A11L.UAS.86 - A44 Mitigating GPS and ADS-B Risks for UAS

Task 5: Final Report

July 27, 2023

NOTICE

This document is disseminated under the sponsorship of the U.S. Department of Transportation in the interest of information exchange. The U.S. Government assumes no liability for the contents or use thereof. The U.S. Government does not endorse products or manufacturers. Trade or manufacturers' names appear herein solely because they are considered essential to the objective of this report. The findings and conclusions in this report are those of the author(s) and do not necessarily represent the views of the funding agency. This document does not constitute FAA policy. Consult the FAA sponsoring organization listed on the Technical Documentation page as to its use.

LEGAL DISCLAIMER

The information provided herein may include content supplied by third parties. Although the data and information contained herein has been produced or processed from sources believed to be reliable, the Federal Aviation Administration makes no warranty, expressed or implied, regarding the accuracy, adequacy, completeness, legality, reliability or usefulness of any information, conclusions or recommendations provided herein. Distribution of the information contained herein does not constitute an endorsement or warranty of the data or information provided herein by the Federal Aviation Administration or the U.S. Department of Transportation. Neither the Federal Aviation Administration nor the U.S. Department of Transportation shall be held liable for any improper or incorrect use of the information contained herein and assumes no responsibility for anyone's use of the information. The Federal Aviation Administration and U.S. Department of Transportation shall not be liable for any claim for any loss, harm, or other damages arising from access to or use of data or information, including without limitation any direct, indirect, incidental, exemplary, special or consequential damages, even if advised of the possibility of such damages. The Federal Aviation Administration shall not be liable to anyone for any decision made or action taken, or not taken, in reliance on the information contained herein.

TECHNICAL REPORT DOCUMENTATION PAGE

1. Report No. A11L.UAS.86	**2. Government Accession No.**	**3. Recipient's Catalog No.**
4. Title and Subtitle A11L.UAS.86 - A44 Mitigating GPS and ADS-B Risks for UAS Task 5: Final Report		**5. Report Date** July 27, 2023 **6. Performing Organization Code**
7. Author(s) University of North Dakota William Semke, william.semke@und.edu Prakash Ranganathan, prakash.ranganathan@und.edu Kansas State University Randall Nichols, profrknichols@ksu.edu Embry-Riddle Aeronautical University Hever Moncayo, moncayoh@erau.edu Oregon State University Jihye Park, jihye.park@oregonstate.edu		**8. Performing Organization Report No.**
9. Performing Organization Name and Address University of North Dakota 243 Centennial Dr. Grand Forks, ND 58202		**10. Work Unit No.** **11. Contract or Grant No.**
12. Sponsoring Agency Name and Address FAA		**13. Type of Report and Period Covered** **14. Sponsoring Agency Code** 5401

15. Supplementary Notes

The A44 team has completed the testing, analysis, and demonstration of mitigations report and has made final recommendations which fulfills Task 5 for the A44 ASSURE project. Select mitigation strategies and test plans were chosen from previous reports. This report prioritizes the mitigations identified in Task 2 for further analysis based on those that show the most promise for reducing risks while remaining cost effective and implementable. These test plans were developed in the Task 3 report. The Task 4 report placed particular emphasis on testing mitigations that support sUAS operations. The use of simulated flight data is a significant source of the test data used for evaluation.

17. Key Words GPS, ADS-B, signal dropouts, erroneous data, jamming, spoofing	**18. Distribution Statement** No restrictions. This document is available through the National Technical Information Service, Springfield, VA 22161.

19. Security Classification (of this report) Unclassified	**20. Security Classification (of this page)** Unclassified	**21. No. of Pages** 153	**22. Price**

Form DOT F 1700.7 (8-72) Reproduction of completed page authorized

TABLE OF CONTENTS

TABLE OF FIGURES

TABLE OF TABLES

TABLE OF ACRONYMS

1090ES	1090 Extended Squitter Data Link
A/C	Aircraft
ABR	AdaBoost Regressor
ACAS	Airborne Collision Avoidance System
ADS-B	Automatic Dependent Surveillance-Broadcast
AGL	Above Ground Level
A-GPS	Assisted GPS
ASTERIX	All-purpose Structured EUROCONTROL Surveillance Information eXchange
ATC	Air Traffic Control
ATO	Air Traffic Organization
ATS	Air Traffic Services
BPSK	Binary Phase Shift Key
BRR	Bayesian Ridge Regressor
BVLOS	Beyond Visual Line Of Sight
C/A	Coarse Acquisition
C2	Command and Control
CD	Collective Detection
CIA	Confidentiality, Integrity, and Availability
COTS	Commercial Off The Shelf
CRC	Cyclic Redundancy checks
CTN	Coarse -Time Navigation
DAA	Detect and Avoid
DoS	Denial Of Service
ECD	Eichelberger's Collective Detection
EKF	Extended Kalman Filter
ERAU	Embry Riddle Aeronautical University
ETR	Extremely Randomized Trees or Extra-Trees Regressor
FAA	Federal Aviation Administration
FMS	Flight Management System
ft	Feet
GAN	Geomagnetic Aided Navigation
GN&C	Guidance, Navigation, and Control
GNAV	Geomagnetic based Navigation
GNSS	Global Navigation Satellite System
GPS	Global Positioning System
GSFD	Ground Station Flood Denial
Hz	Hertz
ICCP	Iterative Closest Contour Point

IGRF	International Geomagnetic Reference Field
IMU	Inertial Measurement Unit
INS	Inertial Navigation System
km	Kilometer
kNN	k-Nearest Neighbor
KSU	Kansas State University
LNAV	Legacy Navigation
LTE	Long-Term Evolution
MAD	Mean Absolute Deviation
MAE	Mean Absolute Error
M-code	military code
MIMO	multi-input multi-output
NAC	Navigation Accuracy Category
NAS	National Airspace System
NDM	Navigation Data Modification
NEDP	Nearest Euclidean Distance Point
NIC	Navigation Integrity Criteria
NIST	National Institute of Standards and Technology
NM	Nautical Miles
NPROD	Normalized Product Correlation
NTP	Network Time Protocol
OrSU	Oregon State University
PDOP	position dilution of precision
PID	Proportional Integral Derivative
PRN	Pseudo-Random Noise
PROD	Product Correlation
RF	Radio Frequency
RFR	Random Forest Regressor
RINEX	Receiver Independent Exchange
RMSE	Root Mean Squared Error
RN	Relative Navigation
SDR	Software Defined Radio
SIC	Successive Interference Cancellation
SIL	Surveillance Integrity Level
SMS	Safety Management System
SNR	signal-to-noise ratio
SoOPs	Signals of Opportunity
SSLT	Seamless Satellite-Lock Takeover
sUAS	Small UAS
SV	Space Vehicle

SWaP	Size, Weight, and Power
ToF	Time of Flight
UAF	University of Alaska Fairbanks
UAS	Uncrewed Aircraft Systems
UAVs	unmanned aerial vehicles
UTC	Coordinated Universal Time

EXECUTIVE SUMMARY

Unvalidated or unavailable Automatic Dependent Surveillance-Broadcast (ADS-B) and Global Position Systems (GPS) data poses security and safety risks to automated Uncrewed Aircraft Systems (UAS) navigation and to Detect and Avoid (DAA) operations. Erroneous, spoofed, jammed, or drop outs of GPS data may result in uncrewed aircraft position and navigation being incorrect. This may result in a fly away beyond radio control, flight into infrastructure, or flight into controlled airspace. Erroneous, spoofed, jammed, or drop outs of "ADSB-In" data may result in automated uncrewed aircraft being unable to detect and avoid other aircraft or result in detecting and avoiding illusionary aircraft. For automated DAA, a false ADS-B track can potentially be used to corral the uncrewed aircraft to fly towards controlled airspace, structures, terrain, and so on. This research is necessary to enable safe and secure automated small UAS (sUAS) navigation and DAA operations. Goals for the project include reports and recommendations useful for Federal Aviation Administration (FAA) policy development and UAS standards development. It is expected that this information will be used to better understand the risks and potential mitigations, and to help the FAA to reassess and refine FAA policy with respect to validation of ADS-B data.

The A44 team has completed the testing, analysis, and demonstration of mitigations reports and has made final recommendations which fulfills Task 5 for the A44 ASSURE project. Select mitigation strategies and test plans were chosen from previous reports. This report prioritizes the mitigations in Task 2 for further analysis based on those that show the most promise for reducing risks while remaining cost effective and implementable. These test plans were developed in the Task 3 report. The Task 4 report placed particular emphasis on testing mitigations that support sUAS operations. The use of simulated flight data is a significant source of the test data used for evaluation. Full reports can be found in the appendices of this document.

The integrity of ADS-B and GPS navigation systems were tested to detect threats to the integrity and/or reliability of the data. These risks include dropped, erroneous, spoofed, and jammed data from GPS and/or ADS-B systems. Several mitigation schemes were flight and simulation tested based on their potential effectiveness in jamming and spoofing conditions. The mitigation schemes tested are cellular signal navigation, the Eichelberger's Collective Detection (ECD) method, optical flow, and geomagnetic navigation. Previous results indicate that these have an overall high effectiveness rating, while having varying effectiveness in the individual factors scored.

The UAS anomalies section focused on using ADS-B data sets to identify ADS-B anomalies that would result in ceasing operations and identify the scenarios that are most common. The data analyzed was collected by using flight test operations at University of Alaska Fairbanks (UAF) as well as from a unique case study of public use ADS-B data from the Dallas Fort Worth airport. Additional metrics are recommended for ADS-B reception quality and the distance and altitudes of the ADS-B receiver and transmitting aircraft. The DFW case clearly illustrated the possibility of extended loss of ADS-B signals and the subsequent need for mitigation strategies. Flight tests were developed to record and utilize nearby Long Term Evolution (LTE)/4G cellular signals to inform a Global Navigation Satellite System (GNSS)-independent positioning solution from a UAS-based receiver. The findings show precise cellular signal positioning approaches have strong potential for mitigating risk in UAS operations and should be considered a supporting navigation

aide. For the spoofing chapter, the ECD method was studied in a simulation environment to produce preliminary data to assess its effectiveness. The research efforts have shown the viability and unique capabilities of ECD to detect spoofed signals, mitigate the false and true signals, and recover the true signals. A functional GPS simulation model has been created as an initial step in establishing ECD validity. The evaluation of the capabilities, advantages, and limitations of optical flow and geomagnetic navigation techniques were tested using both flight and simulated data. These algorithms have demonstrated significant potential in improving the accuracy and robustness of navigation systems.

1. INTRODUCTION AND BACKGROUND

The FAA position communicated to Radio Technical Commission for Aeronautics Special Committee 228 is that UAS DAA systems should validate "ADS-B In" data before it is used to conduct DAA. A risk assessment and exploration of potential solutions is needed to inform potential policy updates for different types of UAS and operations for both GPS validation and ADS-B In validation. Potential risks and/or mitigations examples considered at the onset of the project are as follows:

- Potential Risk: If GPS data drops out or is jammed, the UAS may not know exactly where it is located and may fly away without anyone's knowledge of where it is. Note that sUAS are not tracked by Air Traffic Control (ATC) radar. Potential mitigations include means to detect broad area GPS jamming or GPS dropouts. Examples: monitor the known GPS position of a fixed GPS receiver on a cell phone, ground control station, tower, and other UAS that is on the ground. Alternatively, have an independent means of temporary navigation and UAS tracking sufficient to cease operations safely. Examples: Inertial Measurement Unit (IMU) navigation, UAS beacons (Radio Frequency (RF) or optical), vision-based navigation, rough triangulation, or signal direction finding from the ground using Command and Control (C2) Signal to Noise Ratio (SNR) or time of flight analysis, etc.
- Potential Risk: If GPS signals are spoofed, the UAS may think it is in one location when it is actually at another location. This may result in the UAS crossing airspace boundaries, flying beyond radio control, sudden climbing to avoid terrain referenced onboard digital terrain elevation maps, etc. Potential mitigations could include means to detect broad are GPS spoofing. Examples: monitor the known GPS position of a fixed GPS receiver on a cell phone, ground control station, tower, or other UAS that is on the ground. Alternatively, have an independent means of temporary navigation sufficient to cease operations. Potential examples may include temporary IMU navigation, navigation by C2 signal strength, UAS beacons (RF or optical), vision-based navigation, etc.
- Potential Risk: "ADS-B In" signals drop out or are jammed. This prevents UAS from detecting and avoiding other aircraft that are transmitting "ADS-B Out." Potential mitigations could include a means to detect ADS-B dropouts and jamming to cease UAS operations when jamming is detected. Example: monitor the signal from a fixed "ADS-B Out" source (potentially easy and low cost). Alternatively, potential mitigations could rely upon detecting jamming and a means to safely cease DAA operations.
- Potential Risk: A false "ADS-B In" signal is detected that harasses the UAS. If the UAS is automated to avoid collisions with other aircraft, there is the potential for false signals to harass and corral an automated UAS thereby directing the UAS where a malicious actor desires it to fly (fly into infrastructure, terrain, controlled airspace, etc.). Potential mitigations could include having a means to validate "ADS-B In" tracks or detect false tracks. Example solutions: rough triangulation or signal direction finding from the ground using SNR or time of flight analysis. Have an ability for overriding UAS automated collision avoidance on unvalidated "ADS-B In" tracks. Cease UAS operations when false "ADS-B In" tracks are detected.

Task 4 testing and analysis of this effort placed particular emphasis on prioritizing mitigations that support sUAS operations. The testing completed in Task 4 included the use of simulated flight data as a significant source of test data for evaluation. The full Task 4 report can be found in the appendices.

This Task 5 Final Report contains summaries of testing results and analysis for UAS navigation anomalies including dropouts and erroneous data, GPS and ADS-B signal spoofing, and GPS and ADS-B signal jamming. The UAS anomalies section uses ADS-B data sets to identify ADS-B anomalies that would result in ceasing operations and identifies scenarios that are most common. The cellular navigation section provides the findings and analysis from flight testing that utilized nearby LTE/4G cellular signals to inform a GNSS-independent positioning solution from a UAS-based receiver. The ECD method is used in the section on signal spoofing in a simulation environment to produce data to assess its effectiveness in identifying spoofing as well as its ability to identify the true signal. Both flight and simulation data to evaluate the capabilities, advantages, and limitations of optical flow and Geomagnetic based Navigation (GNAV) techniques is used to evaluate the mitigation strategies of signal jamming.

1.1 Task 1 Report Summary

The A44 ASSURE Task 1 Literature Review Report (Appendix 1) provides a literature review and meta-analysis that identified the potential safety and security risks of relying on GPS and ADS-B data used for UAS operations. It is divided into three areas of investigation: signal dropouts and erroneous data, jamming, and spoofing that may result in safety or security risks to UAS operations that rely on GPS and ADS-B data. Based on the information gathered, a safety and security risk assessment of potential UAS operations that rely on GPS and ADS-B data is presented.

The risk assessments were performed to inform FAA policy decisions and to guide the follow-on tasks. The risk assessments presented were based on the expertise of the research team and the literature review. It is important to note that the likelihood of malicious acts impacting GPS and ADS-B have been increasing over time. This is in part due to the forward advancement of available technology and the decrease in technology cost over time. The risk assessments presented here use projected likelihoods based on current trends and the subject matter expertise of the research team for the 2025 to 2030 timeframe.

The FAA regulates drone operations to represent and protect the interests of third parties that might otherwise be negatively impacted by drone operations. Most drone rules and regulations are built around operators complying with the regulations during operations. Therefore, these drone risk assessments are intended to inform operational approvals and changes to the National Airspace System (NAS) that would be applied to law abiding drone operators. Another primary purpose of the drone risk assessments is to represent third parties that may be adversely harmed by drone operations. This counter balances the drone industry's self-interests that may at times neglect the safety interests of third parties.

A summary of the risk assessments is provided based on the literature review and subject matter expert discussions. The risk assessments were informed by Order 8040.6, which provides additional

information to what is listed in Order 8040.4. The risk assessments were also informed by the Safety Management System (SMS) Air Traffic Organization (ATO) SMS Manual, and Safety Risk Management Guidance for System Acquisitions along with internal risk assessment measures. Order 8040.6 states that for operations above 400' Above Ground Level (AGL) in Class G airspace, the FAA follows the UAS Safety Risk Management policy. Order 8040.6 provides the following tables and risk matrices to be used for drone operations in Class G airspace below 400' AGL and for operations below the ATO Facility Map Altitudes.

Minimal 5	Minor 4	Major 3	Hazardous 2	Catastrophic 1
Negligible safety effect	– Physical discomfort to persons – Slight damage to aircraft/vehicle	– Physical distress or injuries to persons – Substantial damage to aircraft/vehicle	Multiple serious injuries; fatal injury to a relatively small number of persons (one or two); or a hull loss without fatalities	Multiple fatalities (or fatality to all on board) usually with the loss of aircraft/ vehicle

* Excludes vehicles, crew, and participants of commercial space flight.

Figure 1. FAA Order 8040.6 Severity Definitions.

For Figure1, Order 8040.6 Severity Definitions, it is often interpreted that the severity that is of most interest is the severity experienced by people and systems external to the drone and its remote pilot. This includes people on the ground, people in other aircraft, damage to other aircraft, and so forth.

	Qualitative	Quantitative – Time/Calendar-based Occurrences Domain-wide/System-wide
Frequent A	Expected to occur routinely	Expected to occur more than 100 times per year (or more than approximately 10 times a month)
Probable B	Expected to occur often	Expected to occur between 10 and 100 times per year (or approximately 1-10 times a month)
Remote C	Expected to occur infrequently	Expected to occur one time every 1 month to 1 year
Extremely Remote D	Expected to occur rarely	Expected to occur one time every 1 to 10 years
Extremely Improbable E	Unlikely to occur, but not impossible	Expected to occur less than one time every 10 years

Figure 2. FAA Order 8040.6 Likelihood definitions for general aviation operations for small aircraft and rotorcraft.

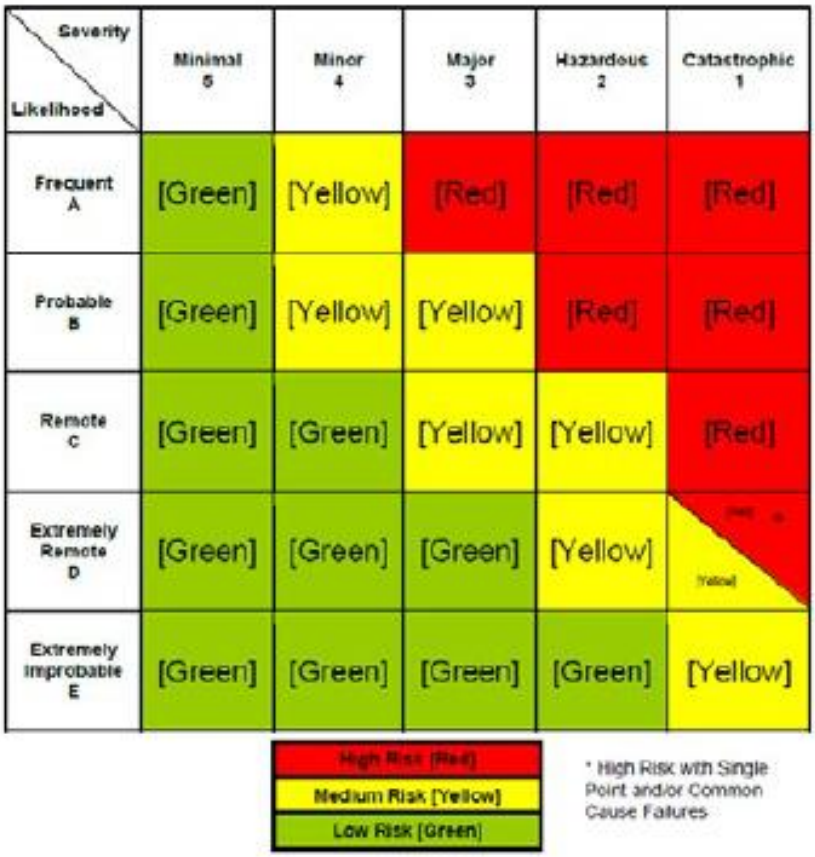

Figure 3. Order 8040.6 risk matrix for general aviation operations for small aircraft and rotorcraft.

The FAA ATO SMS manual provides guidelines to assess the severity and likelihood of identified risks under the domain of the FAA ATO. This includes drone operations above 400' AGL in class G airspace, operations above the ATO Facility Map Altitudes, and operations in all other airspace. For flight operations, the research team used the SMS severity classifications for UAS shown in Figure 4. In addition to these severity classifications, additional security classifications for security risks were developed, as shown in Figure 5.

Severity Classifications for Unmanned Aircraft Systems

Effect On	Minimal 5	Minor 4	Major 3	Hazardous 2	Catastrophic 1
▼	Conditions resulting in any one of the following:				
Unmanned Aircraft Systems	Discomfort to those on the ground Loss of separation leading to a Measure of Compliance greater than or equal to 66 percent	Low Risk Analysis Event severity, two or fewer indicators fail Non-serious injury to three or fewer people on the ground	Medium Risk Analysis Event severity, three indicators fail Non-serious injury to more than three people on the ground A reduced ability of the crew to cope with adverse operating conditions to the extent that there would be a significant reduction in safety margins Manned aircraft making an evasive maneuver, but proximity from Unmanned Aircraft remains greater than 500 feet	High Risk Analysis Event severity, four indicators fail Incapacitation to Unmanned Aircraft System crew Proximity of less than 500 feet to a manned aircraft Serious injury to persons other than the Unmanned Aircraft System crew	A collision with a manned aircraft Fatality or fatal injury to persons other than the Unmanned Aircraft System crew

Figure 4. Severity Classifications of flight operations for Unmanned Aircraft Systems from the Safety Management System ATO SMS Manual.

The SMS qualitative likelihood table used for both flight operations and security threats under the domain of the FAA ATO is shown in Figure 4.

Likelihood Table — Qualitative

Note: This table only applies if the proposed NAS change or existing safety issue affects all ATO operations in a particular air traffic domain. Therefore, it cannot be used for site-specific changes or issues.

	Operations: Expected Occurrence Rate (Calendar-based) Qualitative (Domain-wide: NAS-wide, Terminal, or En Route)
A Frequent	Equal to or more than once per week
B Probable	Less than once per week and equal to or more than once per three months
C Remote	Less than once per three months and equal to or more than once per three years
D Extremely Remote	Less than once per three years and equal to or more than once per 30 years
E Extremely Improbable	Less than once per 30 years

Figure 5. Qualitative Likelihood Table for Unmanned Aircraft Systems from the Safety Management System ATO SMS Manual.

As noted in Figure 5, of the ATO SMS Manual and in

Figure 2 of Order 8040.6, the FAA likelihood criteria only applies to proposed NAS wide changes that affect all similar operations in a particular air traffic domain. FAA likelihood tables are intended to assess the safety of wide scale changes and new types of operations applied across the NAS. For

a given severity assignment, the associated likelihood tables refer to all events across all similar drone operations throughout the NAS. The FAA likelihood tables are not for a single drone and its specific operation. For example, there is a large difference between the likelihood of a specific drone and its operation experiencing a certain severity rating every three years and the likelihood of any drone throughout the entire NAS that is operating in a similar manner experiencing the same severity rating every three years. Using these definitions, the risk matrix and associated classifications under the domain of the FAA ATO are shown in Figure 6.

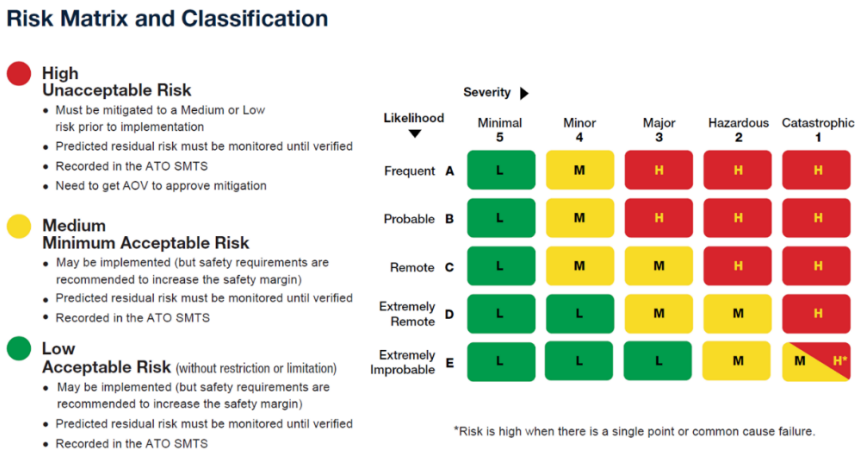

Figure 6. Risk Assessment and Classifications for Unmanned Aircraft Systems from the Safety Management System ATO SMS Manual.

In order to use the likelihood tables, the risk assessment assumes a 2025-2030 timeframe. It assumes that there are many tens of thousands of Beyond Visual Line Of Sight (BVLOS) drone operations throughout the NAS over rural areas, over urban areas, and near airports.

Many drones receive GPS signals for navigation. This risk assessment examined the potential severity and likelihood of outcomes for drone operations where GPS is the sole means of navigating BVLOS. Risk assessments included events traced to GPS dropouts and erroneous GPS signals derived from non-malicious causes. In addition, this risk assessment also examined the risks of cyber-attacks that jam or spoof GPS signals used for drone navigation.

This risk assessment also investigated the potential severity and likelihood of outcomes for drone operations where the drone uses "ADS-B In" as the sole means of detecting other aircraft transmitting "ADS-B Out". This risk assessment assumes that all other aircraft are equipped with "ADS-B Out" and that the drone does not have additional surveillance capabilities to detect approaching aircraft. The purpose of this risk assessment is to focus on potential risks that may occur under these theoretical assumptions and conditions. The risk assessment can then be leveraged when considering future changes to the NAS to enable wider drone operations.

By focusing only on the avoidance of other aircraft equipped with "ADS-B Out," the risk assessment will also inform DAA standards and DAA architectures that intend to operate in the NAS as it exists today. A concern that has been expressed by the small UAS DAA industry is that the cost and complexities of independent validation of ADS-B messages can be high and overly burdensome. By

focusing the risk assessment only on interactions between the drone and ADS-B equipped aircraft, this risk assessment also informs those discussions.

The six major categories of ADS-B and GPS data safety and security risks are ADS-B Dropouts and Erroneous Data, GPS Dropouts and Erroneous Data, ADS-B Jamming, GPS Jamming, ADS-B Spoofing, and GPS Spoofing which are broken into smaller operation types. Further definition of the Risk Assessment is required to provide a clear and informative overview, the mission operation types are broken into four classifications: Part 107 Operations, BVLOS over rural areas, BVLOS Operations over Urban Areas, and BVLOS operations Near Airports in Class B, Class C, or Class D airspace or airports which have Facility Map Altitude limitations. For BVLOS operations near airports, the drone operation under evaluation is intended to remain under the facility map altitudes and the risk assessment will also consider events that may result in the drone crossing facility map altitudes in addition to other risks. For each category, the severity and likelihood probability and associated references were presented.

Part 107 Operations will serve as the base reference. BVLOS operations over rural areas is the next category as it is crucial for many UAS operations and is of great importance to the UAS community. BVLOS operations over urban areas represent a unique case due to signal interruptions and other artifacts along with the density of humans and infrastructure. BVLOS operations near airports operations represent another unique situation due to the air traffic density and potential impacts to commercial airline traffic.

The team used a qualitative approach to risk assessment as there is a void in literature in regard to an appropriate quantitative scale. The risk levels are chosen by the ASSURE subject matter experts involved in this project in all the categories reviewed. They are based on an extensive literature review of the topics and use the most up-to-date and comprehensive studies that are available.

Table 1 is a summary of the risk levels for the six classes and four classifications of operations in a table format to illustrate continuum of risk levels in the various combinations as assessed by the subject matter experts.

Table 1. Summary of the risk levels for the 6 classes and 4 classifications of operations.

Risk	**Part 107**	**Rural BVLOS**	**Urban BVLOS**	**Near Airport BVLOS**
ADS-B Dropout	LOW	MEDIUM	MEDIUM	HIGH
GPS Dropout	LOW	MEDIUM	HIGH	HIGH
ADS-B Signal Jamming	LOW	LOW	MEDIUM	HIGH
GPS Signal Jamming	LOW	LOW	MED/HIGH	HIGH
ADS-B Signal Spoofing	LOW	MEDIUM	MED/HIGH	HIGH
GPS Signal Spoofing	LOW	MED/HIGH	MED/HIGH	HIGH

From this analysis it is evident that the only low risk situations occur with operations in the Part 107 conditions. This was expected due to the nature of Part 107 and the current operability allowed by the FAA. In the medium risk category, most of the conditions are either in the BVLOS or urban area conditions. This is also expected since in both cases the FAA has demonstrated the authority to deviate from certain regulations in the form of a waiver if included in the effective rule, "authorizing" operations or exemptions to certain regulations per 14 CFR Part 11 to allow operations in these areas. The waiver and potentially other situations may be mitigated using additional processes, procedures, and technology to reduce the risk to a lower acceptable level. The high-risk category contains only urban and near airport operations. These areas result in high-risk operations and significant mitigation schemes are needed to reduce the risk to an acceptable level.

1.2 Task 2 Report Summary

In the ASSURE A44 Task 2 Report (Appendix 2), the Risk Management of Mitigation Schemes were addressed. The mitigation strategies identified were evaluated using an assessment tool to provide a metric to the overall effectiveness. The assessment metrics used assessed the overall effectiveness of mitigation schemes. Five things were evaluated to quantify the overall score to rank the proposed methods. These factors are:

1.) Cost

2.) Technical Readiness

3.) Ease of Implementation/Use

4.) Size, Weight, and Power (SWaP)

5.) Impact

Each factor was ranked with a numerical score from 1 to 5, with 1 being the "worst" and 5 being the "best" in each category. A detailed guide for each ranked factor is provided based on the effectiveness of the implementation of the mitigation scheme on a small UAS. Therefore, the factors are the added impact on the "standard' operating configuration.

Cost Rankings

1- Cost over $1000

2- Cost between $500 to $1000

3- Cost between $250 to $500

4- Cost between $100 to $250

5- Cost under $100

Technical Readiness

1- Concept phase

2- Initial prototype testing underway

3- Prototype testing completed

4- Experimental version available

5- Commercially available

Ease of Implementation/Use

1- Extensive modifications/training required

2- Major modifications/training required

3- Moderate modifications/training required

4- Minor modifications/training required

5- Minimal modifications/training required

Size, Weight, and Power (SWaP)

1- Weight greater than 1 kg or power greater than 1 kW

2- Weight between 100 g to 1 kg and/or power between 100 W to 1 kW

3- Weight between 10 g to 100 g and/or power between 10 W to 100 W

4- Weight between 1 g to 10 g and/or power between 1 W to 10 W

5- Weight less than 1 g and power less than 1 W

Impact

1- No impact

2- Little impact

3- Moderate impact

4- Major impact

5- Extensive impact

The cumulative score of the ranked factors generates a value that is indicative to the overall effectiveness. Each factor in the total score has an equal weighting and the sum of all ranking produces the overall score. A scoring breakdown is color coded to outstanding, high, medium, or low value to indicate the overall effectiveness as shown in Table 12.

Table 2. Potential mitigation effectiveness scoring system

Score	Effectiveness
5-10	Low
10-15	Medium
15-20	High
20-25	Outstanding

The scoring system provides a numerical score to aid in overall effectiveness, however this score is to be used for a guide to aid in identifying mitigation strategies with high effectiveness in the current state of development. Some mitigation strategies may have great potential but are early in their development. These strategies, while perhaps did not score high at this time, may have the potential to have a great impact with further development.

This Identification of Potential Mitigations report fulfills Task 2 for the A44 ASSURE project. Examination of recorded ABS-B data was conducted to expose potential risks and provide guidance on mitigation schemes. The examination reveals dropouts and anomalies that occur in flight operations. Based on the risk assessments in Task 1, the performer conducted a survey of market solutions to mitigate loss of GPS and loss of ADS-B data as well as a survey of market solutions to mitigate unvalidated GPS and unvalidated ADS-B In data. The market surveys include estimated costs, ease of implementation, and a preliminary assessment of the effectiveness of market solutions to mitigate the various risks identified in Task 1.

The integrity of navigation systems, such as ADS-B and GPS, was analyzed to detect threats. These risks include erroneous, spoofed, jammed, and dropped data from GPS or ADS-B systems. Recorded ABS-B data was examined to expose potential risks and provide guidance on mitigation schemes. It revealed dropouts and anomalies that occur during flight operations. Two primary data set types were used in this study: GPS data from the Dallas Fort Worth Airport and data from the OpenSky Network. The results are informative and provide real-world assessment of GPS and ADS-B navigation data. Thereby providing knowledge of how often and for how long dropouts and other erroneous data are occurring. The type of machine learning algorithms and the associated settings that process the data more efficiently and effectively were studied.

Several mitigation schemes were evaluated for their effectiveness in jamming and spoofing conditions. The mitigation schemes evaluated were optical flow, geomagnetic navigation, cellular signal navigation, WIFI navigation, and ECD method. The findings are summarized in Table 3.

Table 3. Summary of the GPS and ADS-B risk mitigation methods.

Mitigations Scheme	Condition	Assessment Score	Effectiveness

AI Path Prediction	Drop Outs	13	Medium
Optical Flow	Jamming	16	High
Geomagnetic Navigation	Jamming	14	Medium
Cellular Signal Navigation	Jamming	15	High
W-Fi Navigation	Jamming	12	Medium
ECD	Spoofing	16	High

The study of these five systems indicates that most have an overall high effectiveness rating, while having varying effectiveness in each of the five factors scored. It should be noted that additional mitigation strategies were briefly reviewed but were not of sufficient interest by the team to include in the full evaluation.

1.3 Task 3 Report Summary

The ASSURE A44 Task 3 Planning the Testing and Demonstration of Mitigations Report (Appendix 3) prioritizes the mitigations in Task 2 for further analysis based on those with the most promise for reducing risks while remaining cost effective and implementable. It placed particular emphasis on prioritizing mitigations that support sUAS operations that were tested in Task 4. The use of simulated flight data is included as a significant source of test data for evaluation.

The report contained a test plan for UAS navigation anomalies including dropouts and erroneous data, GPS and ADS-B signal jamming, and GPS and ADS-B signal spoofing. The UAS anomalies chapter focused on using ADS-B data sets to identify ADS-B anomalies that would result in ceasing operations and to identify the scenarios that are most common. With this data the use of hybrid machine learning models was explored. For the jamming chapter, the evaluation of the capabilities, advantages, and limitations of OPNAV and GNAV techniques was tested using both flight and simulated data. In addition, a test was developed to record and utilize nearby LTE/4G cellular signals to inform a GNSS-independent positioning solution from a UAS-based receiver. For the spoofing chapter, the ECD method was used in a simulation environment to produce preliminary data to assess its effectiveness in a challenging scenario.

1.4 Task 4 Report Summary

The Task 4 report contained summaries of the testing and demonstration of mitigations of UAS navigation anomalies including dropouts and erroneous data, GPS and ADS-B signal jamming, and GPS and ADS-B signal spoofing. The UAS anomalies section focused on using ADS-B data sets to identify ADS-B anomalies that would result in ceasing operations and identify the scenarios that are most common. The data analyzed was collected by using flight test operations at UAF as well as from a unique case study of public use ADS-B data from the Dallas Fort Worth airport where ADS-B data was unavailable for an extended length of time over a large area. Additional metrics are recommended for ADS-B reception quality and the distance and altitudes of the ADS-B receiver and transmitting aircraft should be tracked. The DFW case illustrated that extended loss of ADS-B signals may occur, and mitigation strategies are critical for aerospace safety. The jamming section

included flight tests that were developed to record and utilize nearby LTE/4G cellular signals to inform a GNSS-independent positioning solution from a UAS-based receiver. Based on the findings from the cellular navigation study, precise cellular signal positioning approaches show strong potential for mitigating risk in UAS operations and should be further considered as a supporting or backup navigation source in the case of GNSS signal dropout or jamming. For the spoofing chapter, the ECD method was studied in a simulation environment to produce preliminary data to assess its effectiveness. The research efforts have shown the viability and power of ECD to do three things that other countermeasure technologies cannot do: detect spoofed signals in four or more false satellite transmitters, mitigate the false and true signals, and recover the true signals. A functional GPS simulation model was created by Embry Riddle Aeronautical University (ERAU) which needs further modification to explicitly prove the ECD validity. The researchers feel they are on the verge of a huge success in terms of ECD as a countermeasure to reduce the potentially high-risk or catastrophic effects of spoofing and pre-jamming of GNSS/GPS/ADS-B navigation signals in air, land, and sea scenarios. Lastly, the evaluation of the capabilities, advantages, and limitations of optical flow and GNAV techniques were tested using both flight and simulated data. These algorithms demonstrated significant potential in improving the accuracy and robustness of navigation systems. Several challenges and limitations persist and serve as a valid rationale for further research in these areas.

The A44 team Task 4 report on the testing and demonstration of mitigations report provided in depth studies of several navigational mitigation techniques and events that help better inform the FAA and standards bodies detailed information to create appropriate regulations and operational guidelines.

2. UAS NAVIGATIONAL ANOMALIES – DROPOUTS AND ERRONEOUS DATA TESTING AND DEMONSTRATION OF MITIGATIONS

Dropouts and erroneous data in GPS and ADS-B data have severe impacts on navigational awareness and detect and avoid operations. A typical ADS-B is designed to broadcast an update once per second. ADS-B Dropout is referred to the discontinuation of an update within one second (Tabassum 2017), (Sahawneh et al. 2015), (Semke et al. 2017), (Tabassum and Semke 2018). A formal definition for dropout of GPS data is not identified in scholarly literature but for the purposes of this analysis, any circumstance that makes it conducive for GPS data to be degraded (poor or intermittent reception) or denied (unavailability of data for definite periods of time) can be classified as a factor contributing to dropped GPS data (Silvagni et al. 2017; Goforth and Lucey 2019). In this section, the various factors that affect the dropout, particularly those related to the environment, system, and cyber-attacks will be investigated.

2.1 ADS-B Dropouts

Authors in (Tabassum 2017) have conducted four experimental studies to investigate the effect of airborne factors on the dropout frequency. These factors include altitude, range, heading and position. In their first study, four different flight levels were chosen; in the first region, the altitude was less than 4000 feet; in the second one, the altitude was between 4000 and 8000 feet; the altitude in region three was ranging between 18000 and 12000 feet; and the last one's altitude was between 12000 and 18000 feet. The reported experiment results showed that the dropout frequency was high in the first,

third, and forth regions while low in the second region; concluding that flying in an altitude of 4000-8000 feet was the optimal altitude in terms for reducing the ADS-B message dropout. This hypothesis has been proved in another study (Ali, Ochieng, and Zainudin 2017) where the authors found a positive correlation between the aircraft flight level and the ADS-B message update rate as this latter increases when the flight level increases. Based on the second and third experiments' findings, the range and aircraft heading do not have a significant impact on the dropout frequency. Conversely, authors (Ali, Ochieng, and Zainudin 2017) have found out that the aircraft range, which represents the distance between the aircraft position and the ADS-B message received station using ellipsoid distance formula, has an influence on the updating rate as it increases when the flight altitude increases. The fourth experiment indicated that some positions may increase the dropout frequency with longer duration, especially in dense traffic areas, such as terminals.

Authors in (Ali, Ochieng, and Zainudin 2017) have conducted an experimental study for analyzing the performance of ADS-B message broadcast rate from aircraft to the ADS-B ground station in London Maneuvering Area. Specifically, a correlation analysis has been conducted to determine the actual effect of flight's phase on the dropout. Based on the reported findings, the ADS-B message updating performance is poor during the cruising phase at higher levels ranging between 30,000 and 40,000 feet, and relatively high performance during the climbing and descent phases. Thus, the phase of flight has an impact on the ADS-B message updating rate, which may be due to the small distance between ADS-B antenna mounting on the aircraft and the ground station location.

There are other potential external factors that impact the ADS-B message updating rate. For instance, interference with radio frequencies or electromagnetic fields can impact the ADS-B message updating rate. In dense traffic areas, aircraft signal interference is likely to cause ADS-B signal loss. Authors in (Arteaga et al. 2018) have found out that signal drop out may also occur during RF line-of-sight terrain obstruction and aircraft maneuvers. Additionally, heavy electronic system and distance measuring equipment located near the ground receiver may create electromagnetic interference (Tabassum 2017) (Ali et al. 2014). Path loss is another phenomenon where the signal power decreases as the distance between the transmitter and receiver increases (Tabassum 2017). The ADS-B signal can also be affected by distance leading to dropout.

In addition to some environmental related causes, such as multipath, interference, and path loss, the Cyclic Redundancy Checks (CRC) is another potential cause that effects the ADS-B message updating rate. CRC is a mechanism used by ADS-B to check the accuracy of the received message and any message with bit error is discarded at reception (Tabassum 2017). Such a mechanism would increase the dropout frequency at the ground receiver level if faulty data has been accidently injected into the message.

In the same study conducted in (Ali, Ochieng, and Zainudin 2017), a correlation has been found between the aircraft model and the ADS-B message updating rate as the reported results indicated that an A319 provides the optimal performance with 87.35% of the message update rate within 2s, followed by an A321 with 82.32%, and a B777-200 with 80.55%, then a B744 with 72.24%. This performance degradation was due to the different avionic use models including GPS, transponder, and Flight Management System (FMS). Another experimental study (Syd Ali et al. 2016) discussed

the potential effect of avionic types (i.e., GPS model) on the ADS-B message updating rate. The GPS latitude and longitude were provided every 4s for The B747-400 Rockwell Collins GLU920 MMR, and 2s for the B767-300 using Honeywell Mercury Card-equipped EGPWC MkV (system causes). Other ADS-B OUT avionic failure mode that could lead to dropout has been listed in (Ali et al. 2014). The GPS receiver malfunctioning would result in the loss of situational awareness of the aircraft. Since this information is not provided to the ADS-B, the data is not transmitted to other aircraft. Altimeter malfunctioning failure could prevent ADS-B emitters from receiving altitude data. Failure of connection between navigation source and transponder may cause loss of ADS-B positional data. Unstable sensitivity of the ground sensor may cause disruption in the ADS-B message update. Failure of ADS-B ground station power supply may cause unexpected loss of ADS-B data. Failure of data links between the ADS-B ground station and controller working position may cause abrupt loss of ADS-B data. In addition, there are several ADS-B IN failure that could cause dropout (Ali et al. 2014). For instance, the ADS-B IN receiving antenna malfunction may cause sudden loss of ADS-B data to ADS-B IN application. Also, the failure of ADS-B IN receiver on the aircraft may result in a sudden loss of ADS-B data affecting ADS-B IN application.

The relevant operating status information shared by aircraft make them potential targets for attackers. Cyberattacks have a significant impact on the ADS-B message updating rate and could lead to message dropouts or even a denial-of-service situation. Jamming is considered one of these main cyberattacks. In a typical jamming attack, the jammer bombards the communication channel with random data to disturb or even prevent other legitimate users from using the available channel. It is considered a potential threat to all wireless communication networks. With ADS-B systems particularly, jamming may be classified into ground station flood denial attacks and aircraft flood denial attacks (Riahi Manesh and Kaabouch 2017). Although both attack types interrupt the surveillance network by disrupting and blocking communication channels, the first is easier to conduct as the jammer can get closer to its target, the ground station, and send a low power jamming signal. On the contrary, the second attack type requires forging a very high-powered jamming signal to reach the targeted aircraft.

2.2 GPS Dropouts

Depending on the environment a UAS is operating in, it can experience missing or low confidence (degraded) GPS data due to enclosed spaces, remote areas with poor signal reception, objects that obstruct received signal path, multi-path reflection, or poor satellite positioning (Figure 7). Some research also suggests that riverine ambiences (water bodies) also affect the quality of the signal received by the UAS (Sobers, Chowdhary, and Johnson 2009).

Navigation may be degraded due to factors such as interference, signal blockage, or poor signal reception. One way to mitigate degraded navigation is through visual odometry. External reference points that serve as markers can also help in localizing the vehicle and to help the UAV to navigate autonomously. For instance, Nahangi et al. (Nahangi et al. 2018) show the feasibility of fiducial markers (also known as visual tags) and a camera system to localize the vehicle to the visual tag's coordinate frame. Once the onboard hardware computes the 3D translational and rotational vectors, the computed locations are compared to hardcoded ground truth locations that are identified by a distinct "indoor positioning system".

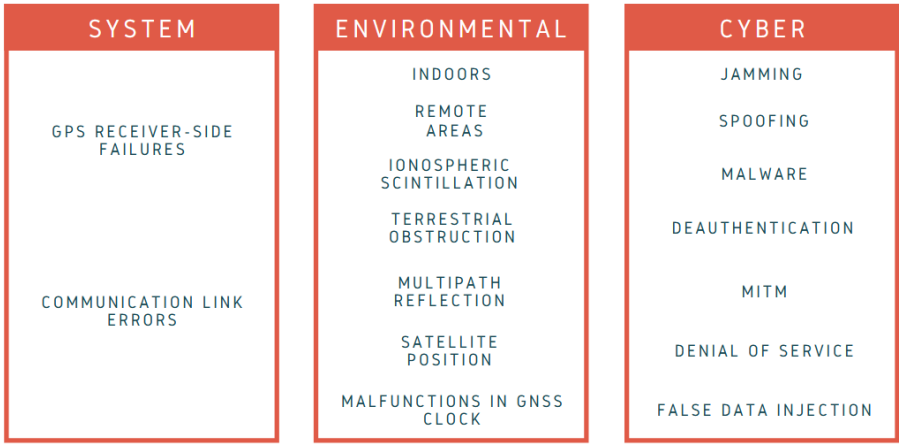

Figure 7. Categorization for causes of dropped and erroneous GPS data.

Ionospheric scintillation is another cause for GPS receivers on UAVs to be unable to lock onto signals provided by the satellite. This is a broadly-defined term for any disturbances experienced by the electromagnetic waves propagating from the satellite at the ionosphere (Kintner, Ledvina, and De Paula 2007). This effect is observed particularly when the ionosphere (which starts at about 46 miles above sea level and is part of the thermosphere) experiences non-uniformity due to magnetic disturbances such as those caused by solar winds. This leads to a situation known as "loss of lock" where GPS receivers are unable to lock onto a satellite signal.

Obstructions from buildings, trees, vehicles, and other infrastructure (particularly in urban areas) lead to degraded or unavailability of GPS data though its effect might be temporary. This might be less of an issue for sUAS operations that are above 400 ft. (which is higher than most structures) but for requirements under this threshold, there might be a temporary drop in GPS data (Gebre-Egziabher and Taylor 2012). A related but distinct consequence of obstructions is multipath reflections which lead to multiple wave fronts received by the GPS receiver. If the multipath reflections are too dense, the GPS receiver will be unable to detect the transmitted data and this can cause periods of intermittent data reception (Isaacs et al. 2014).

According to (GPS.GOV 2021), the position of the satellite directly affects the quality of service (QoS) of relayed GPS data to the user segment such as sUAS. This is because a minimum of three satellites are required to determine the position of a user, but four satellites are ideal to have a precise determination for the GPS receiver. Though the deployed GPS satellites orbit the earth twice a day (two 12-hour periods), not all locations have sufficient accuracy to effectively operate UAS.

For all these causes, it's important to identify mitigation solutions that can address the need based on the factor causing the dropout. For instance, receiver-side clock correction can be used to increase the accuracy of the data provided by GPS satellites which are subject to clock errors. Figure 8 categorizes the most common elements in a localization solution based on hardware and software.

Figure 8. Mitigation solutions for GPS denied environments (Ling 2020).

In order to reconstruct the GPS data payload in such situations where there is a loss of lock, an integrated Inertial Navigation System (INS)/GPS solution with a correction mechanism such as the Kalman Filter (Kissai and Smith 2019) can help in localizing the sUAS. In onboard systems that lack such a correction mechanism, dead reckoning (which is the use of previously calculated position, navigation, and timing data to predict current and future parameters) can be a reasonable option; it must be noted, however, that integration drift in the INS can cause errors in each calculated step to be cumulative and can ultimately produce data that is highly deviant from the ground truth.

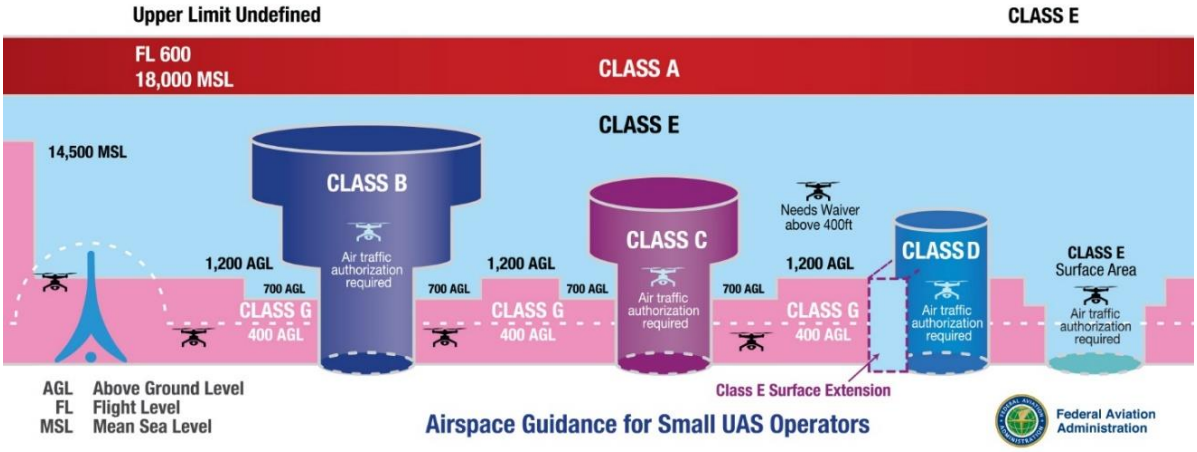

Figure 9. FAA specified operating altitudes for UAVs based on classes (Federal Aviation Administration 2018).

Table 4 shows a comparison of the mitigation tactics and their reliance on GPS data as a secondary system for aided UAV localization. “Application Type” specifies the environment in which the respective mitigation tactic was designed to work in. Outdoor and indoor application types can

potentially work when the UAS experiences GPS dropout due to the factors listed in Figure 9. “GPS Reliance” indicates the degree to which the solution requires current or historical GPS data. “Vehicle Type” lists the rotor specification and the size of the UAV used in terms of altitude, rotor span, and maximum takeoff weight. Micro UAVs have rotor spans under 0.49 ft, altitude under 100 ft Above Ground Level (AGL), and a take-off weight under 0.22 lbs. Miniature UAVs have rotor spans under 2.6 ft, altitude under 500 ft AGL, and a takeoff weight under 6.6 lbs., and the small tactical UAV has a rotor span of 6.2 ft, and a maximum takeoff weight between 22 – 55 lbs.

Table 4. Current mitigation methods based on sUAS vehicle types.

Mitigation Tactic	**Application Type**	**GPS Reliance**	**Vehicle Type***	**Operating Altitude (ft)**	**References**
Laser SLAM, visual odometry, and sensor fusion	Indoor	Medium	Miniature Hexarotor	-	(Bi et al. 2019)
Dual laser scanners, IMU, Robust and Precise Tracking	Indoor	Low	Miniature Quadrotor	-	(F. Wang et al. 2014)
Google Maps, HOG, OP/PF	Outdoor	High	Miniature Quadrotor	< 265	(Shan et al. 2015)
Homography using IMU, monocular camera, compass, EKF	Indoor/Outdoor	Low	Miniature Quadrotor	-	(Zhao et al. 2016)
Robust and Precise Tracking control law for stability, laser odometry, graph SLAM	Outdoor	Low	Miniature Quadrotor	-	(Cui et al. 2016)
GPS/IMU, monocular and stereo cameras	Outdoor	High	Small Tactical Helicopter	-	(Andert et al. 2014)
Relative Navigation (RN)	Indoor/Outdoor	Low	Miniature Hexacopter	-	(Wheeler et al. 2020) (Horri and

frontend and global backend					Palmer 2013)
Radio SLAM using Signals of Opportunity	Outdoor	Low	Miniature Quadrotor	-	(Morales and Kassas 2021)
Relative Visual Localization using IMU and monocular camera	Outdoor	Low	Micro-Miniature Quadrotor	< 500	(Couturier and Akhloufi 2020)

*****Based on the classification criteria by Cai et al. (Cai, Dias, and Seneviratne 2014)

When considering system-related factors that can contribute to GPS dropout data, it is imperative to first discuss the types of wireless technologies used in a UAS. The performance of the GPS can be affected by available wireless communication links within the UAS (onboard sensors/subsystems) and external to the UAS environment (ground station). For example, while the processor inside UAS needs to rely on wireless links for seamless data transport among IMUs and other sensors, there may be advanced scenarios where additional positional information may be required from external UAS environment (ground station) during GPS dropout conditions. In the latter scenario, GPS information needs to be uplinked back to the UAS with updated positional information. According to Lagkas and colleagues (Lagkas et al. 2018), technologies such as Zigbee, WiFi 802.11 a/b/g/n, LoRa, and LTE (4G) can be categorized into wireless personal area network, wireless local area network, low-power wide-area network, and cellular mediums respectively and are the most common technologies used for communication in UAS operations. Before further discussion on the importance of quality of service in UAS communication, it might help to categorize the subsystems of a UAS depending on their primary functions. Similar to a classification framework for motor vehicles and based on a UAV's onboard sensors such as laser, electro-optical, IMU, etc. that gather precise data, stabilized or automated control of the UAV which are forms of UA piloting, and a wireless link between the UAV operator and the UAV that makes piloting possible, it can be said that a UAS operates in the sensing, communication, and control categories respectively and based on a framework used for the automotive industry (El-Rewini et al. 2020), shown in Figure 10. The primary focus will be on the communication layer that handles a full duplex communication, implements technologies mentioned earlier to make wireless communication possible, and inter-UAV communication (in the special case of UAV swarms).

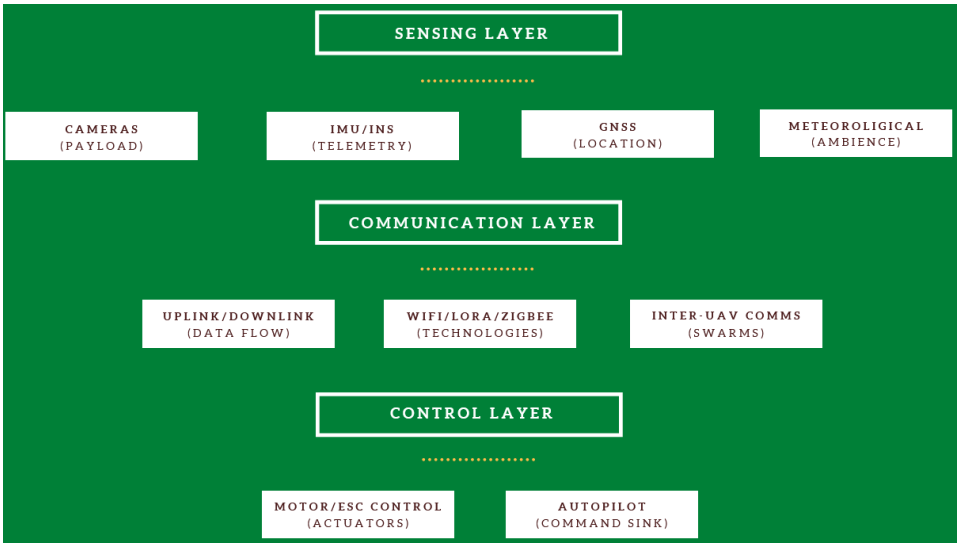

Figure 10. Operating framework for a UAS.

Communication link errors can be controlled if the topology of the UAS network can be identified and implemented before deployment. For instance, it is stated by Gupta and Jain (Gupta, Jain, and Vaszkun 2016) that star networks have higher latency and delays in transmission because the distance between the downlink distances (distance between the node and the GCS) for each UAV in the system is greater than the inter-UAV distance. As the GCS handles all the communication data from each node in the star network, every node in the UAV will not have reliable data if the GCS experiences downtime (Hentati and Fourati 2020). However, both these networks are still susceptible to communication link failures/errors (contributing to dropped GPS data) due to factors such as interference and mobility. One mitigation strategy to regain a functional link is through self-organization of the UAVs in the swarm but there are other considerations that can be investigated.

Considering multi-UAV systems such as those in swarms, much deliberation must go into the application, topology, unit mobility, network configuration, and the dynamicity of the unit's movements. Gupta and Jain (Gupta, Jain, and Vaszkun 2016) state that mesh networks are more reliable and offer better performance in terms of data links as each node is interconnected and has more than one direct link to communicate the data it receives. For Commercial Off The Shelf (COTS) components, design considerations such as the data rate required for the application is a crucial characteristic that needs to be deliberated as it is usually specified by the manufacturer. It is encouraged for UAS to work with a range of data rates depending on channel (transmission medium) conditions. Additionally, parameters that are affected by the channel such as the Multi-Input Multi-Output (MIMO) antennae (Matolak 2015), antenna directivity (power of radio signal in a specified direction), antenna altitude, antenna polarization (matching polarization between the receiving and transmitting antennae promises optimal power transfer), and antenna beamwidth (signal coverage) (H. Wang et al. 2018) will ensure that the inevitable negative effects of environmental factors stated in the previous section can be minimized and while being resource-efficient. More recently, a radio access technique called nonorthogonal multiple access with Successive Interference Cancellation

(SIC) (Yuanwei Liu et al. 2019; Higuchi and Benjebbour 2015) can be considered to mitigate the effects of interference and degraded communication links. However, there are inherent challenges in implementing some of these solutions like MIMO for UAS. For instance, directional mmWave communications utilize MIMO technology but due to the highly dynamic and mobile nature of UAVs, it will be challenging to achieve synchronized transmitter and receiver beam alignment (Zeng, Zhang, and Lim 2016).

The navigation framework on which GPS is based, the GNSS, is susceptible to cyber-attacks that can contribute to GPS data that is dropped or missed (Ly and Ly 2021). Yagdereli and colleagues (Yağdereli, Gemci, and Aktaş 2015) state that it is possible for attackers to "interrupt or corrupt communications between control system components." Mitigation solutions used by the military in such cases include the selective availability anti spoofing module which is a GPS security architecture that provides GPS receivers the ability to encrypt and decrypt received signals (Program and Air Force Program 2012), Military code (M-code) encryption or M-code GPS user equipment, a sensor fusion approach called receiver autonomous integrity monitoring, and GPS receivers that can track multiple state-owned satellite constellations such as GPS, GLONASS, Beidou, or Galileo. GPS receivers in all these cases could be used in ground instruments, weapons systems, or UAVs. Commercial uses, however, require low-cost but efficient solutions to counter cyber threats. Although the GCS and the UAV are vulnerable to attacks such as man-in-the-middle (Ly and Ly 2021), Denial of Service (DoS) (Gudla, Rana, and Sung 2018), keylogging (Hartmann and Steup 2013), spoofing, malware, etc., it has been identified that GPS spoofing followed by GPS jamming are the two most common cyber-attacks identified with lesser research on deauthentication, malware, and keylogging attacks (Leela Krishna and Murphy 2018).

Before listing the attacks that contribute to dropped, degraded, or denied GPS data, it might be helpful to describe which aspect of the Confidentiality, Integrity, and Availability (CIA) triad that the primary concern (dropped GPS data) maps to. According to NIST, availability is "ensuring timely and reliable access to and use of information" and that a "loss of availability is the disruption of access to or use of information or an information system" (National Institute of Standards and Technology (NIST) 2004). By this definition, it can be said that the availability of a system is compromised when it experiences dropped, degraded, or denied GPS data. Keeping this is mind, the two key points of focus when identifying cyber-attacks that cause dropped and/or erroneous GPS data will be to identify cyber threats that primarily compromise the availability (unavailable data when they are required) and integrity (data that are modified/destroyed) respectively though they might also compromise the confidentiality of the data.

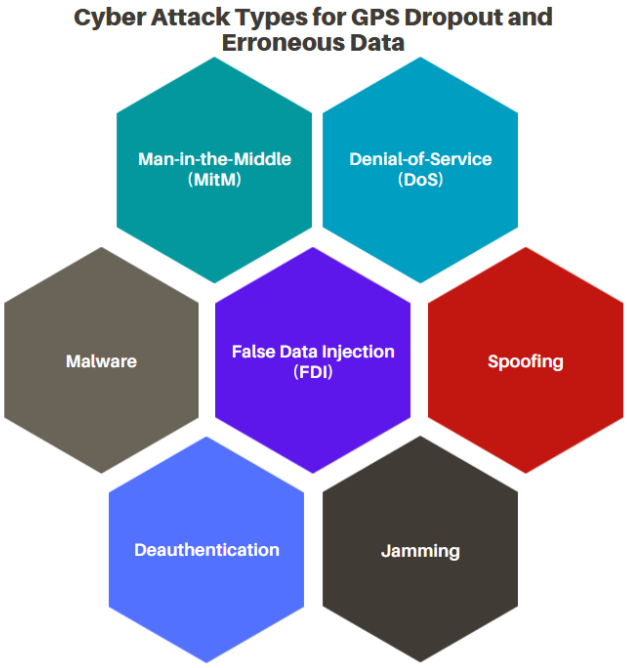

Figure 11. Cyber-attacks that compromise the availability and integrity of UAV GPS data.

As stated by Haque and Chowdhury (Vidal and Choo 2018), one way to classify the attack surfaces is by categorizing attack vectors three distinct groups that can be used to attack the UAV: hardware, wireless, and sensor spoofing.

Though there are variations to jamming attacks, they work on the underlying premise that legitimate GPS signals can be overshadowed by an external malicious agent using hardware that emits a high-power signal that overpowers the legitimate signal. Jamming attacks can pave the way for other attacks such as spoofing so the attacker can trick the UAV into localizing itself with false coordinates (Sedjelmaci, Senouci, and Ansari 2017).

Similarly, a malicious agent can identify a vulnerability in a UAV's communication link to significantly degrade the quality of data sent to the GCS. This is known as a logic-based DoS attack that can be carried out due to software flaws or the lack of proper packet filtering mechanisms (Vasconcelos et al. 2016) and crucial data received by the UAV (such as GPS frames) no longer retains their quality when they are forwarded to the main operator. DoS attacks can also be the ultimate goal before other attacks such as malware-based exploitations are carried out (Garg et al. 2019).

Malware for UAVs can be packaged as exploits that can act as a proxy to listen in on the inter-sensor communication onboard UAVs (GPS, IMU, magnetometer, etc.) based on open ports and forward falsified data or drop traffic altogether when communicating with the GCS (Sung et al. 2020; Shashok 2017). It can also be deployed at the GCS level to modify critical software discreetly and passively record sensitive information or take complete control of the system (Li, Qu, and Lin 2020) and the

possibility of this attack to eventually led to the completely unavailability of the system (DoS) is considered (Garg et al. 2019).

2.3 Alaska Data Analysis

As part of the University of Alaska, Fairbanks contribution to the A44 efforts, a device to record ADSB broadcasts and timestamp them was required. This was accomplished using a Raspberry Pi 3B+, a FlightAware ProStick+ ADSB receiver, a Sparkfun NEO-M9N GPS breakout board, and a custom power and data breakout board. The Raspberry Pi was operated as the primary system controller, with the FlightAware ProStick+ connected via USB, and the GPS module connected via UART.

Dump-1090 was used to run the ProStick+, which outputs the collected information on a variety of Telnet ports. A shell script was used to connect to the telnet ports on the device, which then logged the data to a CSV file. As part of the requirements, the data needed to be timestamped accurately, which was made difficult due to how the raspberry pi handles its time synchronization. The Raspberry Pi has no Real Time Clock module to maintain its internal time during power off, so it assumes that no time has passed between shutdown and startup. Since it gets its time via the Network Time Protocol (NTP), updating the time to the correct time is difficult, so the GPS module was added to map the local time on the raspberry pi to Coordinated Universal Time (UTC).

The GPS module is a breakout board of the uBlox NEO-M9N produced by SparkFun. A time offset was provided by the device. A python script was written to simultaneously collect the local time of the Pi and the UTC time from the GPS at startup.

Figure 12. ADS-B Logger Payload.

The payload was designed to be mounted on the top of one of an Aurelia X6 hexacopter and was powered using the adjustable voltage regulator from the main power bus of the aircraft.

Three flights were conducted across the UAF campus, one at Cornerstone Plaza, one in the Nenana Parking Lot across from the Student Recreation Center, and one in the front Akasofu Parking Lot, as shown in Figure 13.

Figure 13. ADS-B Flight Locations.

The Cornerstone Plaza location was chosen since it was the closest available location to an urban environment. It is the highest density location on campus, with closely spaced buildings and a large amount of foot traffic. It is also located approximately under the approach path for Runway 20 of Fairbanks International Airport. The Nenana lot location was chosen because it is near the foot of a large hill, potentially blocking signals. Finally, the Akasofu location was chosen as it is also near large buildings, as well as powerful RF emitters and has a clear view of the Fairbanks International Airport. During the flights, the drone would ascend to 400 ft, in 100 ft increments, spending 5 minutes at each altitude.

To estimate the aircraft transmission rate from the reception rate an outlier removal methodology was used for estimating the actual ADS-B message transmission rate of a given aircraft for the collected ADS-B. The outlier removal algorithm was used to filter the time interval between consecutive ADS-B messages to estimate the ADS-B message transmission rate of each flight in the data set. Literature reported transmission rates are also provided in Table 5 to serve as an upper limit for reception rate.

Since the recorded flights were for arbitrary aircraft entering the monitored region, it is difficult to establish what the actual time interval between the transmission of consecutive ADS-B messages (i.e., the ideal reception rate in the case of zero lost messages) is for a particular flight as there is no control data set with which to compare. However, as an upper limit for reception rate, Table 5 provides reported ADS-B message transmission rates for different types of messages (“The 1090MHz Riddle” n.d.) and an estimate for the cumulative message frequency (8.1 Hz or 0.123 s/msg) for airborne

aircraft, which was used as a benchmark when comparing the collected data. For example, a reported transmission rate of 8 Hz and an observed reception rate of 4 Hz suggests 50% message loss at the receiver. Transmission rates were used for this benchmarking purpose since, in the ideal case of zero dropouts or lost messages, the transmission and reception rates would be equal. Therefore, the transmission rate provides an upper limit for the reception rate (or lower limit for analyzing time intervals between received messages).

Table 5. Reported transmission Rates of different ADS-B messages. Transmission rate provides an upper limit for reception rate, and transmission time interval provides a lower limit for reception time interval.

	Transmission Rate (Hz)		Time Interval (s)	
Message	Ground	Airborne	Ground	Airborne
Aircraft ID	0.1-0.2	0.2	5-10	5
Surface Position	0.2-2	-	0.5-5	-
Airborne Position	-	2	-	0.5
Airborne Velocity	-	2	-	0.5
Target States & Status	-	0.8	-	1.25
Aircraft Status				
No TCAS RA & Squawk change	0.2	0.2	5	5
Change in TCAS RA or Squawk	1.25	1.25	0.8	0.8
Operational Status				
No NIC/NAC/SIL change	0.2-0.4	0.4	2.5-5	2.5
Change in NIC/NAC/SIL	0.2-1.25	1.25	0.8-5	0.8
Cumulative Estimate		8.1		0.123

Additionally, the time interval between message reception may be influenced by atmospheric interference, physical obstruction, or limitations of receiver capabilities. Therefore, this analysis aims to estimate the mean-time interval between ADS-B message transmission statistically for each flight from the messages received. This estimate is here referred to as the filtered mean-time interval and has an associated upper bound. Time intervals greater than the upper bound are considered outliers and are not included in the calculation for the filtered mean-time interval.

ADS-B messages from a total of 48 aircraft were captured during data collection. Of these flights, some did not contain location data and others did not contain enough messages for reliable statistical analysis. Therefore, analysis was performed only on flights records that contained location data and that had at least 100 messages. These criteria were met by 34 of the 48 total aircraft detected, which are shown in Figure 14. However, some of these aircraft flew multiple trips during the collection

period. To avoid mixing data from grounded and airborne aircraft which have different transmission rates (see Table 5), individual trips were split into separate flight records and only in-flight data was analyzed. After separating the data by individual flights and removing the data corresponding to grounded aircraft, 45 flight records (from 29 aircraft) met the above criteria of 1) containing location data, and 2) having at least 100 messages. Analysis results for these flights are shown in Table 6 where the filtered mean time interval (all outliers removed before averaging) provides an estimate for the transmission rate of the aircraft. For most flights analyzed, the filter mean time interval is within 0.1 s of the estimated transmission rate of 0.123 s/msg, which suggests that outlier filtering may be a valid method for estimating transmission rate from reception rate, however actual transmission rate data for individual aircraft would be needed to verify this. The ability to accurately compute transmission rate from reception rate would enable aircraft (and ground stations) to compute an estimate for the rate of message loss in near real-time.

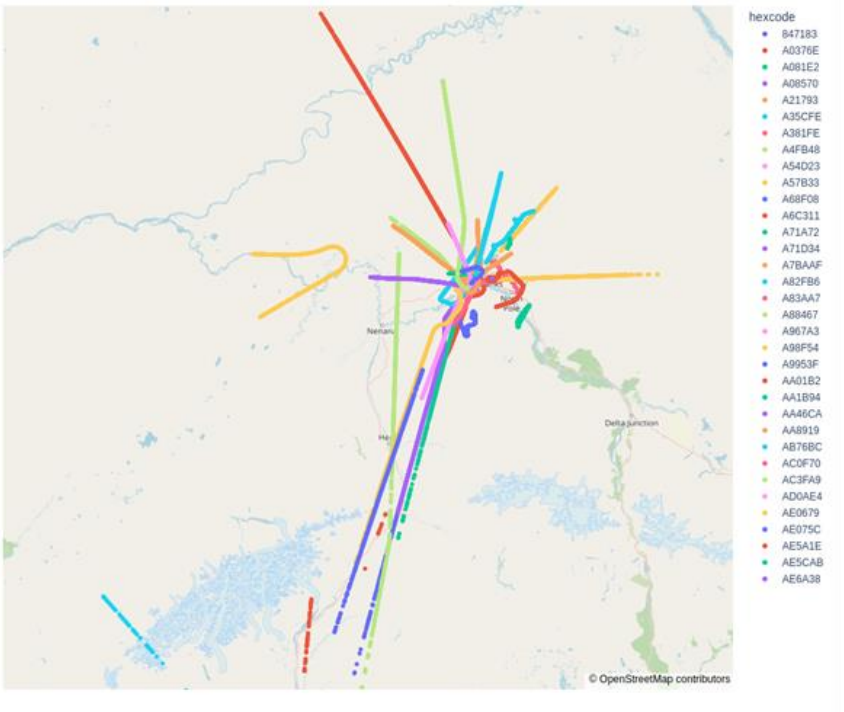

Figure 14. Trajectories for 34 aircraft visualized.

Table 6. Statistical analysis for 45 flights (from 29 aircraft) that contained sufficient data.

Flight Number	Aircraft	Flight Time (H:M:S)	Filtered Mean Time Interval (s)	Upper Bound of RMSE Filter (s)	Max Altitude (Ft)	Type	ICAO-trip#

1	Boeing 747-8KZF	0:14:14	0.447	1.083	33025	large	847183
2	BEECH 1900C	0:36:14	0.193	0.591	21075	large	A0376E
3	Cessna 208B	0:09:41	0.2	0.603	4800	medium	A081E2
4	Cessna 208B C20	0:02:45	0.211	0.636	1900	military	A08570
5	Boeing 737-852 (SF)(W)	0:06:54	0.582	1.325	41000	large	A35CFE
6	Bombardier CL-600-2B16 Challenger 605	0:08:27	0	0.001	1725	large	A381FE-1
7	Bombardier CL-600-2B16 Challenger 605	0:13:08	0	0.001	2525	large	A381FE-2
8	PIPER PA-31-350	0:16:31	0.12	0.275	6800	small	A4FB48-1
9	PIPER PA-31-350	0:00:57	0.161	0.355	800	small	A4FB48-2
10	Cessna 208B	0:11:18	0.195	0.599	7750	medium	A57B33
11	PIPER PA-28-180	0:36:02	0	0.001	4350	small	A68F08-1
12	PIPER PA-28-180	0:02:23	0.18	0.546	1825	small	A68F08-2
13	Boeing 737-890 (W)	0:10:25	0.583	1.296	36700	large	A6C311
14	No data	0:16:28	0.078	0.187	35000	unknown	A71A72
15	Boeing 737-890 (W)	0:19:26	0.137	0.321	25900	large	A71D34
16	PIPER PA-31-350	0:01:54	0.247	0.559	5900	small	A7BAAF-1
17	PIPER PA-31-350	0:11:34	0.16	0.361	5800	small	A7BAAF-2

18	PIPER PA-31-350	0:07:23	0.115	0.272	7600	small	A7BAAF-3
19	Cessna 182R	1:15:12	0	0.001	4900	medium	A82FB6-1
20	Cessna 182R	0:14:14	0.193	0.587	1850	medium	A82FB6-2
21	Cessna T182T	0:11:14	0	0.001	3825	small	A83AA7
22	EMBRAER ERJ-175LR (170-200LR)	0:21:34	0.149	0.344	36000	large	A88467
23	FOKKER F.27MK 500	0:14:52	0.091	0.218	19000	large	A967A3
24	Cessna 208B	0:23:39	0.213	0.624	10750	large	A98F54
25	Pilatus PC-12/47	0:34:04	0.197	0.456	24000	medium	AA01B2
26	Cessna 208B	0:32:55	0.197	0.606	6075	large	AA1B94-1
27	Cessna 208B	0:00:03	0.167	0.582	650	large	AA1B94-2
28	Cessna 208B	0:06:31	0	0.001	6050	large	AA1B94-3
29	Cessna 208B	0:14:21	0.183	0.56	7700	large	AA46CA
30	DOUGLAS DC-6A	0:06:21	0.193	0.606	2500	large	AA8919-1
31	DOUGLAS DC-6A	0:11:10	0	0	3825	large	AA8919-2
32	Cessna 208B	0:16:47	0.21	0.608	8800	large	AB76BC
33	Dehavilland DHC-8-102	0:20:24	0.132	0.312	18800	large	AC3FA9
34	Cessna 208B	0:10:08	0.191	0.588	5125	medium	AD0AE4
35	Boeing C-17A Globemaster III	1:38:08	0.119	0.282	23200	military	AE0679
36	Beech C-12F	0:41:24	0.002	0.004	25025	military	AE075C
37	No data	0:06:28	0.41	0.987	700	unknown	AE5A1E-1
38	No data	0:05:11	0.191	0.454	1550	unknown	AE5A1E-2

39	No data	0:20:55	0.186	0.444	1525	unknown	AE5A1E-3
40	No data	0:03:31	0.098	0.233	750	unknown	AE5A1E-4
41	No data	0:01:08	0.116	0.279	675	unknown	AE5A1E-5
42	No data	0:02:09	0.118	0.281	700	unknown	AE5A1E-6
43	No data	0:01:09	0.177	0.421	675	unknown	AE5A1E-7
44	No data	0:38:12	0.102	0.243	1600	unknown	AE5A1E-8
45	Sikorsky UH-60M Blackhawk	0:31:58	0.243	0.578	3600	military	AE5CAB

Figure 15 shows boxplots for the flight times, filtered mean time intervals, and upper bounds listed, where the mean values are calculated across all 45 flights. Averaging across all flights gives a mean filtered time interval of 0.2 s and an upper bound of 0.4 s (message gaps longer than this are considered outliers and suggest message loss). Given the lack of experimental transmission rate data (per aircraft) which could be used to calibrate the algorithm, the estimate of 0.2 s/msg is surprisingly close to the 0.123 s/msg benchmark calculated from the reported ADS-B message transmission rates. However, as shown in Table 6 and Figure 15, the filtered mean time interval is highly dependent on the aircraft, and it is unknown if this holds true for the true transmission rate.

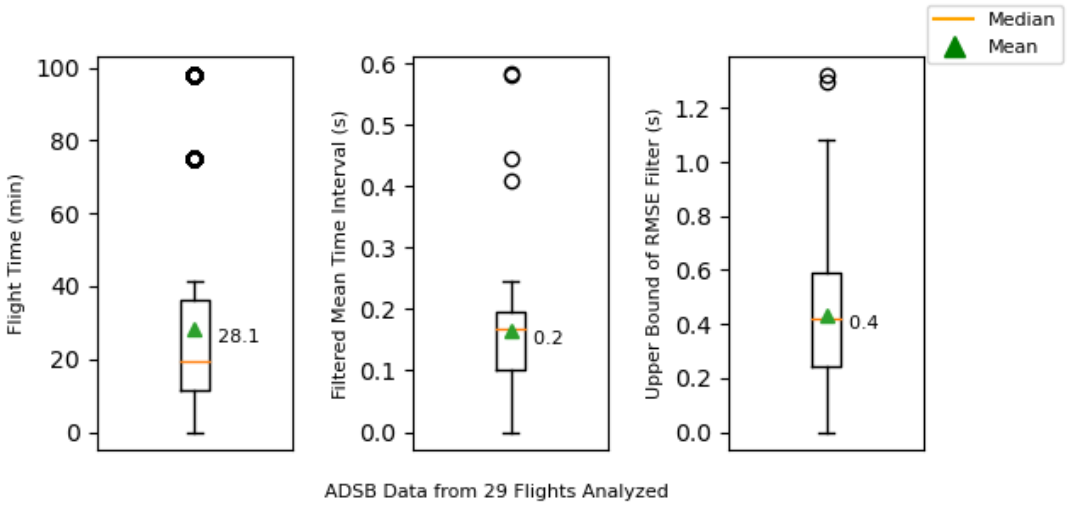

Figure 15. Statistical analysis of flight time filtered mean time interval, and upper bound across all flights.

2.3.1 Effect of Aircraft Altitude on ADS-B Reception Rate

Figure 16 shows boxplots of the time intervals between received messages (unfiltered) binned by maximum flight altitude where the average value across all data points is reported. The range of each bin is 1,000 Ft and is labeled by the maximum value for that bin. For example, the bin labeled 2000 contains data from flights with maximum altitudes > 1,000 Ft and ≤ 2,000 Ft. Note that all grounded data has been removed from the bin with the lowest altitude (> 0 Ft and ≤ 1000 Ft). From the data, reception rate appears to be largely independent of altitude. For most of the altitude bins, the average time interval is near 0.5 s corresponding to a message reception rate of 2 Hz which suggests roughly 75% message loss when compared to the 8.1 Hz transmission rate benchmark.

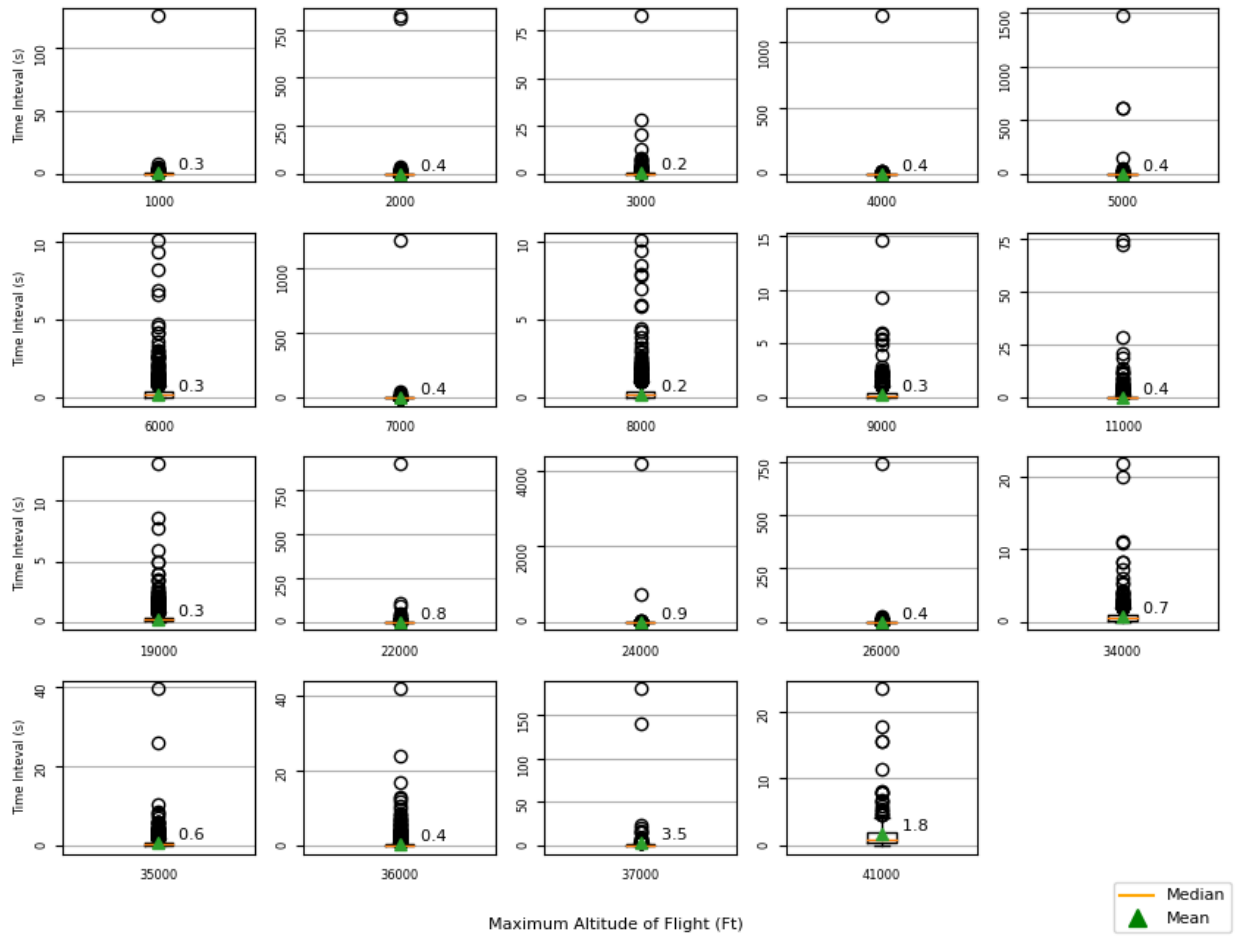

Figure 16. Time intervals binned by maximum flight altitude in 1,000 Ft bins. Bins are labeled by maximum value.

2.3.2 Effect of Aircraft Size on ADS-B Reception Rate

Bins for aircraft size were determined by weight as reported in Table 7. Since some ICAO numbers did not correspond to any aircraft type, an additional "unknown" category was included when analyzing dropout instances and duration by aircraft size. The category "Military" was also binned separately since military aircraft may turn off their ADS-B transceiver.

Table 7. Classification of aircraft by size.

Size Category	Weight
small	< 12.5k lbs
medium	> 12.5k lbs and < 41k lbs
large	> 41k lbs

A dropout was considered any time interval between consecutive ADS-B messages exceeding 10 s. Dropout instances are reported as the average number of dropouts per hour and are shown in Figure 17 for the selected aircraft size categories. This data shows a trend with larger aircraft having more instances of dropout; however, this difference is not statistically significant.

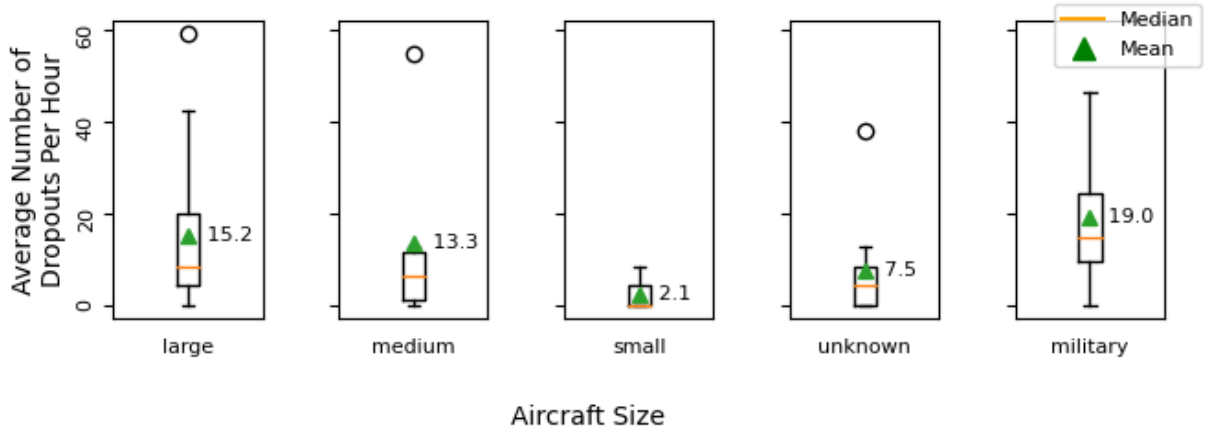

Figure 17. Effect of the aircraft size on the average number of dropouts per hour for 45 flights.

Dropout duration was calculated as the time interval between consecutive messages for each time interval > 10 s. Average dropout duration was calculated over a given flight (ICAO-trip#) and is reported in Figure 18 for the different aircraft size categories. The data displayed in Figure 18 shows that individual dropouts can persist for a long-time interval, with the maximum exceeding 1000 s (15 min) for the "military" category. However, dropout durations are considerably lower for civilian aircraft (all bins other than "military") which is likely due to military planes operating without their ADS-B transceiver turned on. No significant correlation was observed between the average dropout duration of different size categories (large, medium, small).

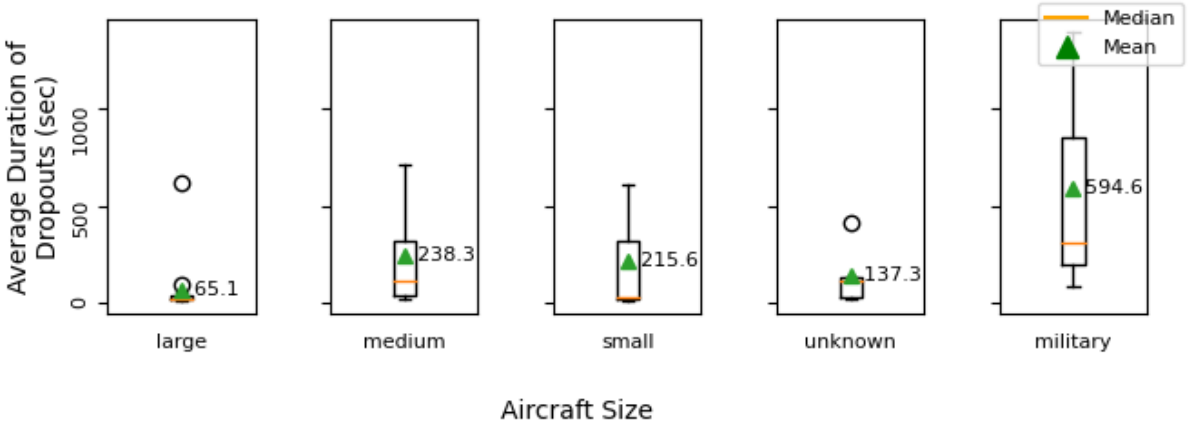

.

Figure 18. Effect of the aircraft size on the average dropout duration.

Mean-time intervals were also analyzed with respect to aircraft sizes. This quantity differs from average dropout duration in that an average of all time intervals is taken for each aircraft size bin,

whereas for dropout duration, only time intervals > 10 s are included in the average. Figure 19 shows the effect of aircraft size on mean time interval, for time intervals between consecutive ADS-B messages of any type (ΔT_msg) and time intervals between consecutive ADS-B location messages (ΔT_loc). No clear trend was observed for the mean-time interval for different aircraft sizes.

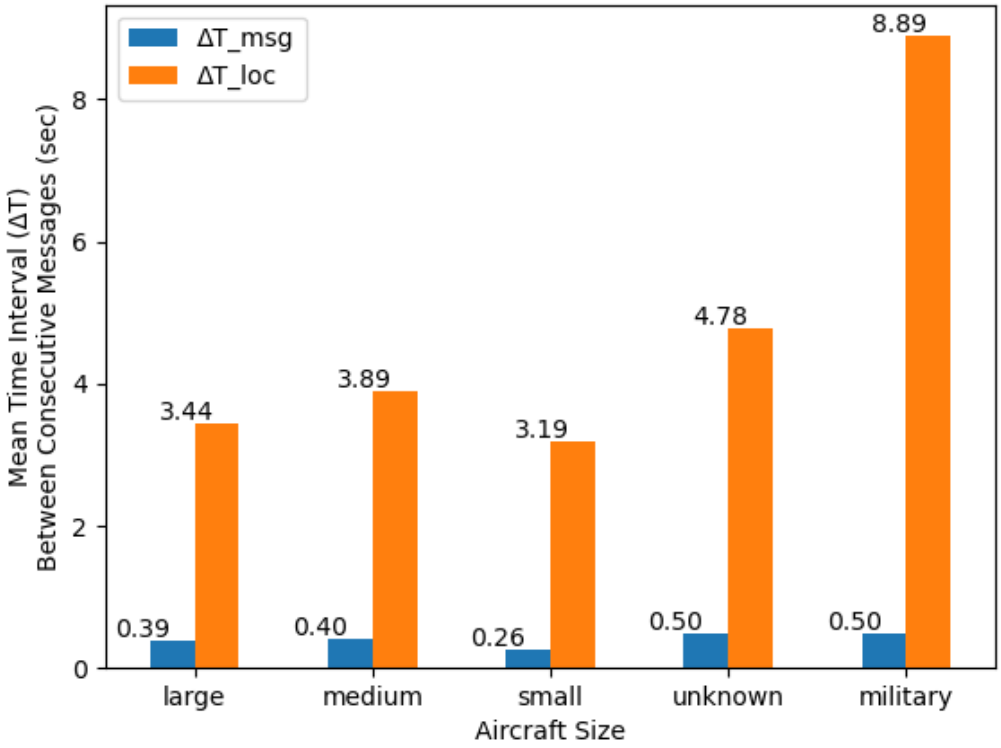

Figure 19. Aircraft size vs Mean time interval between messages.

2.3.3 Effect of Distance from Receiver on ADS-B Reception Rate

The effect of the distance of the aircraft from the UAS-mounted receiver on dropout and mean time interval was also analyzed. Since a time interval is taken between two consecutive ADS-B messages, the distance category was assigned according to the average distance from the receiver for the consecutive messages. Four equally sized distance bins were constructed between the minimum and maximum distances from the receiver in the ADS-B data set. As with the aircraft size analysis (Section 2.3.2), a dropout was considered any time interval between consecutive ADS-B messages exceeding 10 s. Dropout instances are reported as the average number of dropouts per hour and are shown in Figure 20 for each of the distance bins. This data suggests that the aircraft closest to the receiver exhibit the highest frequency of dropouts. Note that this is not due to the large quantity of grounded aircraft at the nearby Fairbanks airport, since all grounded data have been removed.

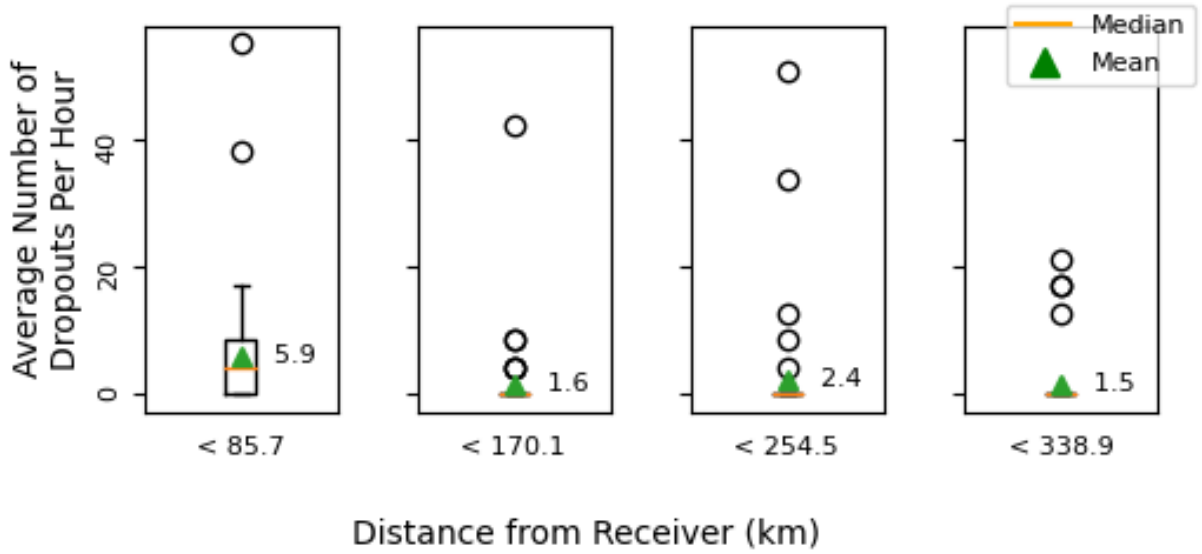

Figure 20. Effect of the distance (km) from the receiver on the average number of dropouts per hour.

As with the aircraft size analysis (Section 2.3.2), dropout duration was calculated as the time interval between consecutive messages for each time interval > 10 s. Average dropout duration was calculated over a given flight (ICAO-trip#) and is reported in Figure 21 for the different distance bins. Surprisingly, dropout duration tends to decrease with increased distance from the receiver, however this may result from the receiver only registering far-away aircraft that have a high-quality transmitter. Note that the longer durations in the shortest distance category (< 85.7 km) are not due to grounded nearby aircraft since all grounded data has been removed.

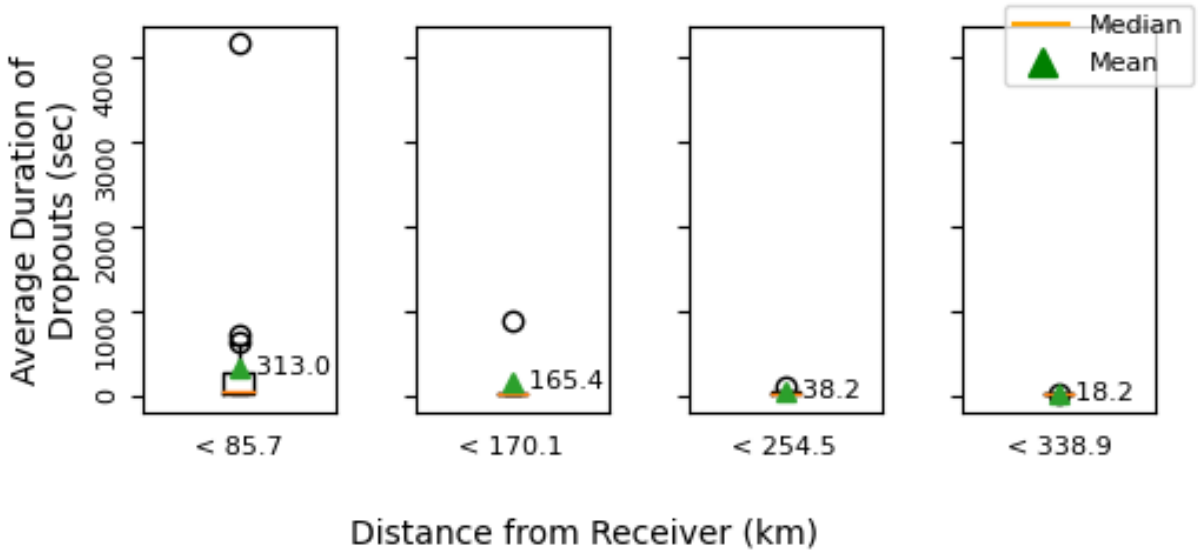

Figure 21. Effect of the distance (km) from receiver on the average dropout duration.

Mean-time intervals were also analyzed relative to distance from the receiver. This quantity differs from average dropout duration in that an average of all time intervals is taken for each distance and aircraft size bin, whereas for dropout duration, only time intervals > 10 s are included in the average. Figure 22 shows the effect of receiver distance on the mean-time interval for time intervals between consecutive ADS-B messages of any type (ΔT_msg) and time intervals between consecutive ADS-B location messages (ΔT_loc). The mean-time interval of both location messages and total messages increases (frequency decreases) with increasing distance from the receiver, suggesting that more messages are lost as the aircraft moves further away. However, this does not result in increased dropout frequency or duration (see Figure 20 and Figure 21) when defining dropout as a > 10 s gap between messages. This suggests that dropout by itself is not a comprehensive metric for evaluating signal quality, and new metrics such as message loss rate may be more descriptive.

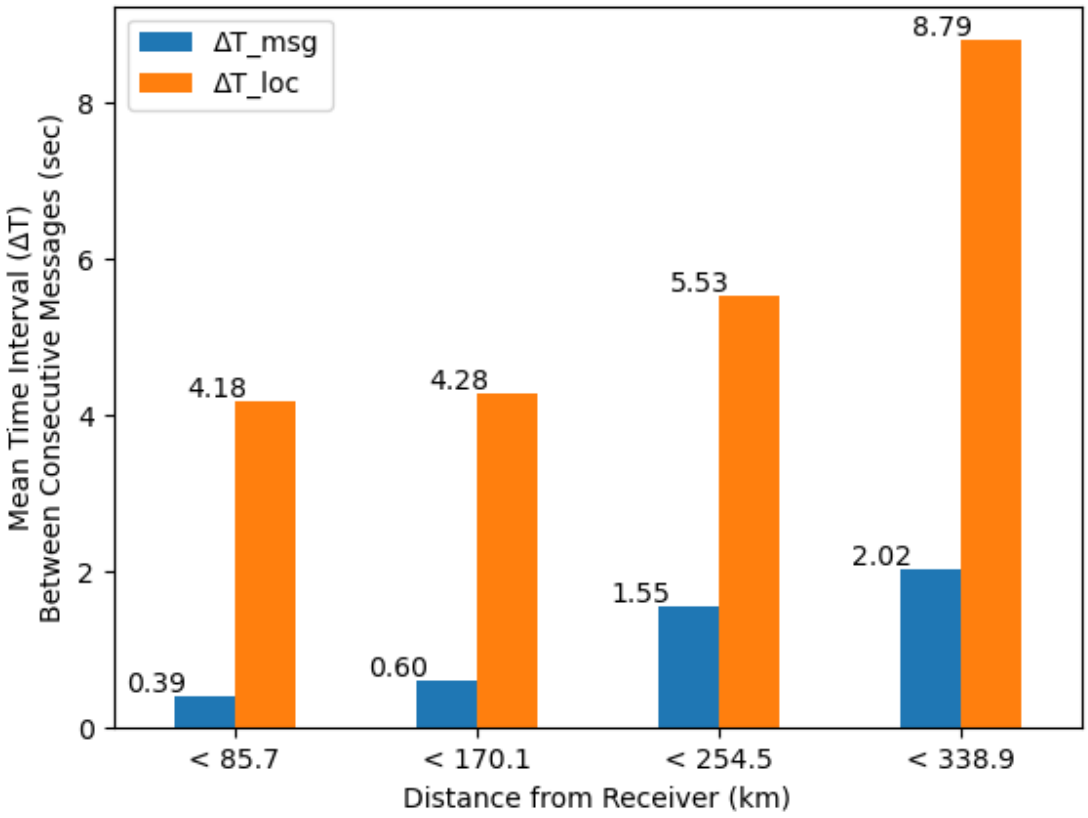

Figure 22. Distance from Receiver vs mean time interval between messages.

2.3.4 Alaska ADS-B Dropout Analysis Conclusions

For airborne aircraft, a cumulative estimate for message transmission rate of 8.1 Hz (0.123 msg/s) (Table 5) was generated by summing the transmission rates of each individual message type (i.e., each row in the airborne transmission rate category of Table 5). This estimate incorporates rates of all message types of airborne aircraft (aircraft ID, airborne position, airborne velocity, target states/status, and aircraft and operational status messages). This cumulative message transmission rate is used as an upper bound for the cumulative reception rate since these rates would be equal in the ideal case of zero lost messages. When comparing the reception data to this ideal total ADS-B message frequency of 8.1 Hz (0.123 msg/s), message loss appears to be a frequent occurrence, given that the filtered mean time interval of 0.2 msg/s (Figure 15) for all flights analyzed is nearly twice that of the estimate for transmission (0.123 msg/s). Also, looking only at dropout frequency and duration (Figure 20 and Figure 21) did not reveal the effect of receiver-transmitter distance on message reception rate (Figure 22). Therefore, metrics other than dropout may be needed to comprehensively characterize ADS-B reception quality, such as an estimated percentage of lost messages in reference to the expected rate of 8.1 Hz. This conclusion is supported by the observation that greater distances between the receiver and transmitting aircraft result in increased mean time intervals but not increased occurrences of dropouts, suggesting that dropout alone may not be an adequate metric.

2.4 DFW Detailed Analysis

The ADS-B is a feature on aircraft that broadcasts its state parameters periodically. Automatic references the fact that transmission happens without the need for operator intervention, and Dependent indicates that the ADS-B depends on other air data systems like altimeters and GNSS like the GPS (Wu, Shang, and Guo 2020; Syd Ali et al. 2016) to obtain the information that it transmits. Surveillance - Broadcast indicates that the state parameters is a broadcast and is available to anyone with receiving equipment. This allows pilots and ATC to have a similar airspace picture and helps improve situational awareness.

The message types and the information transmitted by the ADS-B are outlined in Table 8.

Table 8. Message type and information transmitted by the ADSB.

Message Type	**Information Transmitted**
Identification	Callsign, Wake Vortex Category
Airborne Position	Position, Altitude
Surface Position	Position, speed, and track angle
Airborne Velocity	Vertical rate, GNSS and Baroaltitude difference, Ground Speed, Air Speed
Operational Status	Airborne status message, Surface status message, Capacity class, Operational mode, ADS-B version number, NIC supplement – A, Navigational accuracy category – position, Source integrity level, Horizontal reference direction, SIL supplement

The ADS-B version 2 also broadcasts the following parameters (in the operational status messages) to indicate the accuracy or quality of the transmitted positional information.

1. Navigation Integrity Category (NIC): NIC is an indicator of the accuracy of the transmitted position. The higher the value of NIC, the greater the positional accuracy and vice versa ("The 1090MHz Riddle" n.d.). NIC is transmitted as part of the ADS-B message and has values between 0 and 11. NIC values are related to the containment radius of the aircraft position. For example, a NIC value of 11 has a containment radius of about 7.5 meters, while a NIC of 1 has a radius of 37.04 KM. Further, a NIC value of 0 indicates a complete loss of tracking the containment radius of the aircraft position. Thus, FAA recommends an intermediate agreement of NIC greater than 7 for GPS accuracy tracking. (Garcia n.d.).

2. NIC replaced the Navigational Uncertainty Category parameter in Version 1 of ADS-B.

3. Navigation Accuracy Category (NAC): It is another metric that could be seen as a complementary indicator of NIC and can be used to determine the horizontal and vertical bounds of the position.

4. Surveillance Integrity Level (SIL): Probability estimation of measurements exceeding the containment radius.

In this study of the DFW GPS interference event that occurred in October of 2022 NIC was chosen as a primary parameter to understand patterns that could be typical of such events.

The data set used for analysis is from the OpenSky network ("The OpenSky Network - Free ADS-B and Mode S Data for Research" n.d.). The database was queried in temporally smaller chunks of about four hours to obtain data from 20 00 00 Oct 17th, 2022, to 23 59 59 October 18th, 2022, 40 Nautical Miles (NM) around DFW airport. The dataset contains 5,747,931 data points and about 2,559 unique aircraft.

Figure 23 is a Geo scatter plot showing every data point where the NIC has dropped below 7. The visualization is intended to give a holistic view of the entire dataset.

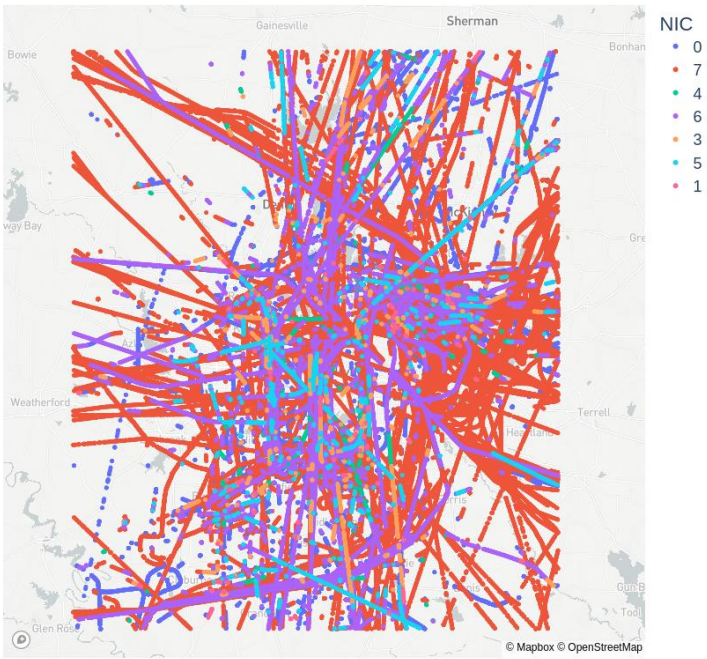

Figure 23. Location of datapoints with NIC less than 7.

2.4.1 DFW Event by Altitude

It is common to find points with low NIC values at lower altitudes. This is because obstructions like trees or high-rise buildings or mountains can obscure a portion of the sky, denying the GPS receiver from being able to view the intended constellation of satellites intended to get a good position fix. However, this is not the case with airborne aircraft. Given their altitude and larger horizon, they would easily get more satellites than what is expected to get a proper position fix. Figure 24 is a violin plot with altitude in the y-axis and NIC values in the X-axis, indicates there are many data points from about 9,000 to 15,000 m altitude whose NIC has dropped to 0.

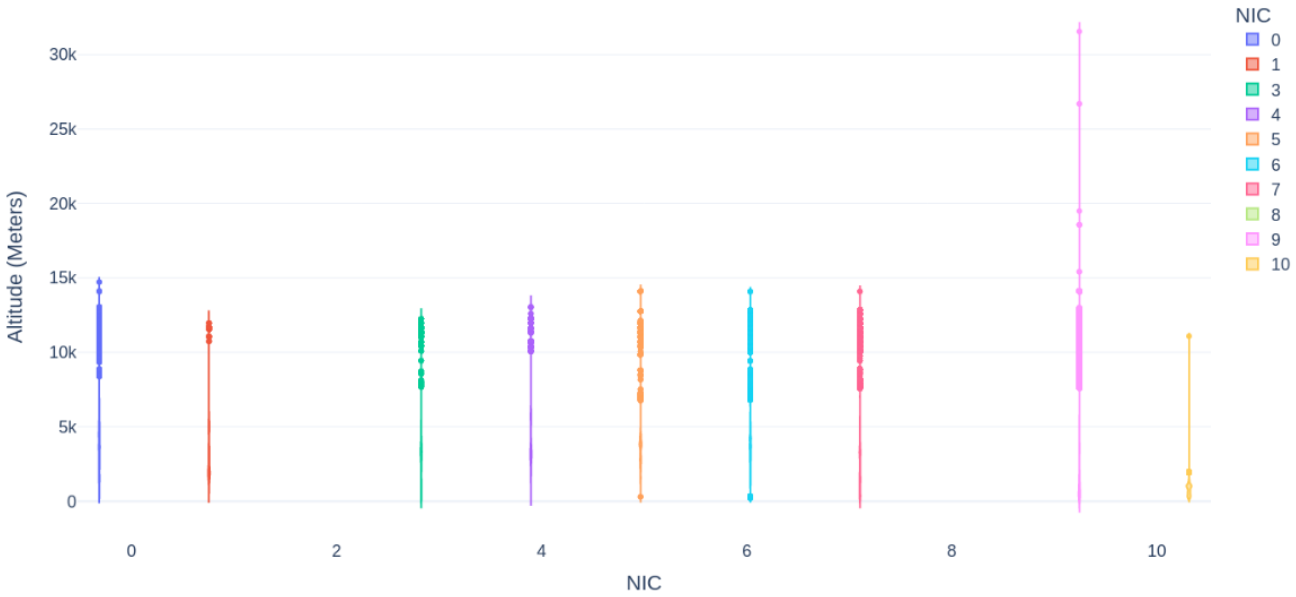

Figure 24. NIC by Altitude.

2.4.2 DFW Event by Change in NIC

The analysis also revealed that when the NIC drops to 0 and recovers, the most typical pattern is a drop from 9 to 0 and a recovery from 0 to 9. This occurs a total of 559 times in the entire dataset. Figure 25 is a bar chart with the count on the y-axis and the change category on the x-axis that visualizes the number of times a given change occurs.

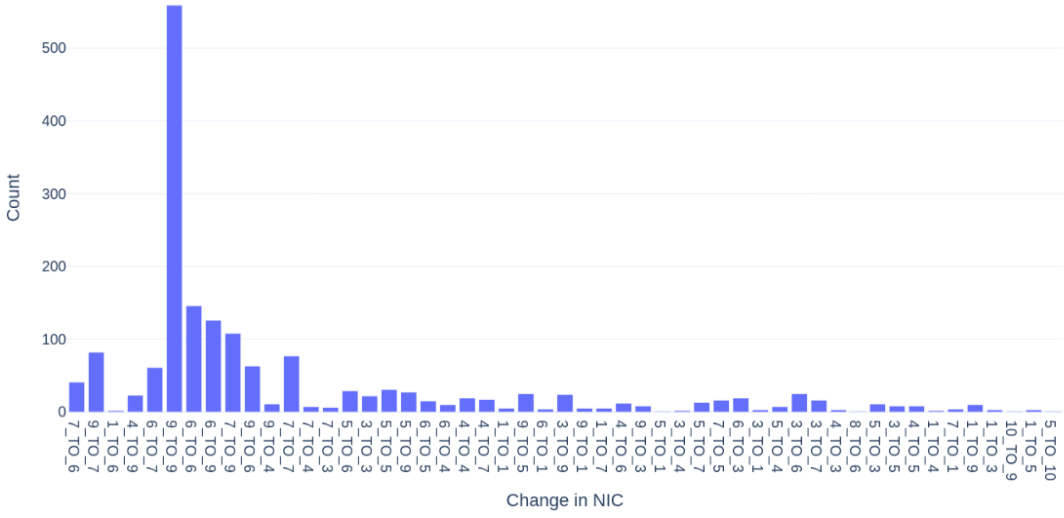

Figure 25. Count of change in NIC per category.

2.4.3 DFW Event by Aircraft Heading

Aircraft were analyzed by heading, and it was found that a drop in NIC of 7 or below was experienced by aircraft heading south-westerly and southern direction. Figure 27 and Figure 26 are polar bar charts where the bars represent the count of aircraft. These plots indicate that though the count of aircraft heading in various

directions is similar, a higher number of aircraft experienced a drop in NIC when heading in the south and south westerly direction.

Figure 26. NIC By Aircraft Heading.

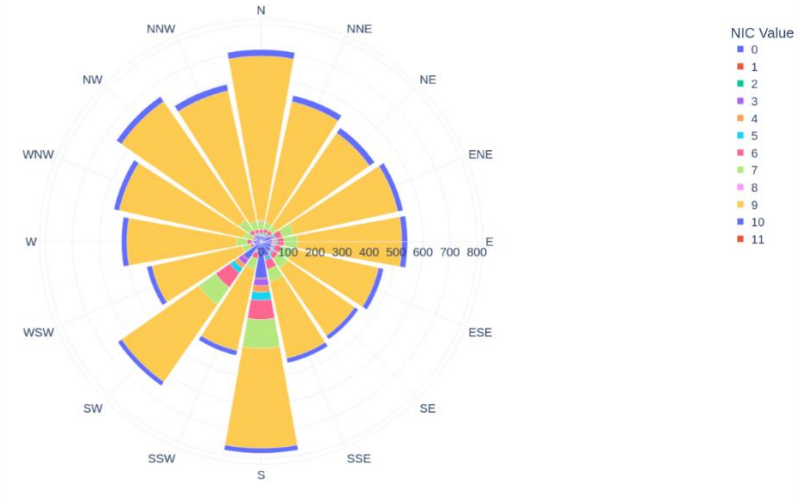

Figure 27. All NIC by Direction.

2.4.4 DFW Event by Areas of NIC Drop

The areas around DFW airport were analyzed using a hexagonal scheme to find paths taken by aircraft that experienced a drop in NIC. It was found from Figure 28 is that a Geo-Hexa plot enhances the visualization of this. The color of the hexagons indicates the count of unique aircraft per hexagon. The darker the color indicates more aircraft. The majority of the aircraft that experienced a drop in NIC were approaching from the north or northeastern direction.

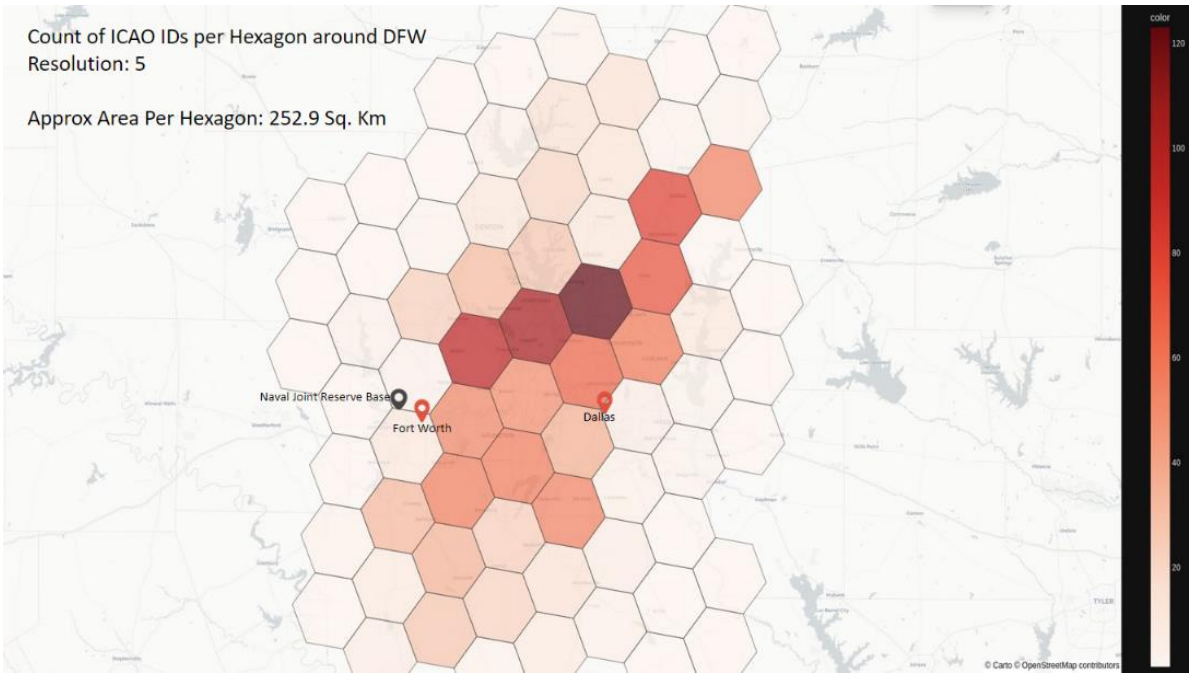

Figure 28. Geo-Hexagon plot of count of aircraft.

2.4.5 DFW Event Conclusions

Thus, through this use case, NIC is a reliable criterion for tracking GPS dropout rates or presence of interference. Further specific conclusions are as follows:

- For this use case, aircraft with altitude ranging as high as 9k– 13k meters were affected by GPS interference.
- The most typical change in NIC was found to be from 9 to 0 and recovery back to 9, followed by 6 to 0 and back 6 and 6 to 0 and back to 9. Further research is warranted to determine the exact cause. Some of the possible reasons for NIC values to go back and forth could be: 1. Intentional jamming/spoofing, 2. Unknown reasons, 3. Environmental/atmospheric interference 4. Interaction with nearby transceivers or satellite constellations affecting the ADS-B/GPS signal quality.
- In terms of heading, it was found that most of the aircraft that experienced a drop in NIC were heading in the southern or southwestern direction.
- By location, it was observed that the majority of the aircraft that experienced a drop were around the northeastern side of DFW.

2.5 Software Based Correction as a Potential Mitigation Approach

Although dropouts and erroneous data in GPS/ADS-B are rare and often intermittent, it is important to integrate robust software-based solutions for better situational awareness in national airspace irrespective of whether commercial or UAS environments. Two key solutions to mitigate such dropout conditions for precise navigation are recommended: 1) Imputation models for estimating

missed data points for guidance on possible latitude/longitude estimation and 2) trajectory planning for future time periods during non-availability of GPS conditions.

The goal of this section of the project is to investigate the ADS-B metadata from an open-source sensor network and use a machine learning framework to impute missing data points for GPS/ADS-B such as position, direction, etc. This section first reviews related work for imputation and then presents the dataset collection and features. Next, it covers the machine learning methods that will be used for this project. Lastly, the experimental section is where data analysis was carried out and the corresponding results are presented.

2.5.1 Dataset Collection

The data from the OpenSky Network ("The OpenSky Network - Free ADS-B and Mode S Data for Research" n.d.) were downloaded using a python script. The information was arranged by day and hour in each parquet file, which is a columnar storage file format optimized for big-data processing. The downloaded data was then organized by day and hour in individual parquet files. The researchers analyzed data collected from February 19 to 27, 2022, and which contained six flights that resulted in a total of approximately 60,100 data points. Table 9 illustrates the features column used in this study and the corresponding sample data format of aircraft recorded in the OpenSky database.

Table 9. Dataset Description of the OpenSky Dataset.

Field Name	Field Purpose	Sample Data Format View
time	The Unix (epoch) timestamp that OpenSky ADS-B Receivers recorded when an aircraft was nearby.	1479957078
icao24	The 24-bit ICAO transponder ID to track aircrafts.	780db8
lat	Last known latitude of the aircraft in decimal degrees.	118.59931
lon	Last known longitude of the aircraft in decimal degrees.	22.916793
geo-altitude	The actual height of aircraft above sea level in meters.	8839.2

2.5.2 Dataset Preprocessing

Pre-processing data aims to transform raw data into a more usable and effective format that is suitable for subsequent processing steps. In this scenario, each flight was divided into individual trips as a part of the pre-processing step. To define the trips, a threshold limit of 15 minutes was chosen, as the data obtained had challenges in accurately distinguishing between dropouts due to ADS-B receivers being turned off for shorter durations. The segmented trips for each flight were then saved as a separate parquet data file. These parquet data files, containing the individual trips of each flight, were used as input data to train ML models.

2.5.3 Imputation Methods

Figure 29 provides an overview of the ML framework utilized for imputing ADS-B and GPS dropout data. In this framework, PySpark, which is a Python API for Apache Spark, was employed for processing the feature columns. The percentage of missing values was introduced at different rates ranging from 10%, 20%, and 30% at random and continuous intervals. The missing values were then imputed using ML algorithms. After the values are derived using ML algorithms, they are forwarded to the validation section, which evaluates the performance of each ML algorithm using Mean Absolute Error (MAE) and Root Mean Square Error (RMSE) metrics.

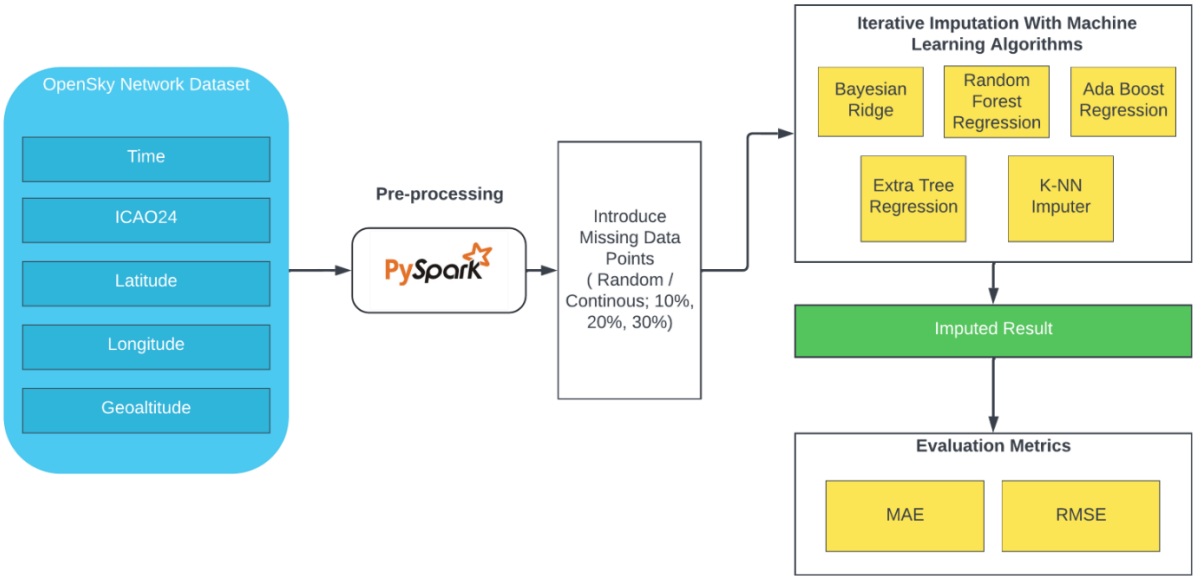

Figure 29. Overview of ML framework for Imputing Missing Data for ADS-B and GPS Dropout.

A detailed description of each of the imputation methods applied in this study can be found below. The Bayesian Ridge Regressor (BRR), Random Forest Regressor (RFR), AdaBoost Regressor (ABR), Extremely Randomized Trees or Extra Trees Regressor (ETR), and k-Nearest Neighbors (kNN) Regressor are a few of the regression methods employed.

- *Bayesian Ridge Regression (BRR)* is an estimator that uses a probability distribution technique to predict the target and uses L2 normalization to reduce the least-squares incorporating regularization element (Liu et al. n.d.).
- *Random Forest Regression (RFR)* is a supervised ML that uses an ensemble approach to predict the target variable by combining the predictions from multiple decision trees rather than using a single decision tree (Feng, Grana, and Balling 2021).
- *Adaptive Boosting or Adaboost Regressor (ABR)* is an estimator, which is a boosting algorithm where only the misclassified data points are iterated each time, and average weights are calculated to make predictions (Yang et al. 2021).

- *Extremely Randomized Trees or Extra-Trees Regressor (ETR)* is an ensemble approach where the collection of decision trees is constructed for random subsets of features. The decision rules are selected based on randomly drawn thresholds for each feature, and predictions are calculated as the mean prediction over the trees (Lee et al. 2022).
- *k-NN Regressor* calculates the difference between the target to the other values and estimates the value by interpolating based on the k-parameter (Zhang et al. 2018).

2.5.4 Imputation Results

Researchers randomly imputed the data, ranging from 10% to 30%, and applied various ML models with different hyperparameters as listed in Table 10. Hyperparameters for different ML models. The performance of these models was assessed using the MAE and RMSE metrics, which are defined in equations (1) and (2) respectively.

$$\mathrm{MAE} = \frac{1}{n}\sum_{i=1}^{n}|x_i - \hat{x}_I| \qquad (1)$$

$$\mathrm{RMSE} = \sqrt{\frac{1}{n}\sum_{i=1}^{n}\left|x_i - \hat{I}\right|} \qquad (2)$$

The results indicate that, regardless of the missing rates, Bayesian imputation did not significantly affect the metrics as the number of iterations grew. On the other hand, RFR produced better results, as the missing rate increases, but did not outperform kNN Regressor, since it gathers nearest points and imputes the result. Figure 30, Figure 31, and Figure 32 present a comparison of MAE scores for randomly imputed data from 10% to 30% for latitude, longitude, and geo-altitude. The MAE scores are computed using various machine learning algorithms, including Bayesian Ridge, Random Forest, AdaBoost, and Extra Tree, as shown in subplots (a), (c), and (e), and for kNN (distance and uniform) in subplots (b), (d), and (f) respectively.

Table 10. Hyperparameters for different ML models.

Imputation Methods	**Hyperparameters**	
	Name	**Value**
BRR	-	-
RFR, ABR, ETR	n_estimators	(10, 50, 100)
kNN Regressor	n_neighbors weights	(1, 2, 3, 4, 5, 10, 20, 30, 50) (distance, uniform)

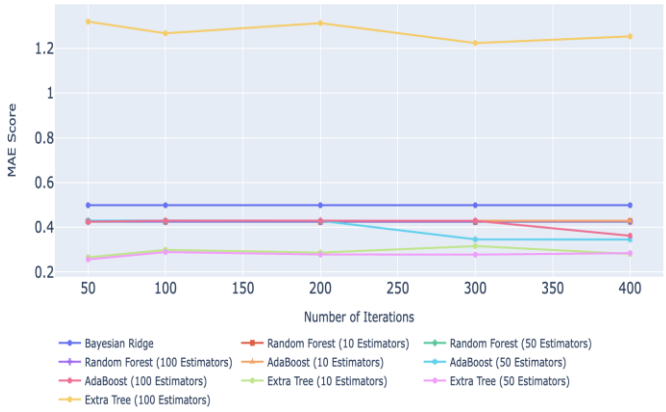

(**a**)

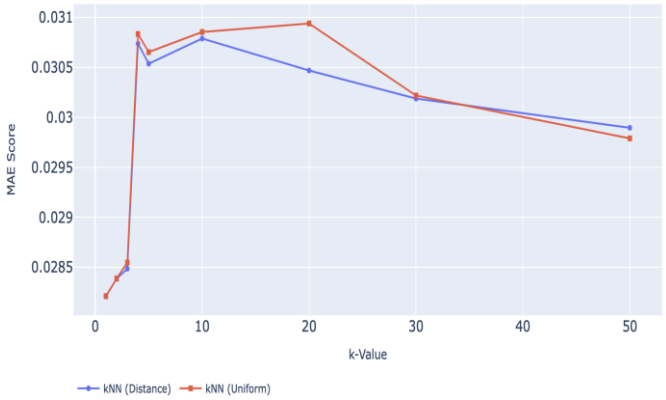

(**b**)

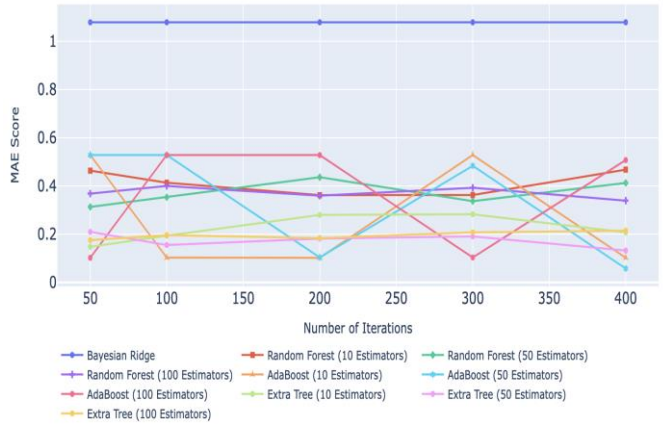

(**c**)

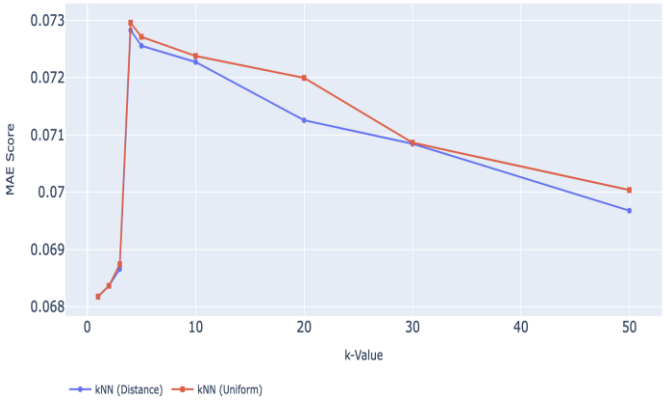

(**d**)

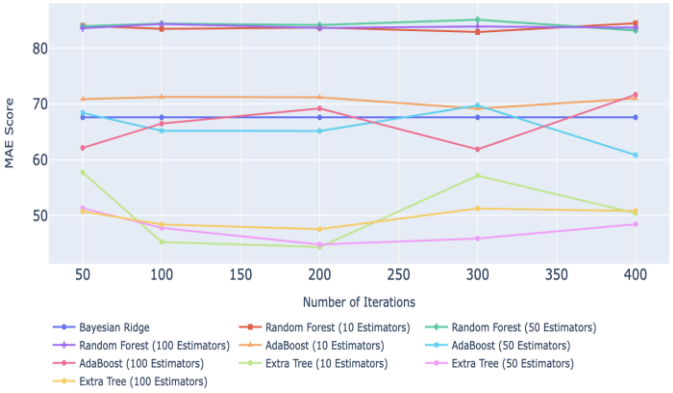

(**e**)

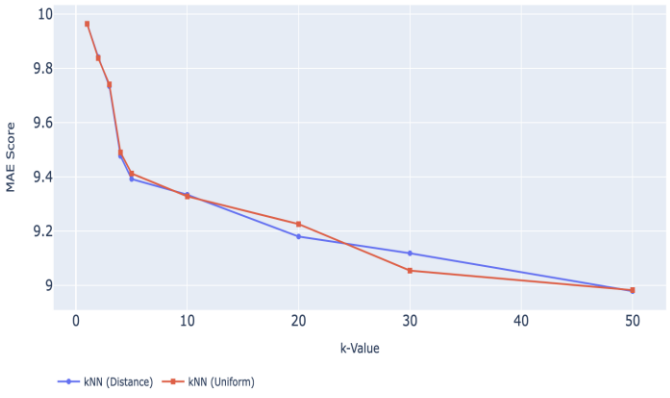

(**f**)

Figure 30. Comparison of MAE score for 10% randomly imputed data for latitude, longitude, and geo-altitude (a), (c), (e), using Bayesian Ridge, Random Forest, AdaBoost, and Extra Tree; and (b), (d), (f) using k-NN (distance and uniform).

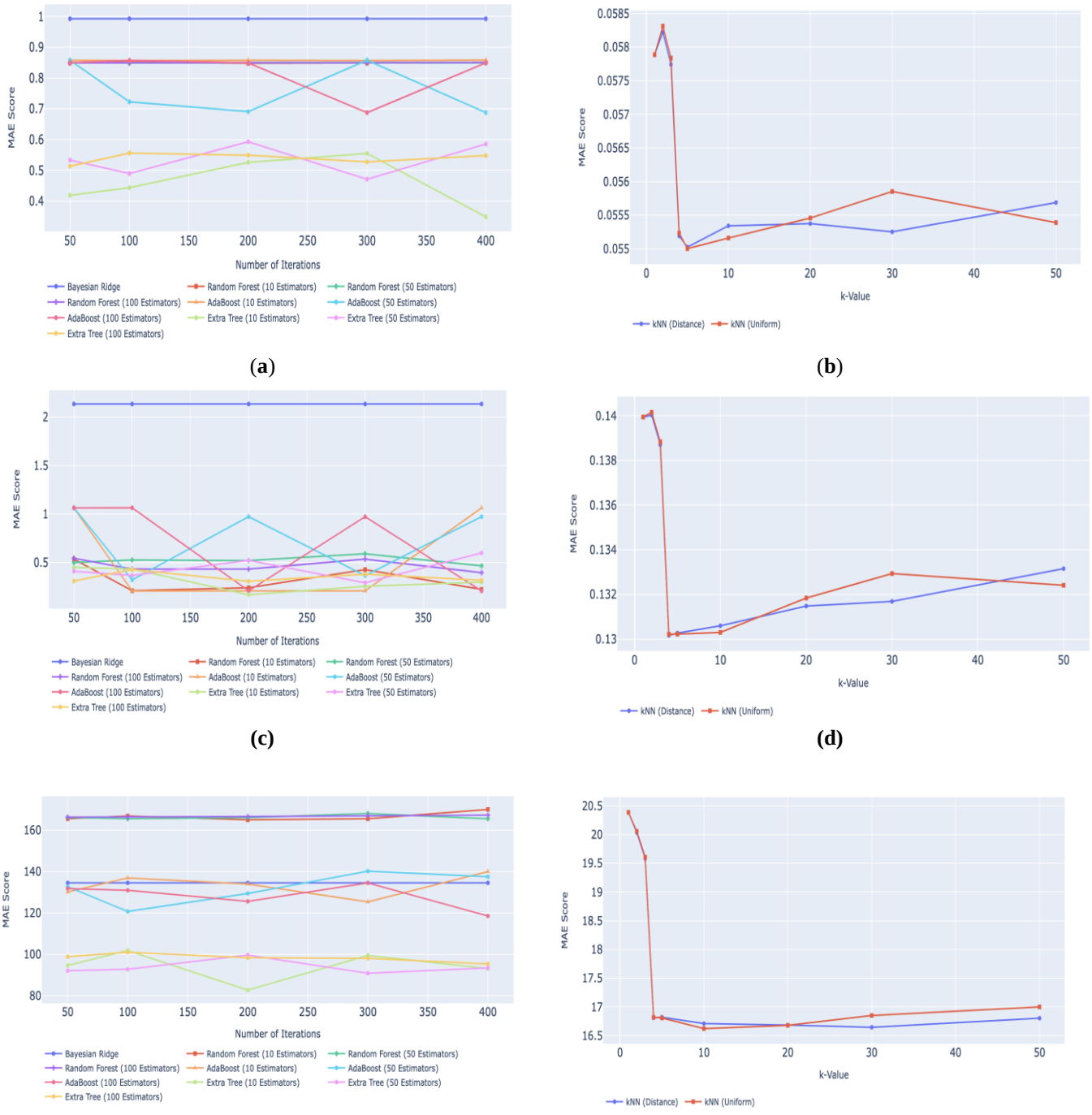

Figure 31. Comparison of MAE score for 20% randomly imputed data for latitude, longitude, and geo-altitude (a), (c), (e) using Bayesian Ridge, Random Forest, AdaBoost, and Extra Tree; and (b), (d), (f) using k-NN (distance and uniform).

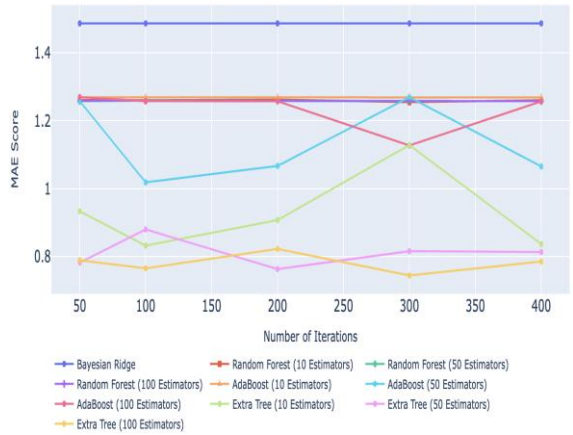

(a)

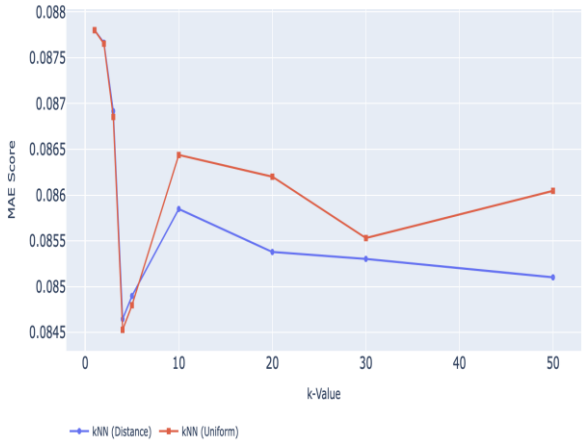

(b)

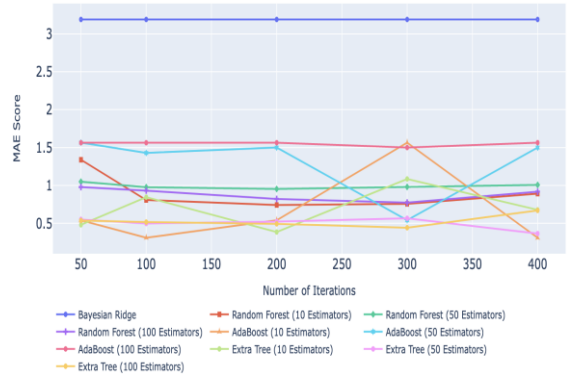

(c)

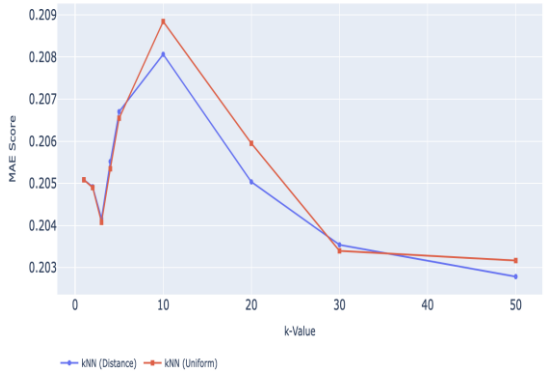

(d)

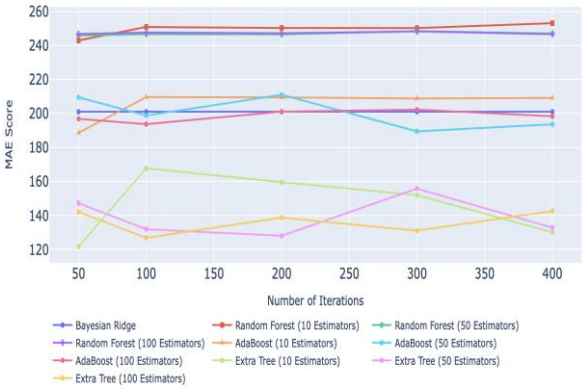

(e)

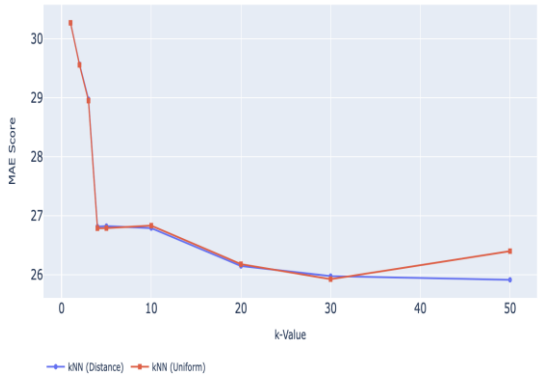

(f)

Figure 32. Comparison of MAE score for 30% randomly imputed data for latitude, longitude, and geo-altitude (a), (c), (e) using Bayesian Ridge, Random Forest, AdaBoost, and Extra Tree; (b), (d), (f) using k-NN (distance and uniform).

2.5.5 Imputation Conclusions and Future Work

This work explored the potential use of ML algorithms for imputing missing data points for ADS-B/GPS obtained from the Open Sky Network. In this study, five ML models - Bayesian Ridge, Random Forest, AdaBoost, Extra Tree Regressor, and kNN were used. The experiments were conducted by introducing various missing ratios of 10-30% for aircraft attributes (latitude, longitude and geo-altitude) and evaluated using the MAE/RMSE metrics. The results showed that kNN was the most robust model for missing data imputation while still achieving reliable predictions even in the worst-case scenario of 30% missed data points.

Overall, the use of ML techniques for imputing missing data points in flight trajectories has the potential to improve the accuracy of flight tracking and avoid collisions during GPS/ADS-B interference. For future work, the team recommends that authors test for scalability conditions using large data sets in a high-performance computing environment containing GPU nodes to validate flight patterns in real-time.

2.6 Trajectory Prediction

With the introduction of NextGen, the FAA mandated the ADS-B requirement for surveillance and improved situational awareness for commercial aircraft. Dropouts and erroneous data seem to be a prevalent issue of the ADS-B system, especially during GPS interference events. As a mitigation strategy for this dropout issue, the researchers propose a simple, non-parametric machine learning algorithm that uses an optimal window size to predict the position of the aircraft on a 30-second horizon. Through this work there is an improved ability to predict aircraft trajectories. Although the trajectory planning scenario considered is for commercial aircrafts, the methods proposed are deployable and applicable to UAS environments during interference scenarios.

Most of the current work that focuses on the prediction of aircraft trajectory seems to take a neural network-based approach that involves very complex and large models like convolutional neural networks, (Long Short-Term Memory (LSTM) networks, and a combination of the two. However, none of the research has applied simpler non-parametric models towards the prediction of trajectories. Using the previously mentioned DFW-interference dataset, the intent is to create a model using a simpler non-parametric method. The main reason for the selection of a non-parametric model is that parametric model makes strong assumptions about the data being used to train the machine learning model like normality of data. Since the normality cannot be tested on the data used, which consists of latitude and longitude, the non-parametric models will be used as they do not make such strong assumptions about the training data. Most of the methods applied in previous work seem to use multiple parameters like heading, speed, latitude, longitude to make predictions. However, testing the hypothesis that by using only latitude and longitude to predict the future latitude and longitude and latitude, would perform better, because parameters like heading, and velocity are indirectly captured in by the position of the aircraft. For example, consider an aircraft that is heading perfectly north, this would cause only the latitude of the aircraft to change, while the longitude would remain constant. As with the case of an aircraft that travels perfectly east, that would cause a change only in the longitude, while the latitude remains constant. Aircraft travelling with a higher speed would have a higher rate of change in the difference in latitude and longitude. Any change in speed would be

reflected in the subsequent positions. A non-parametric model called the kNN regressor was tested for effectiveness. The main idea would be to understand the effect of dropout and window size on the prediction accuracy of the model.

2.6.1 Trajectory Data Preparation

The windowing technique was applied to create trajectories of aircraft using historical data. The overall window size used to create the dataset was 90 seconds. The first 60 is intended to be used for predicting the next 30 seconds.

The pseudo code for the logic used to create the dataset is:

```
Set history_size = 60
Set pred_size = 30
Set sel_features = ['lat', 'lon', 'velocity', 'heading', 'geoaltitude', 'vertrate']
Create empty lists X_collection and y_collection

For each unique value anicao in main_df['icao24']:
   Filter icaodf from main_df where 'icao24' matches anicao
   Sort icaodf by 'time'

   For i in the range from 0 to (length of icaodf - (history_size + pred_size) + 1):
      Create total_window by selecting rows from icaodf starting from i and spanning (history_size
+ pred_size)
      Remove duplicate rows based on 'lat' and 'lon' in total_window

      If there are no time differences greater than 1 in total_window and
        there are no missing values in any of the selected features in sel_features and
        the total_window has a shape of (history_size + pred_size):

         Create hist_window by selecting the first history_size rows from total_window
         Create pred_window by selecting the remaining pred_size rows from total_window
         Append hist_window to X_collection
         Append pred_window to y_collection
```

Running the logic on the entire dataset of 157805 datapoints (2557 flights) resulted in a total of 23,314 windows. This will be used for training the model.

The computer used to train the model had the following specs:

Operating system: Ubuntu 18.04.

Processor: Intel(R) Core (TM) i9-9920X.

Memory: 134 GB DDR 4.

Graphics Card: 4 x NVIDIA GeForce RTX 2080 Ti.

The libraries used to run the experiment are:

Python: 3.9.16.

NumPy: 1.24.2.

Sci-kit Learn: 1.2.1.

PyCharm Professional (IDE): 2023.1.2

2.6.2 Trajectory Experiment Design Objectives

The overall objective is to find an optimal and accurate trajectory prediction model during normal and varying dropout conditions.

Several machine learning models were investigated and the kNN Regressor is the most promising model for trajectory planning and forecasts. This is due to kNN Regressor does not depend on any data distribution and outliers will have no influence as its prediction are outweighed by nearest neighbors.

A fresh instance of the kNN Regressor for different window size with hyper parameter tuning is trained on the dataset in a loop using only latitude and longitude, and the predicted features are also latitude and longitude. The loop maintained the size of prediction and model parameter grid, while varying the input size from 6 to 30, in multiples of 6. The parameter grid in Table 11., is used to tune the model using random search. For the random search, researchers set 6 cross validations for each iteration and the number of parameter settings sampled is set to be 12. The results are recorded in terms of MAE – Latitude and MAE – longitude. These will then be converted to meters, to make the results more interpretable. The elbow technique is used to determine the optimal window size for this problem.

Table 11. kNN Hyperparameters.

Parameter	**Values**
Number of neighbors	1, ***2*** …, 30
Weight function	***uniform***, distance
Algorithm	Auto, ball tree, ***KD Tree***, Brute
Leaf Size	***10***, 20, 30, 40, 50
P (Power parameter for Minkowski metric)	1, 2, ***3***
Distance metric	Euclidean, Manhattan, ***Minkowski***

The best model from the window size experiment will be used, while running it in a loop, randomly dropping a set percent (from 10 to 50) of values from the prediction set while holding the windows size as a constant. The dropped value will be replaced by the previous value in order to maintain the input size. The values dropped will be continuous, and for every x window, there will be one drop out. MAE values will be used as a metric to understand the effect of these injections.

2.6.3 Trajectory Experiment Design Results

The results of running the model in a loop for different prediction windows are visualized in Figure 33. The figure shows the window size used for prediction on the X-axis and the MAE converted to meters on the Y-axis. On observing the drop in error, note the elbow forming at the third bar (window size 18). Though the error does reduce beyond this point, the reduction is not as significant as the previous increments. A strong elbow is observed at the 18 second window. At this window duration, the MAE of latitude and longitude converge, and the error in latitude seems to increase and remains above the error in longitude. The best parameters as chosen by Random Search for a window size of 18 are the highlighted values in Table 11.

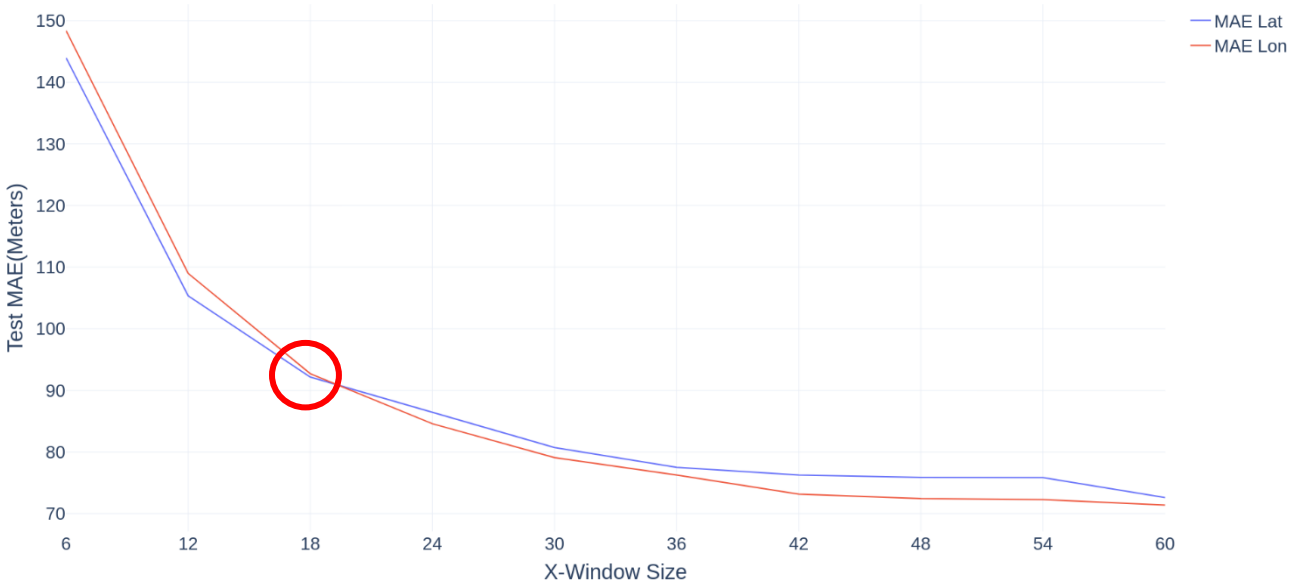

Figure 33. MAE in meters Lat and Lon, kNN Regressor.

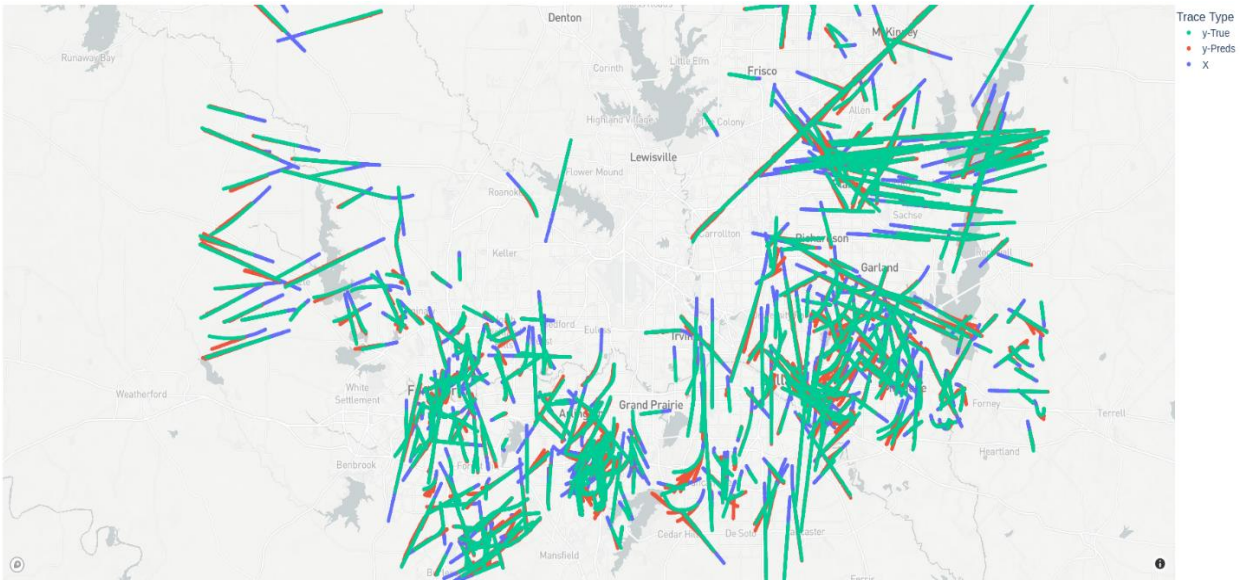

Figure 34. Trajectory Prediction.

Figure 34. is a geo-scatter plot that visualizes the trajectory results. There are three different types of traces in this visualization, the y-true is the accrual trajectory, the y-preds is the predicted trajectory and the X is the history used to make the prediction. It is observed that the model seems to perform well even at some instances where the aircraft has made turns.

The percentages of 10, 20, 30, 40, and 50 account to a total of 2, 4, 5, 7 and 9 data points when rounded off to the nearest integer. By inducing these dropouts, the errors in predictions grew. This is visualized in Figure 35. It is a bar graph with the X-axis as the number of seconds of dropout and Y-axis as the error caused in the MAE of the test data, in meters.

2.6.4 Trajectory Experiment Design Discussion

Through iteration of various window sizes, it was determined that the optimal window size for this use case was a prediction size of 18 seconds to predict a window of 30 seconds. The accuracy for latitude and longitude is about 90 meters. With the best parameters and window size found from this experiment, the effect of dropouts is studied by manually injecting drops of various sizes into the data. It was found that the accuracy deteriorated very rapidly for dropouts beyond 2 seconds.

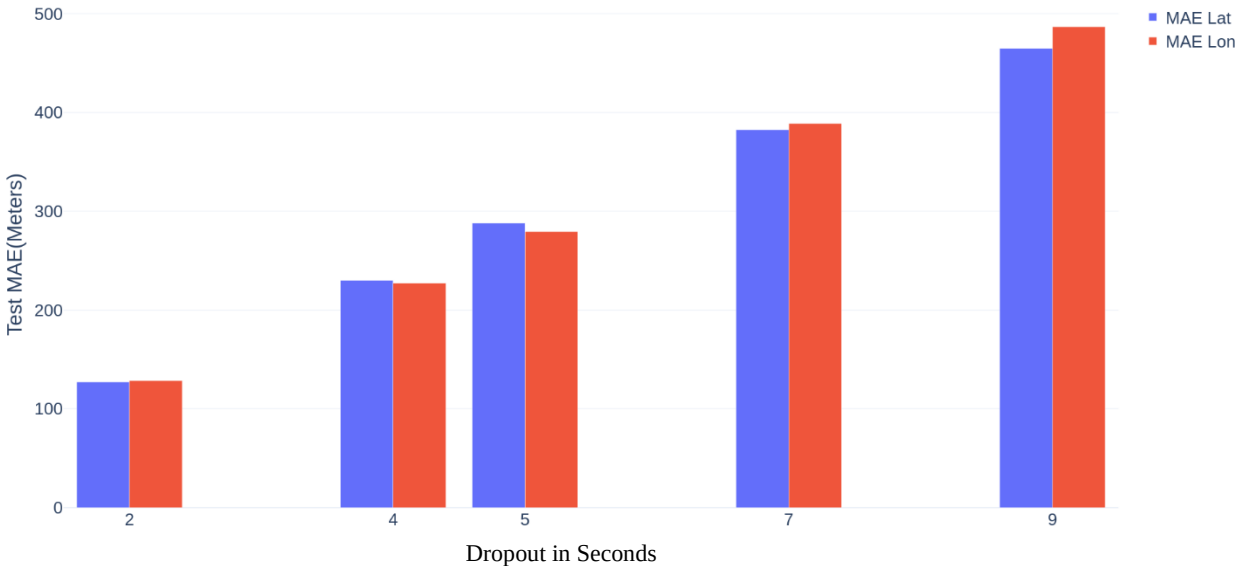

Figure 35. Effect of dropouts on MAE.

There were several limitations found including:

1. The data used for the training and prediction of trajectories is confined to an area of 6400 square NM around Dallas. This model has not been tested on data from other hemispheres.
2. The cleanliness of the data used for training has not been manually assessed by accessing every datapoint but are filtered using the logic mentioned in the pseudo code.
3. The method focused on experimenting with the kNN Regressor that was implemented by sci-kit learn, other implementations were not tried.
4. The computational resources and time for the prediction have not been taken into consideration, while the model is accessed purely based on the prediction accuracy.
5. The conversion of MAE to meters is based on an approximation of latitude and longitude minutes.

2.6.5 Trajectory Conclusions and Future Work

The findings indicate that there is a need for a precise trajectory planning model during GPS/ADS-B interference and the proposed kNN Regressor approach can yield significant accuracy in estimating latitude and longitude up to 44m proximity for each parameter. A use case of DFW-event containing a training set of 2550 flights was demonstrated, but to evaluate the proposed model in real-time, it needs further testing in a multi-cloud environment containing High Performance Computing (HPC) resources for accurate error metrics.

3. CELLULAR NAVIGATION

The use of cellular navigation to mitigate the risk of jammed GPS and/or ADS_B data was investigated. In the event of a GNSS signal loss due to obstructions, multipath, or intentional/unintentional jamming, the UAS's positioning performance is degraded. Depending on the duration and severity of the interference, the onboard IMU system can reasonably maintain the planned course for seconds or even minutes after the event, depending upon the quality of the IMU and/or integrating it with other sensors; otherwise, loss of the UAS control link and navigation systems occurs, posing a risk to the mission and/or the safety of bystanders. Furthermore, even the presence of ADS-B In port in the UAS cannot detect and avoid other UAS nearby due to the constrained GNSS position.

Introducing an additional sensor to inform and diversify the UAS navigation architecture can act as a backup or supplement positioning solution in the case of GNSS jamming or dropout, thus increasing the capacity for the UAS to both complete a mission and maintain accurate and reliable ADS-B data in challenging signal scenarios.

Signals of Opportunity (SoOPs) offer promising candidates for this mitigation approach, utilizing existing signals from the surrounding environment of operation. Cellular infrastructure in the United States comprises of multiple network providers and associated transmission towers, with overlapping coverage in most populated regions. In the framework of small UAS operations, cellular signals as SoOPs provide the benefits of (1) increased signal strength, and wider frequency spectrum in relation to GNSS, (2) good geometric diversity, associated low processing load and payload weight burden, (3) future potential for expanded UAS-cellular integration in the framework of BVLOS operations, as well as (4) a widely established usable network infrastructure.

Considering the potential risks to UAS operations due to the erroneous, dropped, or jammed GNSS data; this section aims to explore Cellular Positioning as a potential mitigation. Oregon State University (OrSU) reviews cellular and navigation theory, in addition to investigating preexisting cellular positioning approaches within the literature. An explorative field study was performed utilizing nearby LTE cellular signals in varying UAS flights in collaboration with UAF. Test findings, project recommendations, and possible future work are summarized.

3.1 Cellular Navigation State of the Art

The potential for cellular signal positioning techniques have been primarily explored in the context of land-based or indoor application, such as autonomous vehicle or pedestrian navigation. Theoretical UAS-based positioning algorithms have been tested through simulations. The development of Software Defined Receiver (SDR) architecture geared towards real time processing techniques has been proposed (del Peral-Rosado et al. 2013; J. Khalife, Shamaei, and Kassas 2016). However, actual UAS-based flight test case studies are sparse in the published research space, contextualized below:

Position estimation is based on a trilateration technique where range measurements from four or more beacons of known location are used to calculate the absolute position of the receiver. Within the framework of cellular-based navigation, three prominent techniques exist to estimate range between a cell transmission tower and cellular receiver exist in the literature:

1. Signal time of arrival
2. Signal direction of arrival
3. Received signal strength

These techniques can be leveraged with the different generations of cellular signals, and in user-based or network-based navigation approaches. Uncertainty thresholds vary based on the given approach, flight, and processing parameters- the simplest approaches, such as received signal strength, is estimated to be hundreds of meters. For more precise approaches such as carrier phase time of arrival positioning, case studies demonstrate potential meter or submeter accuracy in near urban environments based on flight testing (Abdallah and Kassas 2021; Shamaei and Kassas 2019; J. J. Khalife, Bhattacharya, and Kassas 2018). However, testing cellular positioning is still in the experimental phase with no commercial systems readily available.

An experimental UAS payload testing cellular positioning techniques generally includes an SDR platform to facilitate the processing of cellular signals, along with a cellular antenna or antenna array. These components can be costly to purchase and implement, as well as posing additional weight requirements for Part 107 and sUAS platforms. However, open source, 4G capable UAS currently exist off the shelf that could be utilized for testing cellular positioning (Parrot 2021). Additionally, 5G capable UAS have been released and are projected to increase in availability as 5G network infrastructure progresses (Qualcomm 2022).Assuming open-source integration of cellular hardware continues to advance, additional cost to the UAS unit would be much lower in the framework of testing, and potentially utilizing, cellular navigation.

Assuming a cellular-integrated positioning system on a UAS, and four or more consistent cell towers within signal range, an exclusively cellular positioning solution can be achieved. Given current estimated uncertainty of precise cellular approaches, and the likelihood of superior GNSS availability and position accuracy in flight operations outside of an interference event, it is likely most practical to consider cellular SoOPs as a supporting (hybrid) or backup positioning source to GNSS.

3.2 Future Potential for Cell Integrated UAS and BVLOS Flight

Separate from the scope of positioning, cellular networking has been a popular topic in relation to the future of UAS commercial operations. Where most current UAS regulations limit flight to Visual Line Of Sight, and market-available UAS primarily utilize radio frequencies as a command link; innovations, and adoption of cellular networks (most prominently 5G) as a communication platform introduce new possibilities for BVLOS flight and expanded operation in urban areas for the commercial UAS industry. Specifically, infrastructure for UAS 5G corridors are being tested for BVLOS commercial operations in dense, urban areas (sUAS news 2021).

These trends and interests point toward existing and expanding UAS-related cellular infrastructure. If cell networks are an established command link platform in future BVLOS flight operations, cellular receivers would be more commonly integrated on commercially utilized UAS in the large scale. 5G (and other cell generations) signal availability in the case of BVLOS missions would be theoretically consistent throughout the planned route or designated flight perimeter.

3.3 Cellular Navigation Experimental Testing

The objective of this experimental study is to record and utilize nearby LTE/4G cellular signals from a UAS-based receiver and integrate with available GNSS signals to inform and assess a positioning solution. A hybrid scenario is depicted in Figure 36 where the aircraft receives GNSS signals from three of the four satellites as one satellite's signal is occluded by a building. Thus, rendering a GNSS position estimation is not achievable because the minimum required GNSS satellites for positioning is four. In the case of a cellular-integrated UAS, signals from two available terrestrial cell towers can be utilized along with the three GNSS satellites to estimate the aircraft position.

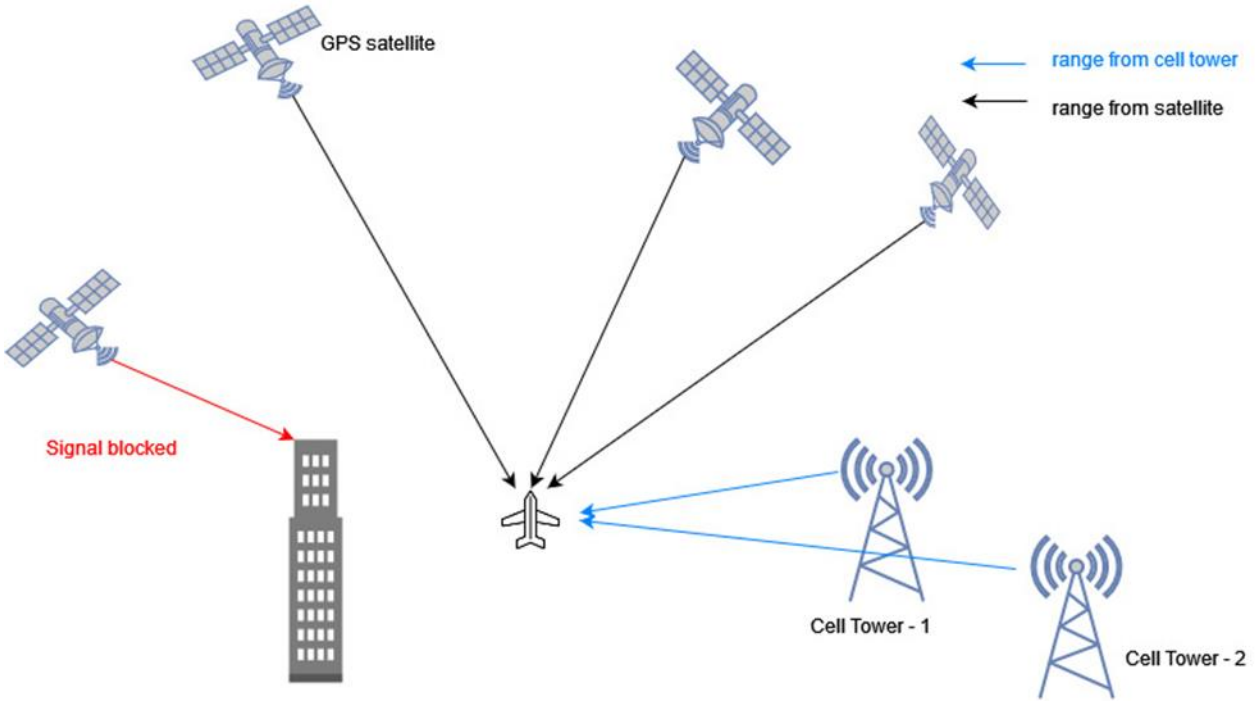

Figure 36. Conceptual diagram of cell towers augmenting GNSS positioning of an aircraft when a satellite signal is blocked.

Given the constraints of the project timeline and equipment budget, the OrSU team adopted the signal strength-based range estimation approach for the experiment. Received signal strength-based range estimation involves minimal hardware complexity, as radio systems commonly measure and report received signal strength, though the approach produces a lower accuracy threshold compared to other presented methods, in the range of hundreds of meters.

OrSU investigated this topic within Tasks 3 and 4 and collaborated with the UAF team to conduct flight testing and manage UAS and sensor equipment logistics. OrSU performed the data processing, interpretation, and discussion components using the measurements collected from the onboard sensors.

A market-available network cellular scanner was acquired by UAF to complete this flight test, capable of logging all available bands and subchannels in semi-real time (Figure 37). The supporting sensor, a high-rate, multi-constellation GNSS receiver paired with a dual band antenna was used for GNSS logging.

Figure 37. Epiq Solution's Prism scanner and omni-directional antenna (detached).

UAF leveraged a Pixhawk-operated hexcopter UAS for flight tests, integrating the two sensors onto the payload (Figure 38).

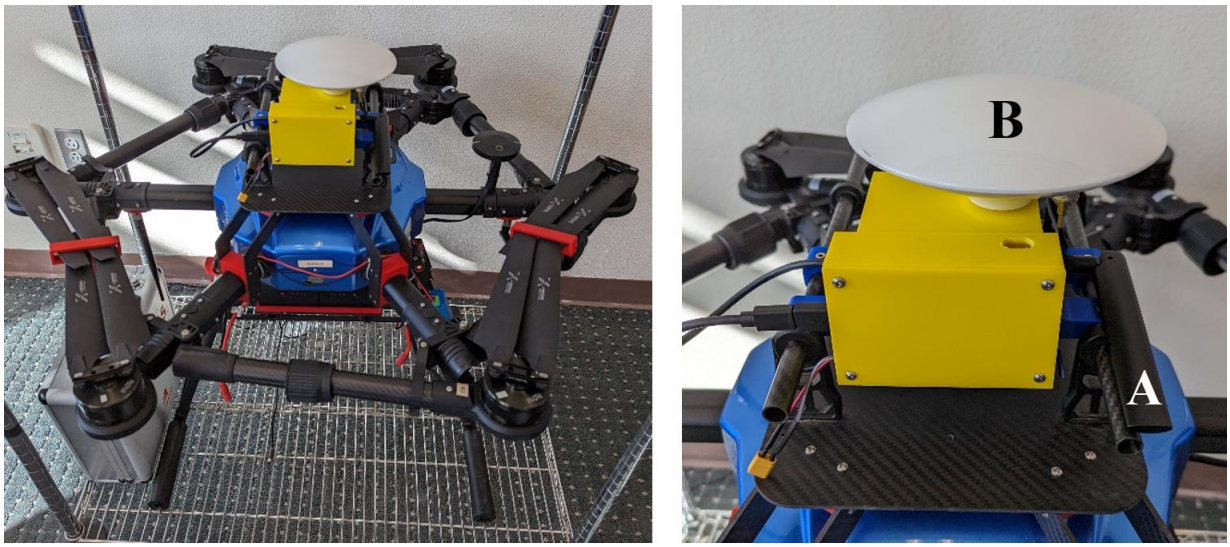

Figure 38. Images of flight test vehicle (left); cellular (A) and GNSS (B) antennae on payload.

Using the received signal strength and the transmitted signal strength, the path loss between the cellular tower and the UAS can be calculated to estimate distance. Various models exist to define the relationship between the path loss and the range, depending on the radio signals frequency, and the properties of the medium/environment in which it travels. The Hata path loss empirical model was

used to calculate range from path loss due to its frequent adoption in cellular positioning literature, as well as its applicability to a small city environment.

The range solution calculated using the Hata path loss model is combined with the range measurements from the GNSS satellites to estimate a hybrid navigation solution. In this experimental study, the team utilized the combined range estimates from GNSS and cell towers for a simple linear least squares technique, to estimate the UAS position.

3.4 Data Acquisition and Analysis

Four data collections campaigns were conducted during the testing phase of the project. The first two acquisitions were completed as preliminary assessment of the signal environment and scanner logging behavior, which informed flight test planning, and allowed for workflow development of locating signal transmission sources through a cell tower matching, which is described in the next section.

The third acquisition session included the primary flight tests. Three static occupations of 6-10 minute duration at 15ft, 150ft, and 400ft AGL were manually flown and logged in a designated flight area (Figure 39).

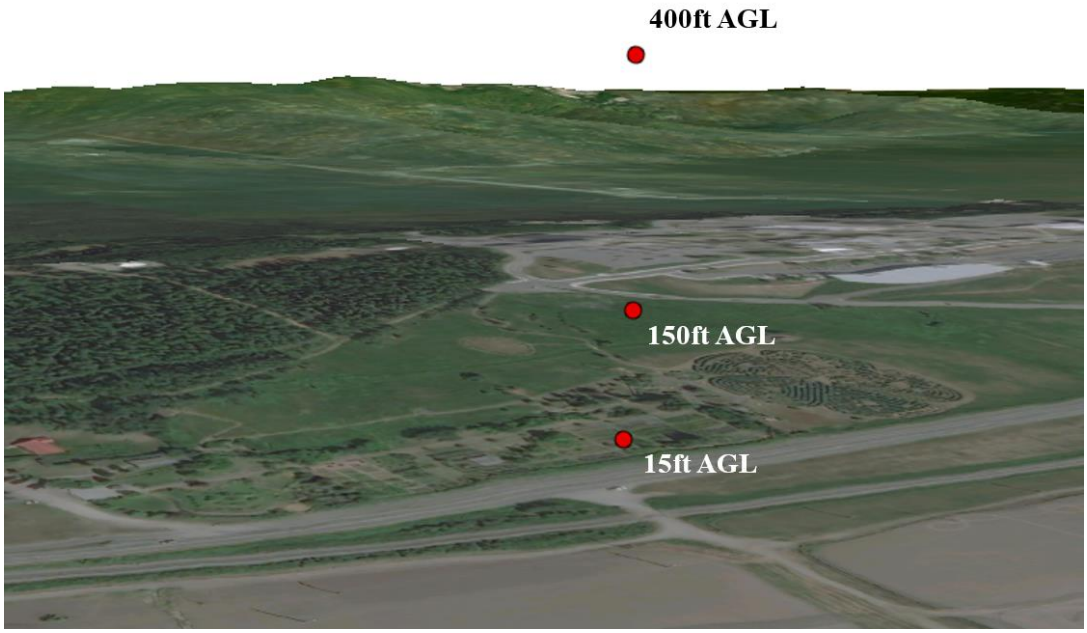

Figure 39. 3-D scene of the manual static observations collected SW of the UAF campus.

Early preprocessing of test data identified hardware limitations affecting logged cellular data, including reduced sampling rate and obstructions inherent to the UAS payload. The challenges prompted a final standalone cellular collection to confirm the hardware bias, and recontextualized the position estimation results for this experiment.

To calculate range from existing path loss models, the location and height of the signal source, or cell, also needs to be known. While the onboard cellular scanner collects signal information from all mobile network provider towers within range, the only tower-related information logged is the unique cell ID, which provides no explicit details related to signal origin. Communication tower construction and modification are regulated and documented by the Federal Communications Commission, and in the state of Alaska, by the local Borough. Tower permit records for all communication infrastructure currently in operation and within 10km of Fairbanks city limits were obtained from both sources. These documents provide reliable location coordinates for towers that meet the criteria of the search parameters, as well as tower height, but still no directly related fields to match with the cell ID acquired in flight tests.

Two open access, crowd-sourced cell tower databases were identified as potential intermediary resources for matching together the cellular logs and permit-documented locations. Similar to a cell and its designated cell ID, each tower has a standardized unique identification number named eNodeB ID (eNB ID), which can act as the intermediary field needed. Using both databases and a browser-based eNodeB ID conversion tool, tower cell IDs were able to be matched to permit tower location, through crosschecking on public mapping software and street view imagery. Figure 40 depicts a subset of identified towers surrounding the flight test area, logged from the preliminary ground collection.

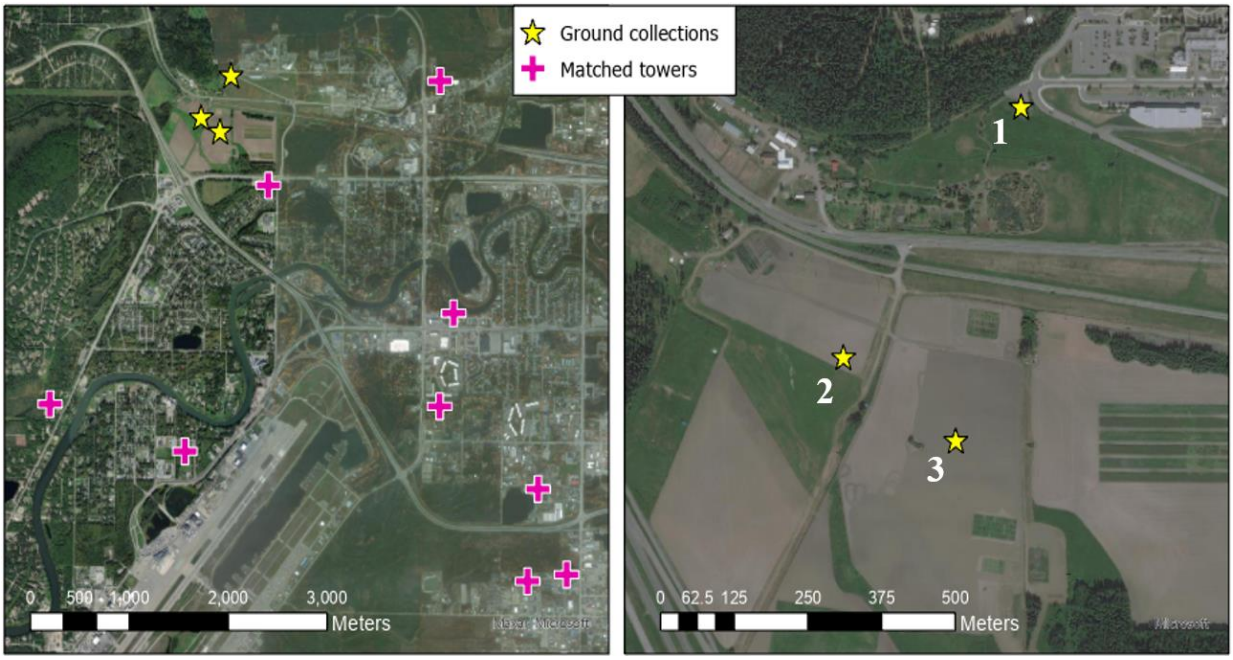

Figure 40. Subset of local towers identified and matched from preliminary ground collections.

Despite sub-optimal signal clarity during the flight trials due to hardware restrictions identified in Task 4, researchers performed a simplified UAS position estimation to simulate a loss of signal from a GNSS satellite, out of four satellites flight scenario, which can frequently occur in an urban canyon or interfered environments. The approach was accomplished through post-processing, as a proof of concept, but can be applicable for onboard real-time implementation.

Using data from the 150ft AGL static occupation, researchers selected a cell tower that had the least range error to the UAS. Two case studies are pursued in which UAS position is estimated using:

1. 4 GPS satellites.
2. 3 GPS satellites and 1 LTE tower.

The true position of the 150 ft flight, the position estimated using 4 GPS satellites, and the position estimated using 3 GPS satellites and 1 LTE tower are shown in Figure 41. Note that the position estimation with only 3 GPS satellites cannot be obtained mathematically but augmenting the algorithm with the range estimate from a single tower, one can determine the position of UAS. The position error for this single epoch-based estimation is 594 m, considering the noisy range estimates from the cell tower, as well as the non-availability of other nearby LTE towers due to the challenged antenna position.

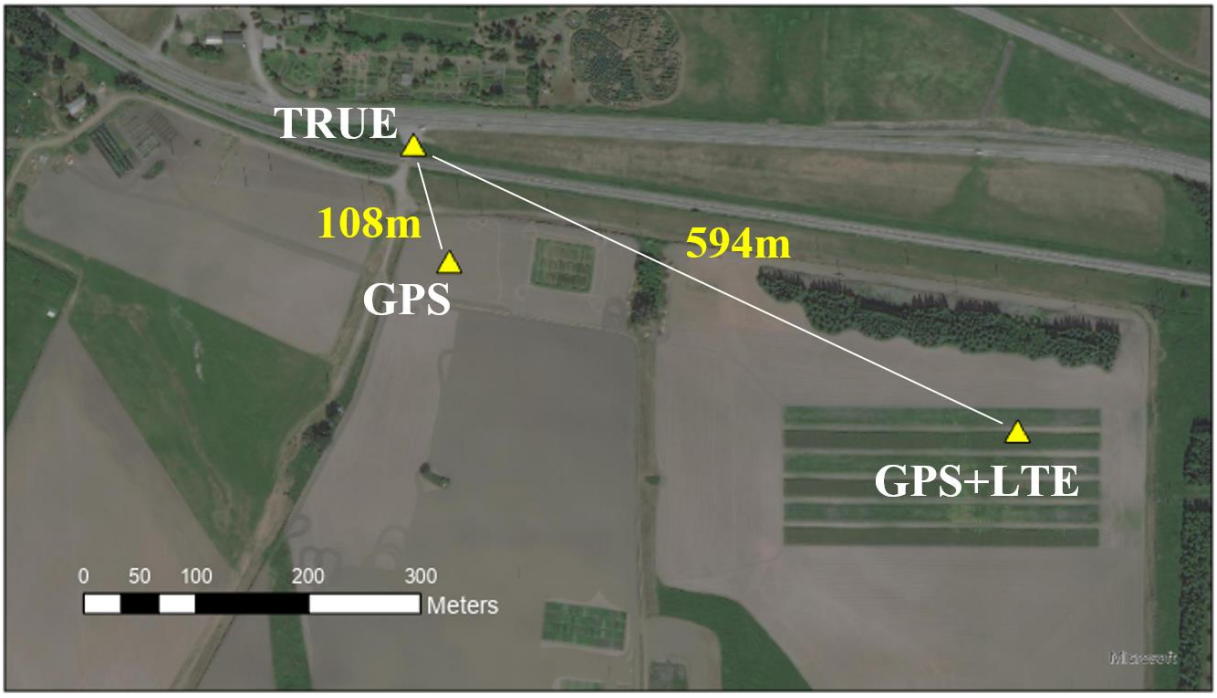

Figure 41. Position estimate results for the 'challenged' 150ft flight, in case of 3 available GPS satellites.

Considering summarized accuracy thresholds for the signal strength method, this result shows potential, in specific scenarios, to augment or aid the GNSS based positioning with measurements from LTE towers in a non-challenged antenna scenario.

3.5 Summary of Cellular Navigation Findings

Though hardware and logistical components limited the flight and processing potential for a true signal strength-based method in Task 4, productive characteristics and methods for leveraging cellular signals as a UAS-based navigation source can be identified from the case study.

1. RSSI-informed cellular positioning approaches fundamentally yield an accuracy threshold in the range of hundreds of meters, in-line with results found in the flight data analysis. This level of uncertainty can be utilized in very specific dropout conditions but is too high for practical and reliable application in real-time UAS operations. However, it remains to be seen if further improvements can be made to this result without the reported hardware limitations.
2. Tower location matching was a particular challenge in this experiment due to the lack of public resources for identifying the source cellular towers and their properties (e.g., height of antenna etc.). In the ideal scenario of achievable accuracy in a cellular-based approach, an efficient method of locating and characterizing cellular tower parameters is still required to calculate a solution, especially in the framework of real-time navigation. This report outlines the available resources and a viable, manual approach to match local towers through intermediary cross-checks and redundant datasets, successful for the scope and scale of the tests conducted in Fairbanks, with likelihood of applicability to areas in the US of similar or greater population density and development.
3. Current and region-specific cellular infrastructure provided sufficient signal overlap in flight scans for this study area. When surveying the occurrence of unique visible cell IDs recorded during scanner occupations, cell ID counts from the 150ft and 400ft sessions were significantly higher than the 'clean', standalone, on the ground PRiSM collection; even considering the two to three times shorter flight occupations, and cellular antenna visibility obstructions associated with the UAS payload. This indicates that existing 4G cell infrastructure can provide usable signals of opportunity throughout the current sUAS vertical flight space of 400ft altitude and below. Assuming this is true in a given location outside of the study area, it could be plausible to broadly consider most environments semi-ideal for eavesdropping on cell signals. Exceptions would notably include the urban canyon, or regions of high topographic variability, where obstructions create a challenging multipath environment even at higher AGL elevations. However, current projections of 5G infrastructure in urban environments could involve a dense next generation cellular network that could be considered for such scenarios in future UAS cellular navigation.

3.6 Cellular Navigation Recommendations

Based on reviewed literature and the explorative study conducted, precise cellular signal positioning approaches show strong potential for mitigating risk in UAS-based commercial operations and should be further considered as a supporting or backup navigation source in the case of GNSS signal dropout or jamming.

The primary considerations for this conclusion include (1) the published potential for meter to submeter accuracy in time-of-arrival approaches, (2) practicality and plausibility of cellular receiver utilization in current and future UAS hardware, (3) the signal coverage of typical UAS operation flight space currently available from existing cellular infrastructure, and (4) future potential for cellular positioning in challenging urban environments in lieu of 'smart cities', possible dense 5G communication networks.

Specific recommendations include:

1. To achieve effective, real-time cellular positioning onboard a UAS, integration of a cellular system is required on the hardware and software level. Future FAA funded research on developing such systems, or FAA-sponsored market incentives for open-source UAS systems can cultivate a space for further development of this mitigation approach on the large scale.
2. Acquiring cellular transmission tower characteristics and location is a vital component of producing a position solution. While an effective manual approach towards identifying these values is presented in this report, it is time intensive, reliant on crowd-sourced information and physical public records, and not plausible for real-time processing applications.
    a. For cellular signaling to plausibly be utilized in commercial UAS operations, a publicly accessible, or partnership-specific database of cellular transmission towers would need to be established and regularly updated to inform successful navigation systems.
    b. Another approach is for the cellular towers to transmit its location as part of its system message which any mobile/cellular scanner can read. This would be similar to how GNSS satellites transmit its location in the navigation message. However, unlike the GNSS satellites which need to be regularly tracked from the ground stations to determine its position, the cellular towers being stationary can be surveyed once to determine its location. This would provide a highly precise tower location to all the mobile units in a particular cell. Technical feasibility to implement this requirement as well as legislation can help to proliferate cellular based navigation.
3. Future legislation decisions expanding legality of commercial BVLOS flight, or permissions related to commercial UAS flight corridors within dense urban areas, will likely accelerate cellular infrastructure networks and market UAS integration with onboard cellular signaling hardware; indirectly creating more potential viability for the implementation of the presented mitigation.

3.7 Cellular Navigation Future Work

Based primarily on the limitations and challenges faced within the flight test and processing component of this project, within context of the available literature relating to UAS cellular navigation; recommendations of future work include:

1. Continuation of the tests flights and processing originally outlined for this project's Task 4 component offer an opportunity to produce more refined results. Further iterations of payload orientation could improve consistency of signal strength readings to produce more accurate results in context of established RSSI benchmark levels. Recent firmware updates to the cellular network scanner have improved the filtering performance. Implementation of automated flight plans and longer occupation times may reduce additional bias, while testing a broader variety of positioning approaches and scenarios.
2. With a longer-term project scope and equipment focused budget, more precise positioning methods can be developed and tested as a closer analogue to practical uses of cellular-based UAS navigation. Cellular and SDR architecture integrated onto a sUAS would create potential for testing the published meter level accuracy, in real time. Use of 5G signals in similar tests could speak to

challenges and benefits of the platform for use in the urban canyon environment, assuming a dense network infrastructure.
3. To assess viability of cellular infrastructure on a nation-wide scale, a survey of all domestic cell towers and associated characteristics could be conducted. A GIS analysis of signal radius zones based on the transmitted signal generation would provide a productive overview of regions and environment types that may foster cellular-supported UAS navigation.

4. Existing literature points to various empirical path loss models which were formulated primarily when a scanner is held closer to the ground, with heights mimicking a human standing. However, for UAS flights at 150 ft and 400 ft, existing empirical path loss models may not be suitable. Further testing with the scanner mounted on the UAS and flying at these altitudes will enable a suitable model, which can be used for the simpler, signal strength-based range estimation and position determination.

4. SPOOF – PROOF GPS AND ADS-B SECURITY CONSIDERATIONS AND INTEGRATION OF ECD ALGORITHM TO ERAU SIMULATION ENVIRONMENT

GPS spoofing detection, mitigation, and signal recovery for GNSS / GPS using the ECD algorithm applies to both GPS and ADS-B systems. This Report focusses on GPS spoofing of ADS-B systems. Recognize that ADS-B is a mathematical subset of the larger receiver localization problem. Solutions that apply to the larger vector space, GNSS / GPS also are valid for the subset, ADS-B, if computational hardware is available. The spoofing attacks may target the ADS-B systems that incorporate GPS information within its data stream. However, since the spoofed GPS is part of the ADS-B data stream the same techniques can be used utilize to detect, mitigate, and counter spoofing attacks on the ADS-B system.

ADS-B high dependency on communication and navigation (GNSS) systems causes the system to inherit the vulnerabilities of those systems. This results in more opportunities (threats) to exploit those vulnerabilities. In general, advancements in computers, connectivity, storage, hardware, software, and apps are major aids to malicious parties who wish to conduct the spoofing and other threats by exploiting the vulnerabilities of ADS-B. Another main vulnerability of ADS-B systems is its broadcast nature without security measures, which can easily be exploited to cause harm.

Of the mitigation schemes evaluated for their effectiveness in jamming and spoofing conditions, (optical flow, geomagnetic navigation, cellular signal navigation, Wi-Fi navigation, and the ECD method), ECD ranked highest for effective mitigation of spoofing (Semke, Ranganathan, Nichols, Moncayoh, & Park, A11L.UAS.86-44 Mitigating GPS and ADS-B Risks for UAS Task 2: Identification of Potential Mitigations, August 5, 2022).

Task 1 and Task 2 showed the viability and power of ECD to do three things that other countermeasure technologies cannot do in entirety: A. Detect Spoofed communication / navigation signals in four or more false satellite transmitters; B. Using ECD to mitigate the false and true signals

(eliminating the false and exposing the true) and C. Recover the true signals in all risk conditions – especially BVLOS flights.

A functional GPS simulation model has been created by ERAU which needs to be modified to explicitly prove the ECD validity. Adjustments to certain variables and API's may need to be performed. However, the ERAU model is viable. ERAU has accomplished a great deal with its simulation approach within time and budget allotted.

4.1 Literature Research Summary

GPS / ADS-B spoofing is a professionally researched topic. Many methods have been proposed to detect, mitigate, and recover spoofed signals. Kansas State University's (KSU's) literature review of this subject was covered extensively in Section IV: GPS and ADS-B Data Signal Spoofing, pages 4-1 to 4-37 with notes in (Semke, Ranganathan, Nichols, Moncayoh, & Park, A11L.UAS.86-44 Mitigating GPS and ADS-B Risks for UAS Literature Review, September 30 2021).

The majority of the prior / current research focuses on detection of spoofing attacks. Methods of spoofing mitigation are often specialized or computational burdensome. Civilian COTS anti-spoofing countermeasures are rare. History of spoofing countermeasures has been covered in detail in (Haider & Khalid, 2016), (R.K.Nichols & et.al., 2022), and submitted KSU research reports for ASSURE 44 Task 1 and 2 (Semke, Ranganathan, Nichols, Moncayoh, & Park, A11L.UAS.86-44 Mitigating GPS and ADS-B Risks for UAS Literature Review, September 30 2021) (Semke, Ranganathan, Nichols, Moncayoh, & Park, A11L.UAS.86-44 Mitigating GPS and ADS-B Risks for UAS Task 2: Identification of Potential Mitigations, August 5, 2022).

Three tracks of research are most relevant to ECD / CD**:** Maximum Likelihood Localization, Spoofing Mitigation algorithms, and SIC. Note that historical spoofing research focusses primarily on detection of singular GPS source attacks. The focus on mitigation, correction and recovery attending to multiple spoofing signals on multiple satellite attack surface is a hallmark of ECD.

CD is a maximum likelihood GPS localization technique. It was proposed in 1996 but considered computationally infeasible at that time (Spilker, 1996). CD was first implemented by Axelrad et al. in 2011. The search space contained millions or more location hypotheses. Improvements in the computational burden were found using various heuristics (Cheong & al., 2011) (Jia, 2016). A breakthrough came with the proposal of a branch-and-bound algorithm that finds the optimal solution within ten seconds running on a single CPU thread (P. Bissag, 2017).

GPS spoofing defenses have been intensively studied. Most of them focus on detecting spoofing attacks. There is a paucity of prior research for spoofing mitigation and recovering from successful attacks by finding and authenticating the correct signals (M.L. Psiaki & Humphreys, 2016). In contrast to the vast research on GPS spoofing, there is a lack of commercial, civil receivers with anti-spoofing capabilities (Eichelberger, Robust Global Localization using GPS and Aircraft Signals, 2019). ECD inherently mitigates spoofing attacks.

Spoofing hardware performing a sophisticated seamless satellite-lock takeover attack has been built (Humphreys & al., 2008). Challenges associated with spoofing are matching the spoofed and

authentic signals amplitudes at the receiver, which might not be in line of sight and moving (Schmidt & al, 2016).

It is practically feasible for a spoofer to erase the authentic signals at a 180-degree phase offset (M.L. Psiaki & Humphreys, 2016). This is one of the strongest attacks that can only be detected with multiple receiver antennas or by a moving receiver (M.L. Psiaki & Humphreys, 2016). For signal erasure to be feasible, the spoofer needs to know the receiver location more accurately than the GPS L1 wavelength, which is 19 cm. Receivers with only a single antenna cannot withstand such an erasure attack. ECD targets single-antenna receivers and does not deal with signal erasure (Eichelberger, Robust Global Localization using GPS and Aircraft Signals, 2019). In all other types of spoofing attacks, including signal replay and multiple transmission antenna implementations, the original signals are still present and ECD remains robust (Eichelberger, Robust Global Localization using GPS and Aircraft Signals, 2019). Detecting multi-antenna receivers and differentiating signal timing consistencies is covered in (Tippenhauer & et.al, 2011).

The GPS anti-spoofing work most relevant to ECD is based on joint processing of satellite signals and the maximum likelihood localization. One method can mitigate a limited number of spoofed signals by vector tracking of all satellite signals (Jafarnia-Jahromi & al., 2012). A similar technique is shown to be robust against jamming and signal replay (Y. Ng & Gao, 2016).

ECD uses an iterative signal damping technique with spoofing signals that are similar to SIC. SIC removes the strongest received signals one by one in order to find the weaker signals and has been used with GPS signals before (G. Lopez-Risueno & Seco-Granados, 2005) (Madhani & al., 2003). That work is based on a classical receiver architecture which only keeps a signal's timing, amplitude, and phase. The ECD has its own snapshot receiver based on CD, which directly operates in the localization domain and does not identify individual signals in an intermediate stage. It is impossible to differentiate between authentic and spoofed signal, a priori, ECD does not remove signals from the sample data. Otherwise, the localization algorithm might lose the information from authentic signals/ Instead, ECD dampens strong signals by 60% in order to reveal weaker signals. This can reveal localization solutions with lower CD likelihood (Eichelberger, Robust Global Localization using GPS and Aircraft Signals, 2019).

This report highlights the brilliant additive research by Dr Manuel Eichelberger on mitigation and recovery of GPS / ADS-B spoofed signals (Eichelberger, Robust Global Localization using GPS and Aircraft Signals, 2019). ECD has been the prima facia research responsibility of the ASSURE 44 KSU team.

4.2 ECD Discussion

Collective Detection (CD) is a maximum likelihood snapshot receiver localization method, which does not determine the arrival time for each satellite, but rather combines all the available information and decide only at the end of the computation. This technique is critical to the (Eichelberger, Robust Global Localization using GPS and Aircraft Signals, 2019) (R.K.Nichols & et.al., 2022) invention to mitigate spoofing attacks on GPS or ADS-B. CD can tolerate a few low-quality satellite signals and is more robust than Coarse -Time Navigation (CTN). CD requires a lot of computational power. CD can be sped up by a branch and bound approach which reduces the computational power per location

fixed to the order of one second even for uncertainties of 100 km and a minute. CD improvements and research have been plentiful (Eichelberger, Robust Global Localization using GPS and Aircraft Signals, 2019) (J.Liu & et.al., 2012) (Axelrod & al, 2011) (P. Bissag, 2017).

Dr. Manuel Eichelberger's CD – Collective detection maximum likelihood localization approach, (ECD) method can not only detect spoofing attacks but also mitigate and recover the true signals. The ECD approach is a robust algorithm to mitigate spoofing. ECD can differentiate closer differences between the correct and spoofed locations than previously known approaches (Eichelberger, Robust Global Localization using GPS and Aircraft Signals, 2019). COTS have little spoofing integrated defenses. Military receivers use symmetrically encrypted GPS signals which are subject to a "replay" attack with a small delay to confuse receivers.

ECD solves even the toughest type of GPS spoofing attack which consists of spoofed signals with power levels similar to the authentic signals (Eichelberger, Robust Global Localization using GPS and Aircraft Signals, 2019). ECD achieves median errors under 19 m on the TEXBAT dataset, which is the de facto reference dataset for testing GPS anti-spoofing algorithms (Ranganathan & al., 2016) (Wesson, 2014). The ECD approach uses only a few milliseconds worth of raw GPS signals, so called snapshots, for each location fix. ECD does not track signals, rather it works with signal snapshots. It is suitable for snapshot receivers, which are a new class of low-power GPS receiver (M.Eichelberger, 2019) (J.Liu & et.al., 2012). Snapshot receivers aim at the remaining latency that results from transmission of timestamps from satellites every six seconds. Snapshot receivers can determine the ranges to the satellite modulo 1 ms, which corresponds to 300 km.

The use of snapshot receivers enables offloading the computation into the Cloud, which allows knowledge of observed attacks. Existing spoofing mitigation methods require a constant stream of GPS signals and track those signals over time. Computational load is increased because fake signals must be detected, removed, or bypassed (Eichelberger, Robust Global Localization using GPS and Aircraft Signals, 2019).

It is important to understand that both GPS (part of the GNSS family) and ADS-B systems are vulnerable to spoofing attacks on both manned and unmanned aircraft. In general, GPS vulnerabilities translate down to the more specific ADS-B subset which has vulnerabilities in its own right. This report summarizes the brilliant work of Dr Michael Eichelberger on Robust Global Localization using GPS and Aircraft Signals. He describes a functional tool known as CD to detect, mitigate and counter spoofing (and pre-jamming) attacks on all stages of GPS (Eichelberger, Robust Global Localization using GPS and Aircraft Signals, 2019).

GPS is ubiquitous and is incorporated into so many applications (aircraft, ship, car /truck navigation; train routing and control; cellular network, stock market, and power grid synchronization) that it makes a "rich" target for spoofing a receiver's perceived location or time. Wrong information in time or space can have severe consequences.

ATC is partially transitioning from radar to a scheme in which Aircraft (A/C) transmit their current location twice per second, through ADS-B messages. This system is mandated in Europe and well under way in the US from 2020. The A/C determined their own location using GPS. If a wrong

location is estimated by the on-board GPS receiver due to spoofing, wrong routing instructions will be delivered due to a wrong reported A/C location, leading to an A/C crash.

Ships depend heavily on GPS. They have few reference points to localize themselves apart from GPS. Wrong location indication can strand a ship, cause a collision, push off course into dangerous waters, ground a ship, or turn a ship into a ghost or a missile. 2017 incidents in the Black Sea and South China Seas have been documented (Burgess, 2017) (Nichols R. K.-P., 2019).

While planes and ships suffer spoofing attacks in the domain of location, an attacker may also try to change the perceived time of a GPS receiver. Cellular networks rely on accurate time synchronization for exchanging communication data packets between ground antennas and mobile handsets in the same network cell. Also, all neighboring cells of the network need to be time synchronized for seamless call handoffs of handsets switching cells and coordinating data transmissions in overlapping coverage areas. Since most cellular ground stations get their timing information from GPS, a signal spoofing attacker could decouple cells from the common network time. Overlapping cells might send data at the same time and frequencies, leading to message collisions and losses (Anonymous, 2014). Failing communications networks can disrupt emergency services and businesses (Eichelberger, Robust Global Localization using GPS and Aircraft Signals, 2019).

Threats and weaknesses show that large damages (even fatal or catastrophic) can be caused by transmitting forged GPS signals. False signal generators may cost only a few hundred dollars of software and hardware. Spoofing of location fixes for critical stakeholders can mean Complete Failure Of Mission.

A GPS receiver computing its location wrongly or even failing to estimate any location at all can have different causes. Wrong localization solutions come from 1) a low SNR of the signal (examples: inside a building or below trees in a canyon); 2) reflected signals in multipath scenarios, or 3) deliberately spoofed signals. (Eichelberger, Robust Global Localization using GPS and Aircraft Signals, 2019) discusses mitigating low SNR and multipath reflected signals. Signal spoofing (#3) is the most difficult case since the attacker can freely choose the signal power and delays for each satellite individually (Eichelberger, Robust Global Localization using GPS and Aircraft Signals, 2019).

The GPS system consists of a control segment, space segment and user segment. The space segment contains 24 orbiting satellites. The network monitor stations, and GCS and their antennas make up the control segment. The third and most important are the receivers which make up the user segment (USGPO, 2021).

Satellites transmit signals in different frequency bands. These include the L1 and L2 frequency bands at 1.57542 GHz and 1.2276 GHz (DoD, 2008). Signals from different satellites may be distinguished and extracted from background noise using code division multiple access protocol (DoD, 2008). Each satellite has a unique Coarse / Acquisition code (C/A) of 1023 bits. The C/A codes are Pseudo-Random Noise (PRN) sequences transmitted at 10.23 MHz which means it repeats every millisecond. The C/A code is merged using an XOR before being with the L1 or L2 carrier. The data broadcast has a timestamp called HOW which is used to compute the location of the satellite when the packet was transmitted. The receiver needs accurate orbital information (aka ephemeris) about the satellite

which changes over time. The timestamp is broadcast every six seconds, the ephemeris data can only be received if the receiver can decode at least 30 seconds of signal. (Eichelberger, Robust Global Localization using GPS and Aircraft Signals, 2019).
Civilian / Industry Stakeholders have access to the weaker signals:

- L1 and soon L1C
- L5 not widely available, but will provide enhanced capability for aviation safety
- Authorized DoD / Government Users
- More robust capability to use P(Y) and M codes on L2 in a jamming/spoofing environment.
- L2C will provide enhanced capability when operational
- Takeaways: That weaker C/A codes on L1 are the most susceptible to attacks since there are no built-in countermeasures on the GPS constellation for regular civilian users worldwide
- Critical redundancy for UAS w/o human pilot to react or onboard INS to back-up / augment their GPS due to size. Ex: sUAS, ATACMS, cruise missiles (Nichols R. , COT 684 Fusion Report Self-healing GPS Navigation Signals that have been Jammed, Spoofed or otherwise Degraded, 2023)

Classical GPS receivers use three stages when obtaining a location fix. They are Acquisition, Tracking, and Localization.

Acquisition. The relative speed between satellite and receiver introduces a significant Doppler shift to the carrier frequency. GPS receiver locates the set of available satellites. This is achieved by correlating the received signal with the known C/A codes from satellites. Since satellites move at considerable speeds (Eichelberger, Robust Global Localization using GPS and Aircraft Signals, 2019).

Tracking. After a set of satellites has been acquired, the data contained in the broadcast signal is decoded. Doppler shifts and C/A code phase are tracked using tracking loops. After the receiver obtains the ephemeris data and HOW timestamps from at least four satellites, it can start to compute its location (Eichelberger, Robust Global Localization using GPS and Aircraft Signals, 2019).

Localization. Localization in GPS is achieved using signal Time of Flight (ToF) measurements. ToFs are the difference between the arrival times of the HOW timestamps decoded in the tracking stage of the receiver and those signal transmission timestamps themselves. The local time at the receiver is unknown and the localization is done using pseudo-ranges. The receiver location is usually found using least-squares optimization (Eichelberger, Robust Global Localization using GPS and Aircraft Signals, 2019) (Wikipedia, 2021).

A main disadvantage of GPS is the low bit rate of the navigation data encoded in the signals transmitted by the satellites. The minimal data necessary to compute a location fix, which includes the ephemerides of the satellites, repeats only every 30 seconds.

Assisted GPS (A-GPS) drastically reduces the start-up time by fetching the navigation data over the Internet, commonly by connecting via a cellular network. Data transmission over cellular networks is faster than decoding the GPS signals and normally only takes a few seconds. The ephemeris data is valid for 30 minutes. Using that data, the acquisition time can be reduced since the available

satellites can be estimated along with their expected Doppler shifts. With A-GPS, the receiver still needs to extract the HOW timestamps from the signal. However, these timestamps are transmitted every six seconds, which translates to how much time it takes the A-GPS receiver to compute a location fix (Eichelberger, Robust Global Localization using GPS and Aircraft Signals, 2019).

CTN is an A-GPS technique which drops the requirement to decode the HOW timestamps from the GPS signals (Diggelen, 2009). The only information used from the GPS signals are the phases of the C/A code sequences which are detected by a matched filter. Those C/A code arrival times are related to the sub-milliseconds unambiguously, the deviation may be no more than 150 km from the correct values. Since the PRN sequences repeat every millisecond, without considering navigation data flips in the signal, CTN can in theory compute a location from one millisecond of the sampled signal. Noise can be an issue with such short signal recordings because it cannot be filtered out the same way with longer recordings of several seconds. The big advantage is that signal processing is fast and power- efficient and reduces the latency of the first fix. Since no metadata is extracted from the GPS signal, CTN can often compute a location even in the presence of noise or attenuation (Diggelen, 2009).

4.3 Spoofing and Jamming Techniques

According to (Haider & Khalid, 2016), there are three common GPS Spoofing techniques with different sophistication levels. They are simplistic, intermediate, and sophisticated (Humphreys & al., 2008).

The simplistic spoofing attack is the most used technique to spoof GPS receivers. It only requires a COTS GPS signal simulator, amplifier, and antenna to broadcast signals towards the GPS receiver. It was performed successfully by Los Alamos National Laboratory in 2002 (Warner & Johnson, 2002). Simplistic spoofing attacks can be expensive as the GPS simulator can run $400K and heavy (not mobile). Simulator signals are not synchronized by the available GPS signal and detection is easy.

In the intermediate spoofing attack, the spoofing component consists of GPS receiver to receiver genuine GPS signal and spoofing device to transmit a fake GPS signal. The idea is to estimate the target receiver antenna position and velocity and then broadcast a fake signal relative to the genuine GPS signal. This type of spoofing attack is difficult to detect and can be partially prevented by use of an IMU (Humphreys & al., 2008).

In sophisticated spoofing attacks, multiple receiver-spoofer devices target the GPS receiver from different angles and directions. The angle-of-attack defense against GPS spoofing in which the angle of reception is monitored to detect spoofing fails in this scenario. The only known defense successful against such an attack is cryptographic authentication (Humphreys & al., 2008).

Note that prior research on spoofing was to exclude the fake signals and focus on a single satellite. ECD includes the fake signal on a minimum of four satellites, and then progressively / selectively eliminates their effect until the real weaker GPS signals become apparent (Eichelberger, Robust Global Localization using GPS and Aircraft Signals, 2019).

The easiest way to prevent a receiver from finding a GPS location is jamming the GPS frequency band. GPS signals are weak and require sophisticated processing to be found. Satellite signal jamming worsens the SNR of the satellite signal acquisition results. ECD algorithms achieve a better SNR than classical receivers and can tolerate more noise or stronger jamming (Eichelberger, Robust Global Localization using GPS and Aircraft Signals, 2019).

A jammed receiver is less likely to detect spoofing since the original signals cannot be accurately determined. The receiver tries to acquire any satellite signals it can find. The attacker only needs to send a set of valid GPS satellite signals stronger than the noise floor, without any synchronization with the authentic signals (Eichelberger, Robust Global Localization using GPS and Aircraft Signals, 2019).

There is a more powerful and subtle attack on top of the jammed signal. The spoofer can send a set of satellite signals with adjusted power levels and synchronized to the authentic signals to successfully spoof the receiver (Eichelberger, Robust Global Localization using GPS and Aircraft Signals, 2019). So even if the receiver has countermeasures to differentiate the jamming, the spoofer signals will be accepted as authentic (Nichols R. K., 2020).

Two of the most powerful GPS signal spoofing attacks are: Seamless Satellite-Lock Takeover (SSLT) and Navigation Data Modification (NDM). The most powerful attack is a seamless satellite-lock takeover. In such an attack, the original and counterfeit signals are identical with respect to the satellite code, navigation data, code phase, transmission frequency and received power. This requires the attacker to know the location of the spoofed device precisely, so that ToF and power losses over a distance can be factored in. After matching the spoofed signals with the authentic ones, the spoofer can send its own signals with a small power advantage to trick the receiver into tracking those instead of the authentic signals. A classical receiver without spoofing countermeasures, like tracking multiple peaks, is unable to mitigate or detect the SSLT attack, and there is no indication of interruption of the receiver's signal tracking (Eichelberger, Robust Global Localization using GPS and Aircraft Signals, 2019).

An attacker has two attack vectors: modifying the signals code phase or altering the navigation data. The former changes the signal arrival time measurements. The latter affects the perceived satellite locations. Both influence the calculated receiver location. ECD works with snapshot GPS receivers and are not vulnerable to NDM changes as they fetch information from other sources like the Internet. ECD deals with modified, wireless GPS signals.

4.4 ECD Algorithm Design

ECD is aimed at single-antenna receivers. Its spoofing mitigation algorithm object is to identify all localization solutions. It is based on CD because 1) CD has improved noise tolerance compared to classical receivers, 2) CD is suitable for snapshot receivers, 3) CD is not susceptible to navigation data modifications, and 4) CD computes a location likelihood distribution which can reveal all likely receiver locations including the actual location, independent of the number of spoofed and multipath signals. ECD avoids all the spoofing pitfalls and signal selection problems by joining and transforming all signals into a location likelihood distribution. Therefore, it defeats the top two GPS

spoofing signal attacks (Eichelberger, Robust Global Localization using GPS and Aircraft Signals, 2019).

Relating to the 4th point, spoofing and multi-path signals are similar from a receiver's perspective. Both result in several observed signals from the same satellite. The difference is that multipath signals have a delay dependent on the environment while spoofing signals can be crafted to yield consistent localization solution at the receiver. To detect spoofing and multipath signals, classical receivers can be modified to track an arbitrary number of signals per satellite, instead of only one (S.A.Shaukat & al., 2016). In such a receiver, the set of authentic signals – one signal from each satellite – would have to be correctly identified. Any selection of signals can be checked for consistency by verification that the resulting residual error of the localization algorithm is exceedingly small. This is a combinatorically difficult problem. For *n* satellites and *m* transmitted sets of spoofed signals, there are $(m+1)^n$ possibilities for the receiver to select a set of signals. Only $m + 1$ of those will result in a consistent localization solution, which represents the actual location and *m* spoofed locations. ECD avoids this signal selection problem by joining and transforming all signals into a location likelihood distribution (Eichelberger, Robust Global Localization using GPS and Aircraft Signals, 2019).

ECD only shows consistent signals, since just a few signals overlapping (synced) for some location hypotheses do not accumulate a significant likelihood. All plausible receiver locations – given the observed signals - have a high likelihood. Finding these locations in four dimensions, space, and time, is computationally expensive (Bissig & Wattenhoffer, 2017).

To reduce the computational load comparing to exhaustively enumerating all the location hypotheses in the search space, a fast CD leveraging branch and bound algorithm is employed. (Eichelberger, Robust Global Localization using GPS and Aircraft Signals, 2019) describes the modifications to the B&B algorithm for ECD in copious detail in chapter 6. Eichelberger also discusses acquisition, receiver implementation, and experiments using the TEXBAT database. One of the key points under the receiver implementation concerns correlation of C/A codes.

The highest correlation is theoretically achieved when the C/A code in the received signal is aligned with the reference C/A code. Due to the pseudo-random nature of the C/A codes, a shift larger than one code chip from the correct location results in a low correlation value. Since one code chip has a duration of 1/1023 ms, the width of the peaks found in the acquisition vector is less than 2% of the total vector size. ECD reduces the maximum peak by 60% in each vector. A detection for partially overlapping peaks prevents changes to those peaks. Reducing the signal rather than eliminating it has little negative impact on accuracy. Before using these vectors in the next iteration of the algorithm, the acquisition result vectors are normalized again. This reduces the search space based on the prior iteration (Eichelberger, Robust Global Localization using GPS and Aircraft Signals, 2019).

4.5 ECD and ADS-B capabilities

ADS-B ubiquitously uses GPS location and signal receiver technologies. ADS-B has an extremely high dependency on communication and navigation (GNSS) systems. This is a fundamental cause of insecurity in the ADS-B system. It inherits the vulnerabilities of those systems and results in increased Risk and additional threats (Nichols R. K., 2020) (Nichols R. K.-P., 2019). Another vulnerability of the ADS-B system is its broadcast nature without security measures. These can easily

be exploited to cause other threats such as eavesdropping aircraft movement with the intention to harm, message deletion, and modification. The system's dependency on the on-board transponder is also considered a major vulnerability, which is shared by the SSR. This vulnerability can be exploited by aircraft hijackers to make the aircraft movements invisible (Busyairah, 2019).

ICAO has stressed including provisions for the protection of critical information and communication technology systems against cyberattacks and interference as stated in the Aviation Security Manual Document 8973/8 (ICAO, 2021). This was further emphasized in ATM Security Manual Document 9985 AN/492 to protect ATMs against cyberattacks (ICAO, 2021). There is a current IEEE 4-PAR standard in the works (proposed 25 April 2023 by SC 5 on Self-Healing systems) entitled: "Title: Standard for Self-healing GPS Navigation Signals that have been Jammed, Spoofed or otherwise Degraded."

Strohmeier, et al. (Strohmeier, 2015) and Nichols, et al. (Nichols R. K.-P., 2019) have both outlined a set of security requirements for piloted aircraft and unmanned aircraft, respectively. Here are the combined security requirements for the ADS-B system coordinated with the standard information security paradigm of CIA:

- Data integrity - The system security should be able to ensure that ADS-B data received by the ground station or other A/C or UAS (if equipped) are the exact message transmitted by the A/C. It should also be able to detect any malicious modification to the data during the broadcast.
- Source integrity - The system security should be able to verify that the ADS-B message received is sent by the actual owner (correct A/C) of the message.
- Data origin (location / position fix) authentication - The system security should be able to verify that the positioning information in the ADS-B message received is the original position of the A/C at the time of transmission.
- Low impact on current operations - The system security hardware / software should be compatible with the current ADS-B installation and standards.
- Sufficiently quick and correct detection of incidents
- Secure against DoS attacks against computing power
- System security functions need to be scalable irrespective of traffic density.
- Robustness to packet loss

Vulnerability in this section refers to the Ryan Nichols equations for information Risk determination. A vulnerability is a weakness in the system that makes it susceptible to exploitation via a threat or various types of threats (Nichols R. K.-P., 2019). ADS-B system is vulnerable to security threats. The Risk Assessment is covered in CHAPTER 3: SPACE ELECTRONIC WARFARE, SIGNAL INTERCEPTION, ISR, JAMMING, SPOOFING, & ECD (NICHOLS & MAI) of (R.K.Nichols & et.al., 2022). It is also discussed briefly in *CHAPTER 10: SPACE ELECTRONIC WARFARE* (NICHOLS) an upcoming textbook accepted for publication September 2023 (Nichols & Carter, CHAPTER 10: SPACE ELECTRONIC WARFARE (NICHOLS), 2023).

ADS-B principle of operation, system components, integration and operational environment are adequately discussed in Chapter 4 of (Busyairah, 2019). The ADS-B system broadcasts ADS-B messages containing A/C state vector information and identity information via RF communication links such as 1090 Extended Squitter Data Link (1090ES), UAT, or VDL Mode 4. The broadcast nature of the wireless networks without additional security measures is the main vulnerability in the system. (R.K. Nichols & Lekkas, 2002) Neither ADS-B messages are encrypted by the sender at the point of origin, nor the transmission links. There are no authentication mechanisms based on robust cryptographic security protocols. The ICAO (Airport's authority of India 2014) has verified that there is no cryptographic mechanism implemented in the ADS-B protocol (Airports Authority of India, 2014).

All-purpose Structured EUROCONTROL Surveillance Information eXchange (ASTERIX) is a binary format for information exchange in aviation. (EUROCONTROL, 2016) ADS-B data is encoded into ASTERIX CAT 21 format and transmitted by ADS-B equipped A/C to ADS-B ground stations. And decoded into usable form for ATC use. The ASTERIX format decoding guidance, source code and tools are widely available in the public domain (Busyairah, 2019).

ADS-B encoding, and broadcast are performed by either the transponder (for 1090ES) or an emitter (for UAT/ VDL Mode 4) on board the A/C. Therefore, the ADS-B aircraft surveillance is dependent on the on-board equipment. There is a vulnerability (not cyber or spoofing) whereby the transponder or emitter can be turned off inside the cockpit. Obviously, the A/C becomes invisible and SSR and TCAS operation integrity is affected.

ADS-B is an integrated system, dependent on an on-board navigation system to obtain information about the state of the A/C as well as a communication data link to broadcast the information to ATC on the ground and other ADS-B equipped A/C. The system interacts with external elements such as humans, (controllers and pilots) and environmental factors. The integrated nature of the system increases the system's vulnerability. The vulnerabilities of the GNSS on which the system relies to obtain A/C positioning information are inherited by the system. Vulnerabilities of the communications links are also inherited by the ADS-B system (Busyairah, 2019) (Eichelberger, Robust Global Localization using GPS and Aircraft Signals, 2019) (The Royal Academy of Engineering, 2011).

The broadcast nature of ADS-B RF communication links without additional security measures (cryptographic mechanisms) enables the act of eavesdropping into the transmission. Eavesdropping can lead to serious threats such as targeting specific A/C movement information with intention to harm the A/C. This can be done with more sophisticated traffic and signal analysis using available sources such as Mode S and ASDS-B capable open-source GNU Radio modules or SDR. Eavesdropping is a violation of confidentiality and compromises system security (Busyairah, 2019).

Data-link jamming is an act of deliberate / non-deliberate blocking, jamming, or causing interference in wireless communications (R.K. Nichols & Lekkas, 2002). Deliberate jamming using a radio jammer device aims to disrupt information flow (message sending /receiving) between users within a wireless network. Jammer devices can be easily obtained as COTS devices (Strohmeier, 2015) (R.K. Nichols & Lekkas, 2002). Using the Ryan Nichols equations, the Impact is severe in aviation

due to the large coverage area (airspace) which is impossible to control. It involves safety critical data; hence the computed Risk / lethality level is high (R.K. Nichols & Lekkas, 2002) (Busyairah, 2019). The INFOSEC quality affected is availability because jamming stops the A/C or ground stations or multiple users within a specific area from communicating.

Jamming is performed on ADS-B frequencies, e.g., 1090MHz. Targeted jamming attack would disable ATS at any airport using ATC. Jamming a moving A/C is difficult but feasible (Strohmeier, 2015). ADS-B system transmitting on 1090ES is prone to unintentional signal jamming due to the use of the same frequency (Mode S 1090 MHz) by many systems such as SSR, TCAS, MLAT and ADS-B, particularly in dense space (Busyairah, 2019). Not only is ADS-B prone to jamming, so is SSR (Adamy D. , 2001).

Apart from GNSS (positioning source for ADS-B) jamming, the main jamming threats for the ADS-B system include GS Flood Denial (GSFD) and A/C Flood Denial. The GSFD blocks 1090 MHz transmissions at the ADS-B ground station. There is no difficulty in gaining proximity to a ground station. Jamming can be performed using a low-power jamming device to block ADS-B signals from A/C to the ground station. The threat does not target individual A/C. It blocks ADS-B signals from all A/C within the range of the ground station. A/C flood denial blocks signal transmission to the A/C. This threat disables the reception of ADS-B IN messages, TCAS and interrogation from WAM/MLAT and SSR. It is exceedingly difficult to gain proximity to a moving A/C. The attacker needs to use a high-powered jamming device. According to (D. McCallie, 2011) these devices are not easy to obtain. The jamming function will be ineffective as soon as the A/C moves out of the specific range of the jamming device. Better attempts can actually be made from within the A/C.

ADS-B signal spoofing attempts to deceive an ADS-B receiver by broadcasting fake ADS-B signals, structured to resemble a set of normal ADS-B signals or by re-broadcasting genuine signals captured elsewhere or at a different time. Spoofing an ADS-B system is also known as message injection because fake (ghost) A/C are introduced into the air traffic. The vulnerability of the system – having no authentication measures implemented at the system's data link layer – enables this threat. Spoofing is a hit on the security goal of Integrity. This leads to undesired operational decisions by controllers or surveillance operations in the air or on ground. The threat affects both ADS-B IN and OUT systems (Busyairah, 2019). Spoofing threats are of two basic varieties: Ground Station Target Ghost Injection / Flooding and Ground Station Target Ghost Injection / Flooding.

Ground Station Target Ghost Injection / Flooding is performed by injecting ADS-B signals from a single A/C or multiple fake (ghost) A/C into a ground station. This will cause single /multiple fake (ghost) A/C to appear on the controller's working position (radar screen). Aircraft Target Ghost Injection / Flooding is performed by injecting ADS-B signals from a single A/C or multiple fake (ghost) A/C into an airplane in flight. This will cause ghost A/C to appear on the TCAS and Cockpit Display of Traffic Information screens in the cockpit to go irrational. Making the situation worse, the fake data will also be used by airborne operations such as Airborne Collision Avoidance System (ACAS), Air Traffic Situational Awareness, In Trail Procedure, and others for aiding A/C navigation operations(Busyairah, 2019).

An A/C can be made to look like it has vanished from the ADS-B based air traffic by deleting ADS-B message broadcast from the A/C. This can be done by two methods: destructive interference and constructive interference. Destructive interference is performed by transmitting an inverse of an actual ADS-B signal to an ADS-B receiver. Constructive interference is performed by transmitting a duplicate of the ADS-B signal and adding the two signal waves (original and duplicate). The two signal waves must be of the same frequency, phase and travelling in the same direction. Both approaches will be result in discarded by the ADS-B receiver as corrupt (Busyairah, 2019).

ADS-B message modification is feasible on the physical layer during transmission via datalinks using two methods: Signal Overshadowing and Bit-flipping. Signal overshadowing is done by sending a stronger signal to the ADS-B receiver, whereby only the stronger of the two colliding signals is received. This method will replace either the whole target message or part of it. Bit flipping is an algorithmic manipulation of bits. The attacker changes bits from 1 to 0 or vice versa. This will modify the ADS-B message and is a clear violation of the security goal of Integrity (Strohmeier, 2015). This attack will disrupt ATC operations or A/C navigation.

4.6 ECD Mitigation Plan

To prove the viability and robustness of ECD**,** KSU devised an ECD mitigation plan requiring simulation only. The intention of the plan is to gather data in a scenario that is challenging but is not intended to establish future testing standards or criteria, nor is it sufficient to demonstrate the effectiveness under all threats. Flight testing was not conducted because the level of maturity of the system, funding, and competing workloads in the ASSURE44 project. The mitigation plan developed was:

1. Establish a base case scenario in an urban location.
    A. Scenario will be transporting vital organ delivery by UAS between hospitals during 4-hour max transport time to be used for patient life support. [FAILURE = COMPLETE FAILURE OF MISSION]
    B. Organ and carry case weight 5 lbs
2. Establish 3–5-mile route based on 1 satellite GPS dataset. Establish routing and performance characteristics for successful delivery run.
3. Establish Spoofing case where 2/3 satellites are sending ghost signals that change GPS received signals to show / command UAS false route.
    A. False Route change must be significant enough to cause Failure of Mission (20% deviation in heading) and measurable if real time visual display.
4. Engage ECD as countermeasure:
    A. detect / differentiate all three satellites ECD must indicate correct satellite and reject 2 false ghosts
    B. mitigate route deviation (return to correct mission route) to meet life mission time and delivery specs
    C. recover correct signals and log same
5. Collect as much supplemental data from each interaction to be used to perturb parameters and/or verify ECD perform to 4A-C above.

It is understood that datasets will be batch runs. The ERAU team created the required signals and case datasets to send to Manuel to be run in his ECD models. Manuel sent results to the ERAU team for additional simulations and verification that ECD solved the 4A-C goals. In addition to proof of concept, data was collected to estimate in flight, real-time use of ECD effectiveness in further studies (Semke, Ranganathan, Nichols, Moncayoh, & Park, A11L.UAS.86-44 Mitigating GPS and ADS-B Risks for UAS Task 4: Test Plan and Report, June 2023).

The integration of the ECD Algorithm to the ERAU Simulation Environment has been a collaborative effort (H. Moncayo, Yanke, C., Yuetong, Li., 2020). The ECD algorithm requires I/Q (in-phase/quadrature) GPS signals. ERAU simulation environment did not have the capability to emulate the GPS waveform. Therefore, to accomplish integration of ECD into the ESE, a MATLAB code was written to achieve the goal of generating the GPS waveform data in the form of I/Q signals. This data resembles the received signal from an actual GPS satellite. The data produced by this code is an accordance with IS-GPS-200L (Space and Missile Systems Center (SMC) Navstar GPS Joint Program Office, 7 March 2006). The following provides a general description of the different components of the process of generating the I/Q data as shown in Figure 42.

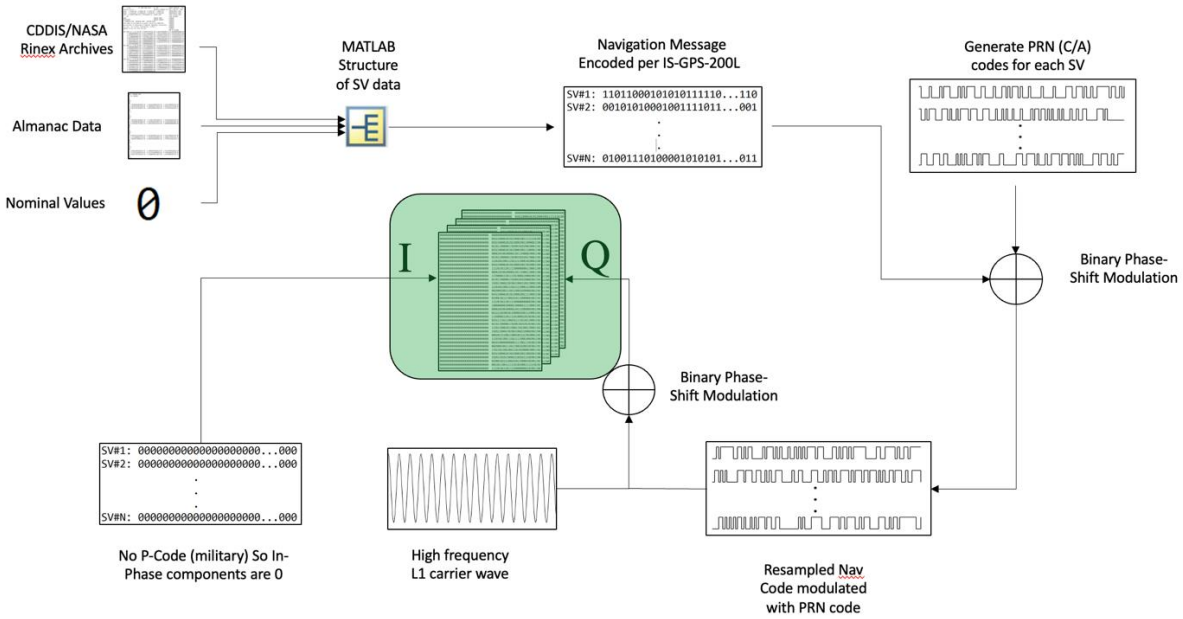

Figure 42. Process of generating I/Q data for a GPS receiver.

In practice, the data sent in the GPS signals is either computed onboard the GPS Space Vehicle (SV) or transmitted to the SV by means of a GPS ground station. For simulation purposes, this data needs to be known before creating the signal and thus must come from an existing real GPS reception. Most of the data in the navigation message is ephemeris, almanac, clock, and health data along with correction coefficients regarding the ionosphere and clock data. Ephemeris data contains information

regarding the SV's orbital parameters. This information was obtained from two sources. The almanac data was downloaded from the CelesTrak website (celestrak.org, 2023), and the ephemeris and correction data were downloaded from NASA's CDDIS website (cddis.nasa.gov, 2023). This data comes in the form of Receiver Independent Exchange (RINEX) format files. The MATLAB code reads both files and stores pertinent data in a data structure for all relevant SVs. The SV produces binary navigation data onboard with a frequency of 50 Hz. This encoded navigation data is a series of 1s and 0s and contains various information regarding satellite ephemeris data, signal health data, correction data, etc. The data is in the Legacy Navigation (LNAV) format. Then, in accordance with section 20.3 in IS-GPS-200L (IS-GPS-200G, 2013), the navigation message is then created as 37500 bits long and takes 12.5 minutes to transmit. Figure 43 illustrates an example of the code plotting the localization of the GPS Satellites and the receiver using RINEX format files.

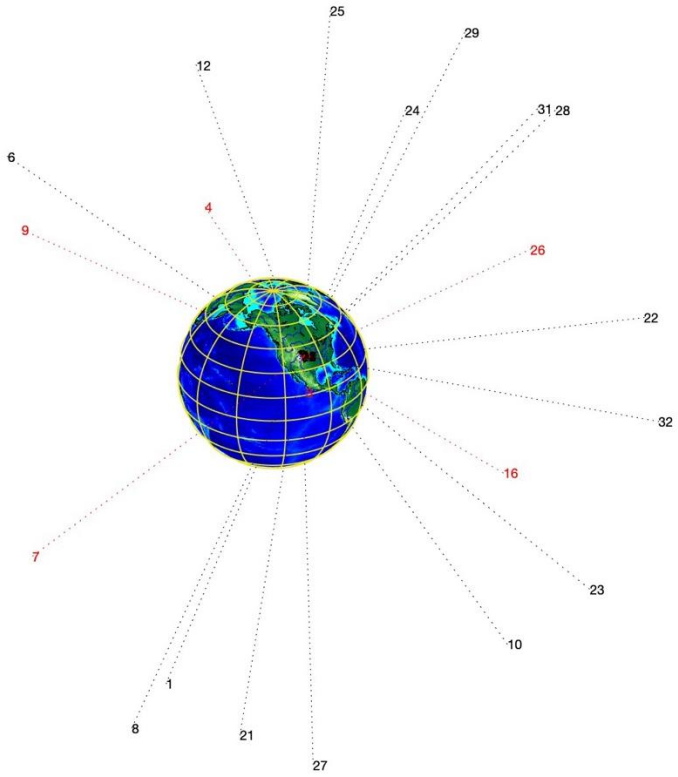

Figure 43. Example of plotting GPS Satellites and Receiver Localizations.

The GPS data typically contains a train of Binary Phase Shift Key (BPSK) modulated in binary bits and further modulated to a 1575.42 MHz carrier wave. The I/Q signals refer to two sinusoidal signals that are 90 degrees apart in phase (i.e., sine and cosine). In order for the receiver to identify which SV signal is being received, the navigation data is modulated with two types of PRN codes. The PRN codes are created using 10 and 12 stage shift registers. The BPSK modulation is performed with MATLAB bitxor() command. These codes are a higher frequency bit train produced by the SV

themselves and each SV has its own unique PRN code. The two types of codes are coarse acquisition C/A and Precise (P) as illustrated in Figure 44. The C/A code has a total length of 1023 bits and is sent with a frequency of 1.023 MHz The P code has a total length of 228.922848 terabits and is sent with a frequency of 10.23 MHz After the navigation message is modulated with either of the two PRN codes, it is then modulated onto the L1 carrier wave. The signal that gets the P code modulated data is called the in-phase and the signal that gets the C/A code modulated data is called the quadrature. If multiple signals are being created, then the signals are summed together to represent a single signal reception from a receiver. After the two modulations with the PRN codes are performed, the L1 carrier wave is modulated with these binary data trains for creating the I and Q data. The data is finally written to a binary file due to the large size of the resulting data files. Figure 43 illustrates the process of generating I/Q binary data from C/A Code and P Code using the available LNAV data. Figure 44 shows an example of the code output generating a signal representation of the Q data associated to a frequency and phase characteristics of the GPS information obtained by the receiver.

It is important to notice that the Q data signal, as illustrated in Figure 45, is prone to spoofing attacks that in consequence would change the actual estimation of the localization provided by the receiver. This attack can be simulated by adding a new signal to the Q date which would result in a change of phase and frequency properties of the localization signal.

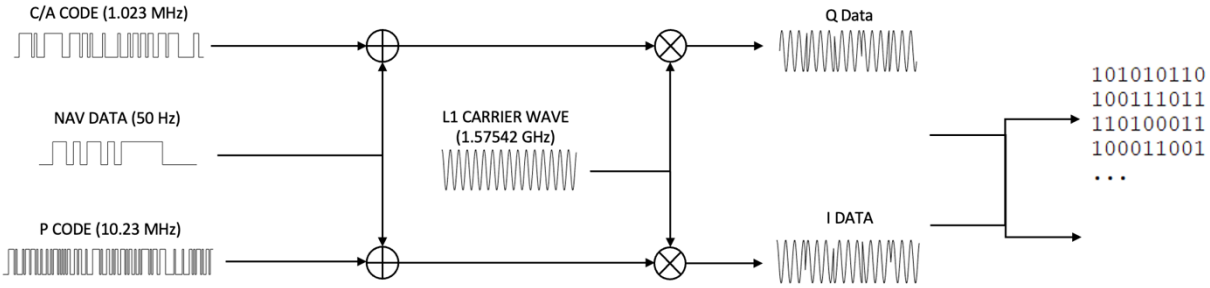

Figure 44. Illustration of the Generation of I/Q binary data using C/A and P codes.

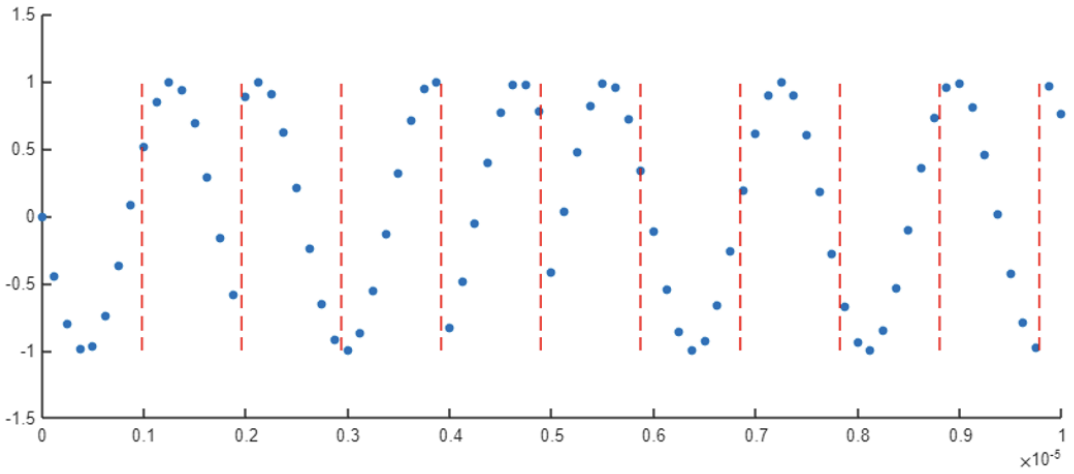

Figure 45. First 10 microseconds of Q data. Red lines are C/A chip width.

The research teams have performed in an exemplary way to prove the value of ECD value as a GNSS / GPS / ADS-B Spoofing and pre-jamming countermeasure for attacks against navigation communication signals. In 2022, because of the difficult nature of the data development (3 dimensions, time, ephemeris, satellite, and ground station considerations) and building a model for simulation ab initio, it was decided to not spend funds or time on flight testing. They chose a difficult case to solve assuming a complete simulation model could be achieved in the schedule and funds allotted. Theoretically and from published data the case was provable (Eichelberger, Robust Global Localization using GPS and Aircraft Signals, 2019) (R.K.Nichols & et.al., 2022).

However, imposing batch runs and delayed communications eventually took its toll on the teams. There were many communications between principals. The problems identified seems to be the APIs were not fully compatible, IQ samples and the simulation omits some phenomena. Both teams were working frantically to prove the technology, and both left with a positive frustration that ECD was in fact a sustainable and effective countermeasure.

4.7 ECD Results and Recommendations

The summary of the results obtained in the ECD research are:

1. For Task 4, the research and simulation activities were closed out of necessity and schedule of principals. KSU-ERAU jointly have not lost faith or interest in the ECD counter-spoofing technology.
2. Task 1 and Task 2 showed the viability and power of ECD to do three things that other countermeasure technologies cannot do in entirety: A. Detect Spoofed communication / navigation signals in four or more false satellite transmitters; B. Using ECD to mitigate the false and true signals (eliminating the false and exposing the true); and C. recover the true signals in all risk conditions – especially BVLOS flight.
3. A functional GPS simulation model has been created by ERAU which needs to be modified to explicitly prove the ECD validity. Adjustments to certain variables and API's may need to be performed. However, the ERAU model is viable. ERAU has accomplished a great deal with its simulation approach.
4. KSU-ERAU both agree that the researchers are on the verge of a huge success in terms of ECD as a countermeasure to reduce the potentially high-risk or catastrophic effects of Spoofing and pre-jamming of GNSS/GPS/ADS-B navigation signals in air, land, and sea scenarios. This is true for both commercial and military operations.

The researchers jointly recommend:

1. Continuation and completion to success of the ERAU ECD simulation efforts,
2. Funding via ASSURE sources,
3. Flight testing (perhaps along the lines of the recent NIST 3.3 Cyber Challenge which addressed Spoofing and demonstrated it on sUAS/ UAS or via Task force partner facilities, and
4. Submission of results as PAR for an FAA or NIST or IEEE standard

5. DEVELOPMENT AND IMPLEMENTATION OF OPTICAL FLOW AND GEOMAGNETIC NAVIGATION

GNSS currently represent the core of accurate and reliable positioning, navigation, and timing information for navigation systems, spanning both manned and unmanned operations. The most well-known GNSS is the GPS, accompanied by other net- works such as GLONASS, Galileo, and BeiDou. More specifically, GNSS has become crucial in localization methodologies for applications in aviation, maritime, and terrestrial domains.

Furthermore, GNSS has become increasingly vital for UAV operations due to the growing demand for precision and automation across various applications. UAVs rely heavily on GNSS signals to provide real- time, accurate positioning and navigation information, enabling them to perform tasks autonomously and efficiently. In particular, GNSS has played a crucial role in the development of advanced autopilot systems, mission planning, and geofencing capabilities, which have significantly enhanced the safety, reliability, and performance of UAVs.

In urban environments, the importance of GNSS for UAVs is further amplified. As cities continue to grow and evolve, UAVs are being increasingly deployed for a wide range of applications, such as delivery services, emergency response, infrastructure inspection, and traffic management. The

complexity of urban environments, characterized by dense buildings, infrastructure, and population, presents unique challenges for UAV navigation. Therefore, reliable operations are essential for UAVs to safely navigate the urban landscape, avoid obstacles, and maintain stable flight paths.

However, GNSS signals can be degraded due to numerous factors, including signal blockage or interference in urban environments, natural phenomena as magnetosphere interference due solar flares, and intentional jamming or spoofing attacks. The degradation of GNSS signals can lead to reduced accuracy and reliability, posing significant challenges for the safe and effective operation of UAVs, particularly in urban environments where the demand for UAV services is on the rise.

To ensure the continued safe and efficient operation of UAVs in GNSS degraded environments, it is essential to develop navigation methods and technologies that can compensate for the reduced quality of GNSS signals. GNSS Degraded Navigation focuses on the development and implementation of such methods and technologies, which enable UAVs to maintain accurate positioning and navigation capabilities even when GNSS signals are partially compromised or degraded.

These GNSS Degraded Navigation solutions often involve the integration of various sensors, algorithms, and communication technologies, which together provide a more robust and resilient navigation system. By incorporating these solutions, UAVs can continue to operate effectively in various applications, such as search and rescue missions, infrastructure inspection, surveillance, and urban air mobility, even in challenging urban environments where GNSS signal quality may be less than ideal.

The following section will present the study and development of Optical Flow integration and Geomagnetic Navigation as enhancing options for GNSS degraded environments. These techniques will be explored to enhance the reliability and accuracy of UAV navigation systems when GNSS signals are compromised. This research was supported by the integration and assessment of simulation tools due to its importance in assessing the performance and effectiveness of the proposed enhancing strategies under various conditions and scenarios. This comprehensive approach aims to provide a robust analysis for maintaining the safe and efficient operation of UAVs, even in challenging GNSS degraded urban environments.

5.1 UAV Guidance Navigation and Control Framework

This section introduces a UAV Guidance, Navigation, and Control (GN&C) framework designed to be compatible with both simulated and physical implementations. The primary objective of incorporating a simulation environment is to accurately recreate various conditions that affect the operation of a UAV, considering the environment's intrinsic characteristics and constraints aiming to cost reduction in the pre- analysis of the scenarios. Factors such as weather conditions, environmental forces, obstacles, dynamic interactions, and vehicle operation within the environment, given its GN&C systems, are considered.

The simulation design is intended to accurately represent conditions in UAV-simulated applications, facilitating the evaluation of performance, safety, and reliability of the system under examination or investigation. In subsequent sections, an in-depth understanding of the complete UAV GN&C system

will be provided by exploring its core components, which encompass the Virtual Environment, GN&C, prior the introduction to the studied enhancing strategies.

5.1.1 Virtual Environment

Gazebo was selected as the simulation environment for this project due to its robust physics engine and versatile integration with algorithm development platforms commonly used in UAV development. This software is an open-source 3D robotics simulator that offers realistic rendering of environments and objects, as well as accurate simulation of physical properties, such as gravity, friction, and aerodynamics. It allows users to create complex virtual worlds with various environmental conditions, enabling the evaluation and testing of robotic systems, including UAVs, in a controlled and safe manner.

By leveraging Gazebo's capabilities, it is possible to design and optimize UAV guidance, navigation, and control algorithms with emphasis on enhancing GNSS-based operations and test their performance under a wide range of simulated conditions. The seamless integration of Gazebo with popular development environments and frameworks, such as Robot Operating System, PX4 Autopilot, and Matlab/Simulink, further enhances its applicability for UAV development projects.

Figure 46. Virtual Environment Models.

Custom environments can be designed to meet specific mission requirements, such as building inspections, package delivery, and surveillance, among others. Figure 46 depicts the custom environment and UAV model integrated into the simulation by the ERAU team. Concurrently, a polygonal model of the area, as illustrated in Figure 47, was created to simulate shadowing and multipath effects on GNSS signals using ray-tracing collisions, thereby generating degraded conditions for subsequent assessments of the proposed enhancing strategies under the defined conditions.

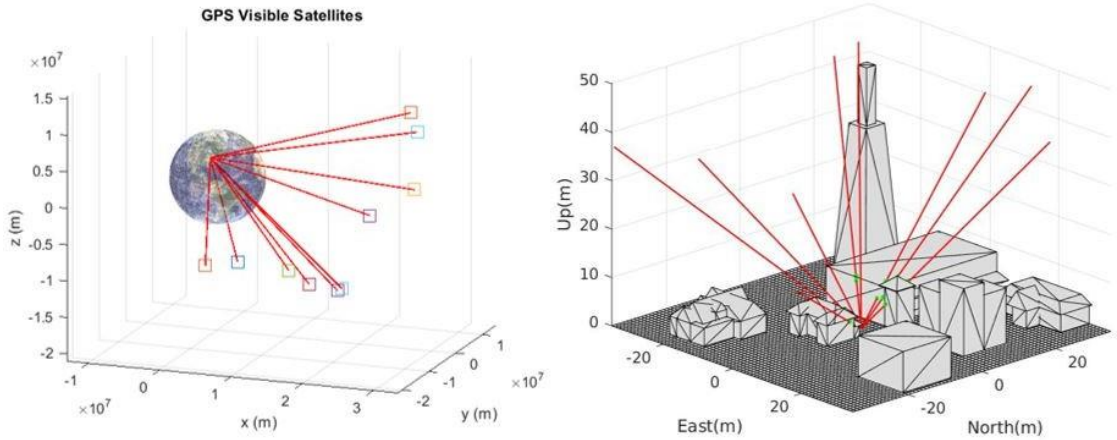

Figure 47. GNSS Signal Modeling for Shadowing Multipath Effects.

Finally, the vehicle's interaction provides the necessary information for GN&C systems. A robot operating system network is employed as the communication link between sensor plugins and MATLAB/Simulink, which runs the flight control algorithms. This seamless integration ensures accurate data exchange and real-time processing, facilitating the development and testing of GN&C systems. The subsequent subsections will delve into the details of these interconnected components as presented in

Figure 48, explaining on their roles and interplay within the virtual environment.

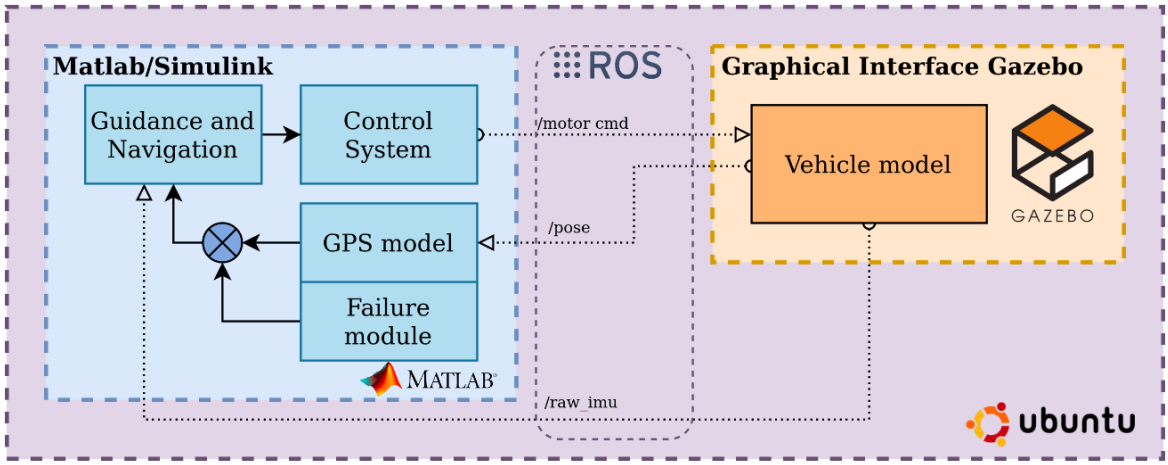

Figure 48. Simulation Architecture Baseline.

5.1.2 Guidance

The methodology employed for generating the trajectory reference for the autonomous navigation of the UAV in question is based on a set of rules that require a given set of input waypoints. The vehicle is expected to address these waypoints sequentially, ensuring a coherent and continuous path for navigation. As illustrated in Figure 49, the UAV's trajectory is determined by connecting these waypoints, which serve as reference points for the autonomous guidance system.

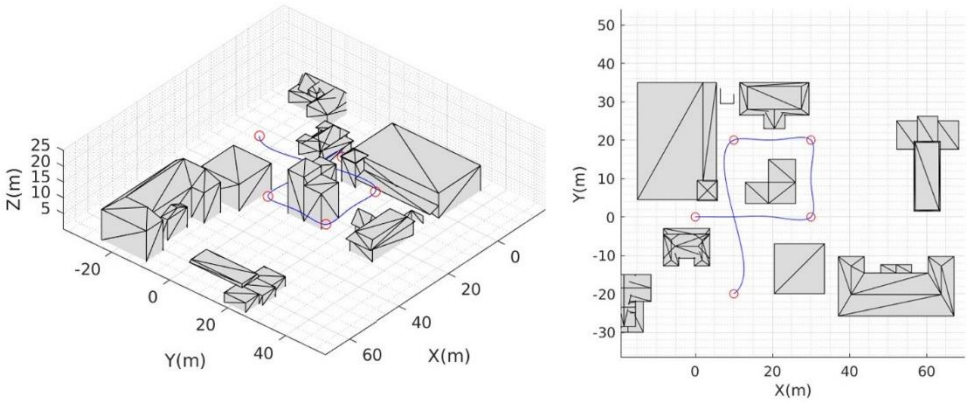

Figure 49 .UAV Reference Trajectory and Waypoints.

By following the predefined sequence of waypoints, the UAV can navigate through complex environments while adhering to mission objectives and operational constraints. This guidance methodology, as considered in this research, offers a flexible and modular approach to trajectory planning. It is well-suited for a control architecture that performs effectively under degraded GNSS conditions, thus allowing for easy adaptation and optimization based on specific mission requirements and environmental conditions.

5.1.3 Navigation System

The objective of the navigation module is to accurately determine the vehicle's position, velocity, and attitude in real-time. This information is critical for safe and efficient operation, as it enables the UAV to navigate autonomously within its operational environment and follow the desired trajectory provided by the Guidance module. The Navigation module processes data from various sensors, such as Global Navigation Satellite System receivers, IMUs, and potentially other sensors like cameras or LIDAR as it will be further discussed. By fusing and filtering this data, the Navigation module generates reliable estimates of the UAV's state, which is then utilized by the control module to generate appropriate control inputs that ensure the UAV adheres to the guidance trajectory while maintaining stability and robustness in the presence of disturbances and uncertainties.

The baseline architecture for the navigation system consists of a loosely coupled integration of INS/GNSS (Titterton and Weston 2004), using an Extended Kalman Filter (EKF) as presented in Figure 50. This approach provides robust navigation performance even in degraded GNSS conditions. The following sections will elaborate on the essential components of this navigation system, starting with the Inertial Navigation System (INS), followed by the EKF and the 15-state Pinson error model used for the state estimation of the vehicle.

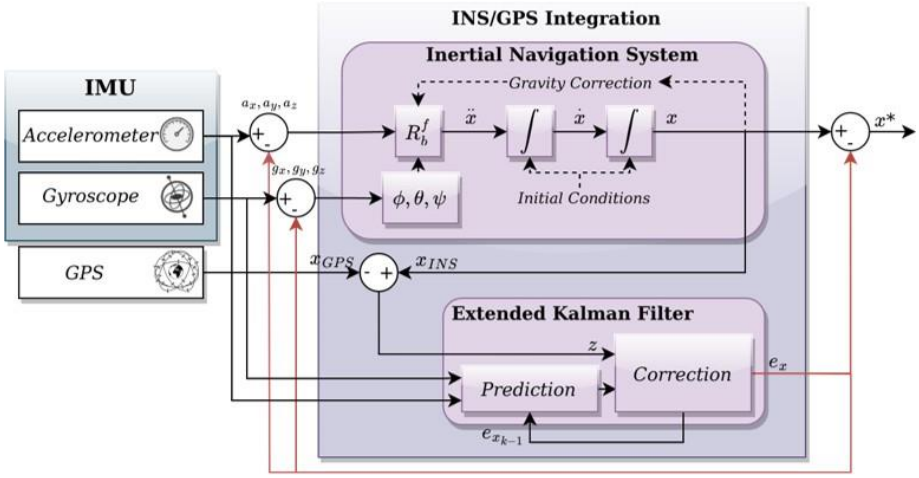

Figure 50. INS-GNSS loosely coupled integration.

The INS is a self-contained navigation technique that uses measurements pro- vided by an IMU to estimate the position, velocity, and attitude of a vehicle (Titterton and Weston 2004). The INS mechanization equations are derived from Newton's laws of motion and are implemented using the IMU's measurements of linear acceleration and angular velocity. As depicted in Figure 51, the INS comprises a set of accelerometers and gyroscopes that sense motion in three-dimensional space.

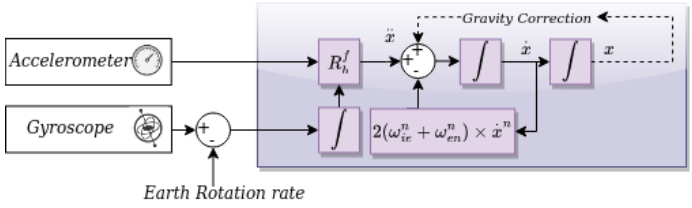

Figure 51. Inertial Mechanization.

The INS mechanization equations using a reference frame can be expressed as follows using the inertial frame mechanization:

$$\dot{V}^{\iota} = R_b^i a^b - \omega_{ie}^i \times V^i + g^i \tag{1}$$

$$\dot{P}^{\iota} = V^i \tag{2}$$

$$\dot{R}_b^{\iota} = R_b^i \times \Omega_{ib}^b \tag{3}$$

$$\Omega_{ib}^b = \begin{bmatrix} 0 & -r & q \\ r & 0 & -p \\ -q & p & 0 \end{bmatrix} \tag{4}$$

In these set of equations, $\dot{V}^{\iota}$ represents the derivative of the velocity vector in the Inertial frame. $\dot{R}_b^{\iota}$ is the rotation matrix that transforms a vector from the body frame (b) to the inertial (i), a^b denotes the specific force (linear acceleration) vector in the body frame, ω_{ib}^b refers to the vehicle rotation

vector, g^i stands for the gravity vector in the inertial frame, $\dot{P}^\iota$ signifies the derivative of the position vector in the inertial frame, $\dot{R}_b^\iota$ is the derivative of the rotation matrix that transforms a vector from the body frame to the inertial frame, Ω_{ib}^b denotes the skew-symmetric matrix representation of the angular rate vector Ω_{ib}^b in the body frame, and finally, *p, q, r* represents the roll, pitch, and yaw rates of the vehicle in the body frame, respectively. These notations and the corresponding equations describe the basic INS mechanization process, considering the specific forces and angular rates measured by the IMU in the body frame, without considering the Earth's rotation rate.

The EKF is a widely used estimation technique that recursively updates the state estimate based on noisy sensor measurements and a nonlinear system model (Corporation 1974). The EKF incorporates a linearized version of the system model and uses the following common set of equations for prediction and update steps:

Prediction:

$$\hat{x}_{k|k-1} = f\left(\hat{x}_{k-1|k-1}, u_k\right) \tag{5}$$

$$P_{k|k-1} = F_{k-1} P_{k-1|k-1} F_{k-1}^T + Q_k \tag{6}$$

Update:

$$K_k = P_{k|k-1} H_k^T \left(H_k P_{k|k-1} H_k^T + R_k\right)^{-1} \tag{7}$$

$$\hat{x}_{k|k} = \hat{x}_{k|k-1} + K_k \left(z_k - h\left(\hat{x}_{k|k-1}\right)\right) \tag{8}$$

$$P_{k|k} = (I - K_k H_k) P_{k|k-1} \tag{9}$$

Here, f and h are the nonlinear process and measurement models, respectively, and F_{k-1} and H_k are their respective Jacobians. The state estimate is denoted by $\hat{X}_k$ with the subscript denoting the time index and the vertical bar indicating the prediction and update steps. Finally, Q_k and R_k correspond to the process and measurement noise covariances respectively.

The nonlinear mathematical model used to describe the vehicle dynamics in this research effort corresponds to the 15-error Pinson model (Titterton and Weston 2004), which is a well-established error model widely used for designing and analyzing the performance of Inertial Navigation System aided by GNSS in a loosely coupled integration scheme. This model is particularly useful for capturing the error dynamics of the system, allowing designers to quantify the effects of sensor errors, initial alignment errors, and other uncertainties on the estimated navigation states. By representing the navigation errors as a 15-element error state vector as follows, the model enables the implementation of an Extended Kalman Filter to optimally fuse the information from the GNSS and INS and provide accurate navigation solutions.

$$\delta X \quad = [\delta P \ \delta V \ \delta \Theta \ \delta b_a \ \delta b_g] \tag{10}$$

This state represents the errors in the position, velocity and attitude vectors, as well as including the inertial measurement unit sensor biases from the accelerometer and gyroscope respectively. The error model equations capture the effects of sensor biases, scale factor errors, and noise on the measured specific force and angular rate, represented as follows:

$$\tilde{a}^b = a^b + R_b^i \delta b_a + \epsilon_a + g \tag{11}$$

$$\tilde{\omega}_{ib}^b = \omega_{ib}^b + \delta b_g + \epsilon_g \tag{12}$$

where a^b represents the measured specific acceleration in the body frame, a^b denotes the true specific acceleration in the body frame. Additionally, δb_a is the accelerometer bias error vector in the body frame, ϵ_a is the accelerometer noise vector in the body frame, $\tilde{\omega}_{ib}^b$ is the measured angular rate vector in the body frame, ω_{ib}^b is the true angular rate vector in the body frame, δb_g represents the gyroscope bias error vector in the body frame, and δb_g is the gyroscope noise vector in the body frame.

The description of sensor errors enables the definition of navigation error equations, as it facilitates the analysis of error components and noise influences on the equations of motion and, consequently, the propagation of the system. First, because the direction cosine matrix and the Euler angles are calculated based on gyroscope information that includes noise and bias, it is essential to model the errors in the rotation matrix and angles as follows:

$$\begin{bmatrix} \dot{\delta\phi} \\ \dot{\delta\theta} \\ \dot{\delta\psi} \end{bmatrix} = \begin{bmatrix} \delta p + \delta q S(\phi)T(\theta) + \delta r C(\phi)T(\theta) \\ \delta q C\phi - \delta r S\phi \\ \delta q S\phi Sec\theta + \delta r C\phi Sec\theta \end{bmatrix} \tag{13}$$

Here, *C* and *S* corresponds the sine and cosine, and $\delta\theta, \delta\phi, \delta\psi$ are the attitude errors in Roll pitch and Yaw. The error in the rotation matrix R_b^i can be calculated by using the found angle errors consequently. Regarding position and velocity states, the differential equations that describe the states are:

$$\begin{bmatrix} \dot{\delta P} \\ \dot{\delta V} \end{bmatrix} = \begin{bmatrix} \delta V \\ -S_f^i \delta\Theta + R_b^i \delta b_a \end{bmatrix} \tag{14}$$

Finally, the term S_f^i corresponds to the Skew matrix error in the forces rotation from the body frame to the inertial frame due to errors in the gyroscope measurements. For this case this only affects the gravity pull, so this term can be represented as follows:

$$S_f^i = \begin{bmatrix} 0 & -a_z & -a_y \\ a_z & 0 & -a_x \\ a_y & -a_x & 0 \end{bmatrix} \tag{15}$$

By assuming a small angle rotation and no Earth rotational velocity, it is possible to write the required linear representation of the given set of states for its integration in the Kalman filter as follows (Schumacher, n.d.; Gustavsson 2015):

$$\begin{bmatrix} \dot{\delta P} \\ \dot{\delta V} \\ \dot{\delta \Theta} \\ \dot{\delta b}_a \\ \dot{\delta b}_g \end{bmatrix} = \begin{bmatrix} 0_3 & I_3 & 0_3 & 0_3 & 0_3 \\ 0_3 & 0 & -S_f^i & R_b^i & 0_3 \\ 0_3 & 0_3 & 0_3 & 0_3 & R_b^i \\ 0_3 & 0_3 & 0_3 & 0_3 & 0_3 \\ 0_3 & 0_3 & 0_3 & 0_3 & 0_3 \end{bmatrix} \begin{bmatrix} \delta P \\ \delta V \\ \delta \Theta \\ \delta b_a \\ \delta b_g \end{bmatrix} + \begin{bmatrix} 0_3 & 0_3 \\ R_b^i & 0_3 \\ 0_3 & R_b^i \\ 0_3 & 0_3 \\ 0_3 & 0_3 \end{bmatrix} \begin{bmatrix} \epsilon_a \\ \epsilon_g \end{bmatrix} \quad (16)$$

5.2 Control Architecture

A control architecture is essential for a UAV to ensure stability, precision, and robustness during flight operations. The control system is responsible for managing the UAV's motion by adjusting its actuators in response to deviations from the desired trajectory or flight path. This is particularly important for maintaining accurate navigation and ensuring the safe execution of mission objectives in dynamic environments or under challenging conditions.

The controller selection was based on an analysis performed by the team (A. Cuenca and H. Moncayo 2023), as illustrated in Figure 52, and corresponds to a waypoint position control based on fuzzy velocity referencing. This design aims to enhance the UAV's ability to follow the desired trajectory by dynamically adjusting its velocity reference according to the current distance to its waypoint objective and GNSS signal conditions. By employing a fuzzy logic approach, the control system can better adapt those position measurement uncertainties, resulting in improved stability and precision during flight operations. The subsequent section will detail the various subcomponents that constitute the comprehensive control scheme.

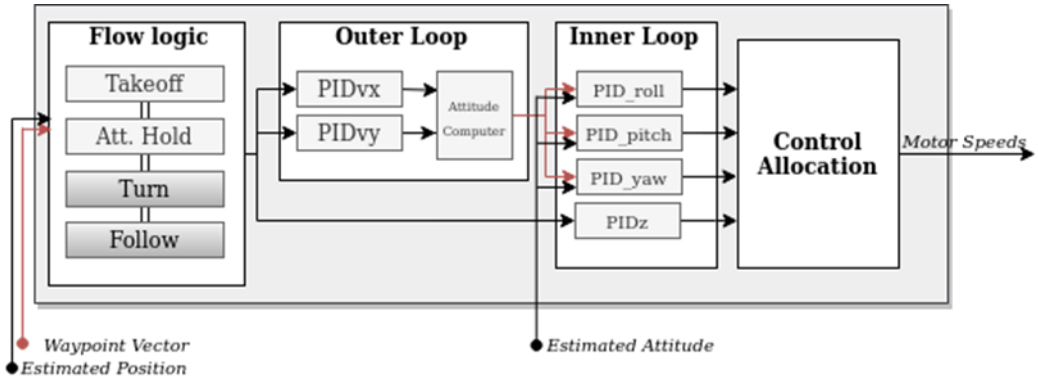

Figure 52. Position Control Scheme with Fuzzy velocity referencing.

5.2.1 Waypoint Control Flow Logic

The control architecture includes a Flow logic shown in Figure 52, in order to attack the current and next waypoint after its initialization, which involves taking off and maintaining attitude hold before acquiring the initial waypoint. Subsequently, the next coordinates are obtained, and a yaw correction

is executed to orient the vehicle towards the next objective with the appropriate yaw angle direction. The UAV will then follow the fuzzy controller commands based on its distance from the goal until its position is met within a circular boundary. This boundary is defined by evaluating the position within a circle centered at the waypoint with a given radius R. When the UAV is within this distance, it is considered to have reached the objective waypoint.

Upon meeting this criterion, the UAV will hold its altitude and attitude for a given number of seconds. After this period, the vehicle will acquire the next objective and iteratively execute the logic until all waypoints have been visited. It is important to note that this algorithm assumes no obstacles are present between two consecutive waypoints, and as such, no obstacle avoidance logic is included, unlike the ACASxu system (M. J. Kochenderfer et al. n.d.).

5.2.2 Inner Control - Attitude

Owing to the inherent instability of a UAV with a quadrotor configuration, the first challenge in achieving stable flight involves defining an attitude control that will function as the inner controller. This inner controller must assess the attitude error and produce the desired forces and moments necessary for vehicle control. Consequently, a collection of Proportional Integral Derivative (PID) controllers is defined as follows:

$$\tau_{\phi} = k_d\left(\dot{\phi}_{ref} - \dot{\phi}\right) + k_p\left(\phi_{ref} - \phi\right) + k_i \int \left(\phi_{ref} - \phi\right) \tag{17}$$

$$\tau_{\theta} = k_d\left(\dot{\theta}_{ref} - \dot{\theta}\right) + k_p\left(\theta_{ref} - \theta\right) + k_i \int \left(\theta_{ref} - \theta\right) \tag{18}$$

$$\tau_{\Psi} = k_d\left(\dot{\Psi}_{ref} - \dot{\Psi}\right) + k_p\left(\Psi_{ref} - \Psi\right) + k_i \int \left(\Psi_{ref} - \Psi\right) \tag{19}$$

$$F_z = (k_d\left(\dot{Z}_{ref} - \dot{Z}\right) + k_p\left(Z_{ref} - Z\right) + k_i \int \left(Z_{ref} - Z\right) \frac{m}{C\theta C\phi} \tag{20}$$

The relationship between the vehicle actuators' rotational speed and the moments generated by the produced thrust is employed to determine the control allocation. Assuming a quadrotor configuration with the body frame aligned with the UAV frame in a North-East-Down orientation, it is established:

$$\begin{bmatrix} \tau_{\phi} \\ \tau_{\theta} \\ \tau_{\Psi} \\ T \end{bmatrix} = \begin{bmatrix} Kl(\omega_4^2 - \omega_2^2) \\ Kl(\omega_3^2 - \omega_1^2) \\ b(\omega_4^2 - \omega_3^2 + \omega_2^2 - \omega_1^2) \\ T_1 + T_2 + T_3 + T_4 \end{bmatrix} \tag{21}$$

The inversion of these set of equations, combined with the integration of the controllers from (R. Hartley and A. Zisserman 2003), constitutes the inner control with control allocation. This process yields a solution for the required motor speeds.

5.2.3 Outer Control - Position

The control law of the outer loop is established by setting the reference velocities, which are generated by integrating fuzzy rules within the turn and follow steps. The reference angles for the inner loop are then computed using a set of PIDs with feedback from the velocity error. These PIDs are defined as follows:

$$k_{p_i}\left(\dot{r}_{i_T} - \dot{r}_i\right) + k_{p_i}\left(\dot{r}_{i_T} - \dot{r}_i\right) + k_{i_i}\int\left(\dot{r}_{i_T} - \dot{r}_i\right) = \ddot{r}_{ref} \tag{22}$$

Finally, to account for the noise in the velocity measurements, a moving average with a sliding window of ten measurements was incorporated into the PID controller ("Robust Waypoints Navigation Using Fuzzy Type 2 Controller | IEEE Conference Publication | IEEE Xplore" n.d.). The outer control layer generates attitude reference commands for the inner control layer by associating the desired accelerations over the Newton's second law, as shown in Eq. 23. Small angle approximations are used under hovering conditions.

$$\ddot{r}_c = m\begin{bmatrix}\ddot{x}_c\\ \ddot{y}_c\\ \ddot{z}\end{bmatrix} = \begin{bmatrix}0\\0\\-mg\end{bmatrix} + R\begin{bmatrix}0\\0\\T\end{bmatrix} \tag{23}$$

The relation between the desired accelerations and the roll and pitch angles is obtained as presented as (Mellinger, Michael, and Kumar 2014):

$$\ddot{x}_c = g(\theta_c cos\Psi + \phi_c sin\Psi) \tag{24}$$

$$\ddot{y}_c = g(\theta_c sin\Psi - \phi_c cos\Psi) \tag{25}$$

$$\ddot{z}_c = \frac{T}{m} + g \tag{26}$$

Solving these set of equations algebraically for the angles in terms of the accelerations provides a relation between the required angles and on the reference positions:

$$\phi_{ref} = \frac{1}{g}\left(\ddot{X}_{ref} sin\left(\psi_{ref}\right) - \ddot{Y}_{ref} cos\left(\psi_{ref}\right)\right) \tag{27}$$

$$\theta_{ref} = \frac{1}{g}\left(\ddot{X}_{ref} cos\left(\psi_{ref}\right) + \ddot{Y}_{ref} sin\left(\psi_{ref}\right)\right) \tag{28}$$

$$\psi_{ref} = \psi \tag{29}$$

Once the reference angles are defined, together, these controllers create a comprehensive and robust control system, allowing the UAV to navigate effectively and efficiently through its environment.

5.3 Enhancing Strategies

This section will target the integration of optical flow and geomagnetic positioning as enhancing strategies for the UAV's navigation system. These methods were selected from a broad range of

alternatives, including SLAM (Simultaneous Localization and Mapping), terrain navigation, LiDAR (Light Detection and Ranging), complex sensor fusion, and computer vision approaches. The chosen enhancing strategies aim to improve the performance and robustness of the UAV's navigation system, particularly in GNSS degraded environments.

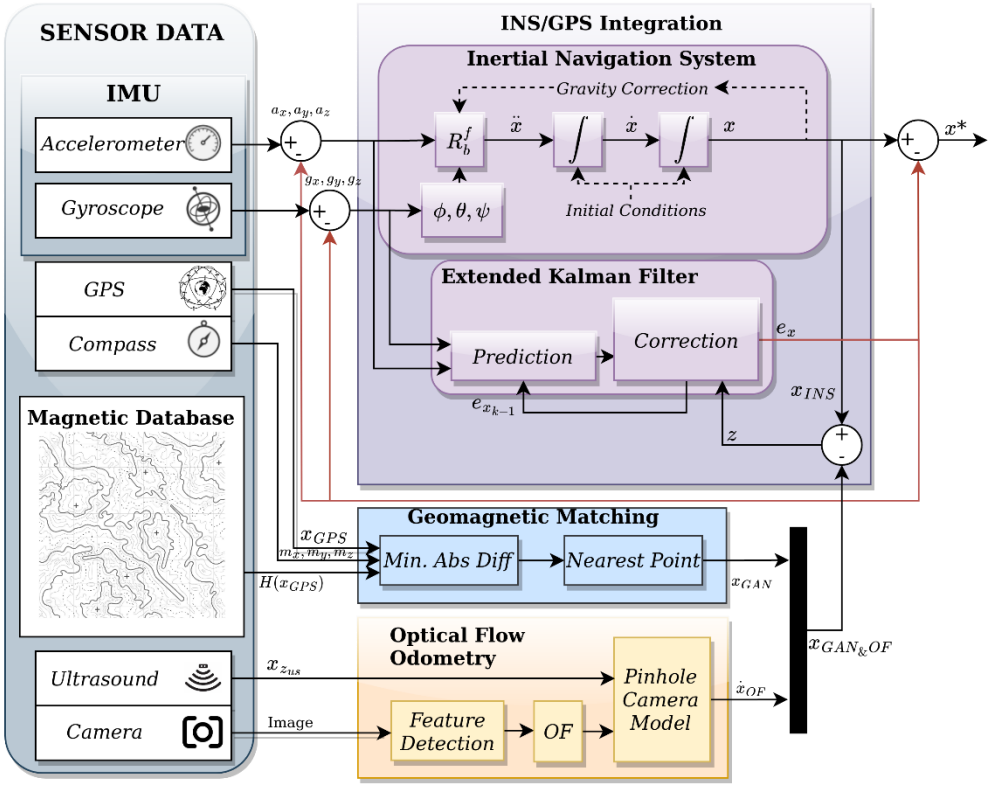

Figure 53. Enhanced INS-GNSS Loosely coupled Integration by Geomag. and Optical Flow Odometry.

The proposed general architecture illustrated in Figure 53, is defined on top of the scheme presented in Figure 50, which now incorporates both the optical flow and geomagnetic navigation as enhancing strategies. This integrated approach aims to define a robust navigation solution by combining the individual strengths of each method. The architecture seamlessly integrates the information from the optical flow and geomagnetic navigation systems with the existing guidance, navigation, and control components previously described, allowing for enhanced adaptability and resilience. A detailed examination of this integrated architecture and the benefits it provides to the UAV's navigation performance will be presented in the following subsections.

5.4 Visual Odometry with Optical Flow

Optical flow can be considered as a valuable visual odometry tool for UAV navigation, providing a means of estimating the vehicle's motion based on the observed changes in the scene's features over time. By analyzing the apparent motion of features in the captured images, optical flow algorithms can estimate the UAV's relative position and velocity, offering an alternative or complementary source of navigation information.

The optical flow algorithms essentially analyze pixel motion between two-dimensional images as a projection of the three-dimensional motion of objects relative to the visual sensor. The navigation information obtainable through optical flow fields includes rotational and translational velocities. In the following sub- sections, the sub-components of the optical flow process will be developed, including the feature detection and tracking, optical flow vector determination, and velocity estimation through camera models.

5.4.1 Feature Detection

Feature detection and tracking algorithms are necessary in optical flow for navigation as they enable the identification and monitoring of distinctive points in a sequence of images, thereby facilitating the computation of motion information from consecutive frames. These algorithms are crucial for ensuring that the optical flow process can reliably estimate the motion of objects in the environment, which ultimately aids the UAV in determining its position and orientation relative to the surroundings (Beauchemin and Barron 1995) (Song, Seneviratne, and Althoefer 2011). By accurately tracking the features over time, a more robust and consistent motion estimation can be achieved, which directly translates into improved navigation performance for the UAV (Scaramuzza and Siegwart 2008).

Various algorithms for feature detection are available, and their suitability depends on the specific requirements of different applications. Some examples of these methods include the Shi-Tomasi or good features to track (Shi and Tomasi 1994), Features from Accelerated Segment Test, Scale Invariant Feature Transform, and Speeded-up Robust Features corners (Chao, Gu, and Napolitano 2014). The Shi-Tomasi algorithm was chosen for this project due to its robustness under orientation changes and computational efficiency.

In the context of grayscale images, the Shi-Tomasi algorithm functions by calculating a corner response function for each pixel in the image. This response function relies on the eigenvalues of the image gradient matrix, which represents the rate of change of image intensity in both the x and y directions. Initially, the algorithm computes the image gradient using a filter such as the Sobel operator. Subsequently, for each pixel in the image, it forms a 2x2 matrix containing the sum of squared differences of the gradient within a small neighborhood surrounding the pixel. The eigenvalues of this matrix are then determined, with their minimum value serving as a measure of cornerness (Harris and Stephens 1988).

$$\hat{S}(x,y) = \sum_{u,v} w\,(u,v) \times \begin{bmatrix} \frac{\partial I}{\partial x}^2 & \frac{\partial I}{\partial x}\frac{\partial I}{\partial y} \\ \frac{\partial I}{\partial x}\frac{\partial I}{\partial y} & \frac{\partial I}{\partial y}^2 \end{bmatrix} \tag{30}$$

In this context, $w(u, v)$ represents a windowing function, which is sometimes equivalent to one. As a result, the trace and determinant are computed to find the value of R, which aids in determining as illustrated in the Figure 54, whether the pixel is a corner or an edge as follows:

$$R = detS - k(traceS)^2 \tag{31}$$

$$det(S) = \lambda_1 \lambda_2 \tag{32}$$

$$trace(S) = \lambda_1 + \lambda_2 \tag{33}$$

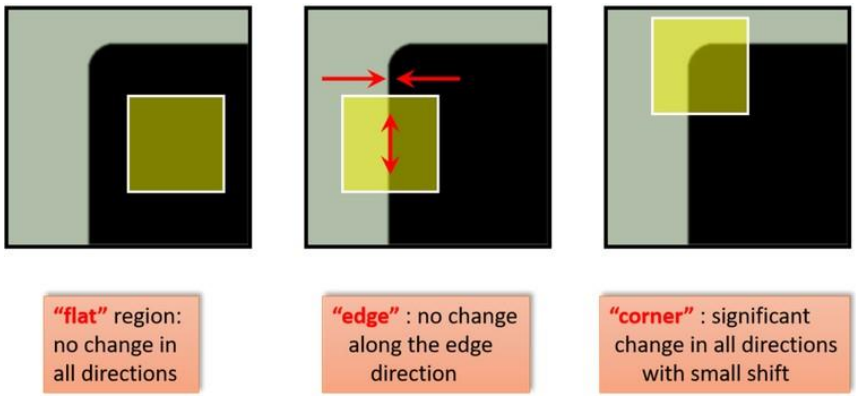

Figure 54. Illustration of Intensity use for Corner and Edge Detection (G. Bradski 2000).

Pixels with a low minimum eigenvalue are classified as edges, whereas those with a high minimum eigenvalue are considered corners. The algorithm applies a threshold to the corner response function, selecting a set of strong corners to be used as feature points for further analysis.

5.5 Optical Flow Navigation

In the context of navigation, there are two methods commonly employed for optical flow calculation, namely differential methods and region-based matching processes. In the specific context of a downward camera attached to an UAV, differential methods are the choice, such as the widely used Lucas-Kanade approach. This method calculates the velocity of features detected and tracked across two consecutive images by computing the flow from spatio-temporal derivatives of the image intensity or filtered image. It is assumed minimal changes between the images, constant brightness, and smooth spatial motion.

Considering an image denoted as $I(x, y)$, the following image derived from a small motion can be represented as $H(x, y) = I(x + u, y + v)$ where u, v represent the displacement of the pixel. The Lucas-Kanade method leads to the following optimization statement (Gageik, Strohmeier, and Montenegro 2013) :

$$\begin{bmatrix} \dot{\mu} \\ \dot{\nu} \end{bmatrix} = \begin{bmatrix} \sum_{(i,j)} I_x(i,j) * I_t(i,j) \\ \sum_{(i,j)} I_y(i,j) * I_t(i,j) \end{bmatrix} * \begin{bmatrix} \sum_{(i,j)} I_x^2(i,j) & \sum_{(i,j)} I_x(i,j) * I_y(i,j) \\ \sum_{(i,j)} I_x(i,j) * I_y(i,j) & \sum_{(i,j)} I_y^2(i,j) \end{bmatrix}^{-1} \tag{34}$$

Where $I_x(i, j)$, $I_y(i, j)$ and $I_t(i, j)$ correspond to the partial intensity derivatives of the given pixel $I(i, j)$ and μ and v represents the searched optical flow values in the two-dimensional plane.

By calculating the optical flow for each feature, it is possible to track the movement of these features across subsequent images. Furthermore, the velocity information provided by the flow is integrated with inertial measurements and camera models to translate 2-dimensional velocities into the vehicle's 3-dimensional motion.

5.5.1 Pinhole Camera Model

An ideal motion estimation based on Optical Flow can be derived by considering a camera model and the motion of objects in space. Two major approaches can be implemented for deriving motion models: the pinhole image plane and the spherical imaging surface.

The pinhole camera model is a fundamental concept in computer vision and photogrammetry, which provides a simple yet effective representation of the geometric relationship between a 3D point in the world and its 2D projection onto an image plane as illustrated in the Figure 55. This model is based on the idea that light rays from a scene pass through a single point (the pinhole) before being projected onto an image plane located behind the pinhole (R. Hartley and A. Zisserman 2003). In this model, the transformation from the 3D world coordinates to the 2D image coordinates can be described mathematically by a perspective projection, which involves a series of coordinate transformations, including rotation, translation, and scaling.

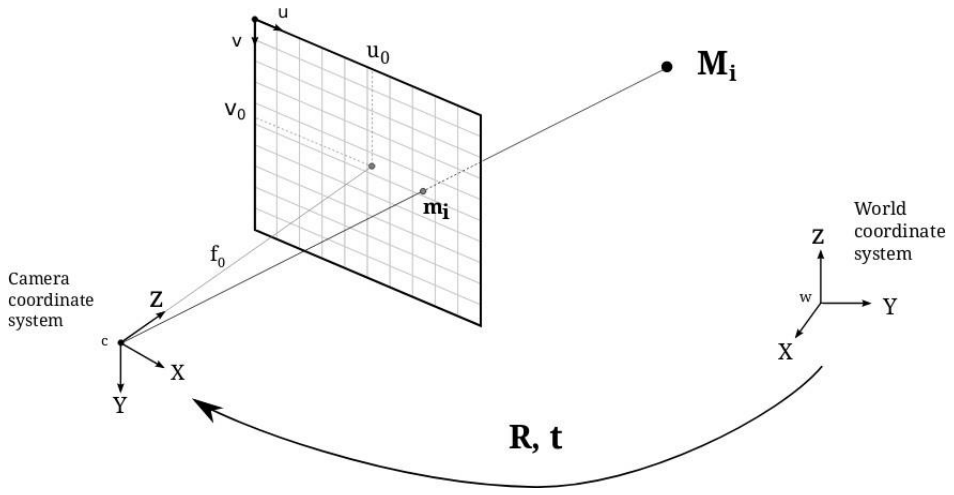

Figure 55. Pinhole Camera Model.

Within the pinhole image plane approach, a given point (η_x, η_y, η_z) in the 3D camera body frame F_c is mapped onto the 2D image plane P_i. Given a focal length f, the mapping function from the camera frame to the image plane is defined as (Chao, Gu, and Napolitano 2013):

$$m_x x_i = \mu = f\frac{\eta_x}{\eta_y} \tag{35}$$

$$m_y y_i = v = f\frac{\eta_y}{\eta_z} \tag{36}$$

The camera is situated within the coordinate frame x, y, z and has its own body frame aligned with the camera's optical axes. If the relative position of the camera within the world frame is known, an expression can be defined for the projection of the point η_x, η_y, η_z onto the image plane u, v. This is referred to as the Forward Imaging Model.

The ideal optical flow estimates can be acquired through the derivative of the previous equations as:

$$\begin{bmatrix}\dot{\mu}\\ \dot{v}\end{bmatrix} = f\begin{bmatrix}\frac{1}{\eta_z} & 0 & -\frac{\eta_x}{\eta_z^2}\\ 0 & \frac{1}{\eta_z} & -\frac{\eta_y}{\eta_z^2}\end{bmatrix}\begin{bmatrix}\dot{\eta_x}\\ \dot{\eta_y}\\ \dot{\eta_z}\end{bmatrix} \tag{37}$$

Assuming that the camera is mounted at the center of the UAV in a downward-facing position, the optical flow can be extended to incorporate the vehicle's dynamics within the mathematical expression (Chao, Gu, and Napolitano 2014) (Chao, Gu, and Napolitano 2013):

$$\begin{bmatrix}\dot{\mu}\\ \dot{v}\end{bmatrix} = f\begin{bmatrix}\frac{1}{\eta_z} & 0 & -\frac{\eta_x}{\eta_z^2}\\ 0 & \frac{1}{\eta_z} & -\frac{\eta_y}{\eta_z^2}\end{bmatrix}\left[C_{V_{\frac{B}{C}}} + C_{\omega_{\frac{B}{C}}} \times \left(C_P - C_{O_B}\right)\right] \tag{38}$$

In this expression, $C_{V_{B/C}}$ represents the linear ground velocity components *u, v, w*, the term $C_{\omega_{B/C}}$ accounts for the angular velocities *p, q, r*, C_P denotes the 3D coordinate of any point in the image within the F_c frame, and the term C_{O_B} corresponds to the rotational center. With the availability of an inertial mechanization and aiding position estimation methods such as GPS or even geomagnetic estimation, this model can then be formulated as follows:

$$\begin{bmatrix}\dot{\mu}\\ \dot{v}\end{bmatrix} = \begin{bmatrix}f\frac{u}{\eta_z} - \frac{\mu w}{\eta_z}\\ f\frac{v}{\eta_z} - \frac{vw}{\eta_z}\end{bmatrix} + \begin{bmatrix}fq + rv + \frac{p}{f}\mu v + \frac{q}{f}\mu^2\\ -fp + r\mu - \frac{p}{f}v^2 + \frac{q}{f}\mu v\end{bmatrix} \tag{39}$$

5.6 Earth's Geomagnetic Field

Initially, the sources affecting the total magnetic field can be classified into two main groups: internal and external, as illustrated in Figure 56. Internal sources refer to phenomena occurring below the surface level, such as the core field and anomaly field. In contrast, external sources encompass components unrelated to ground effects, such as ionospheric and magnetospheric fields.

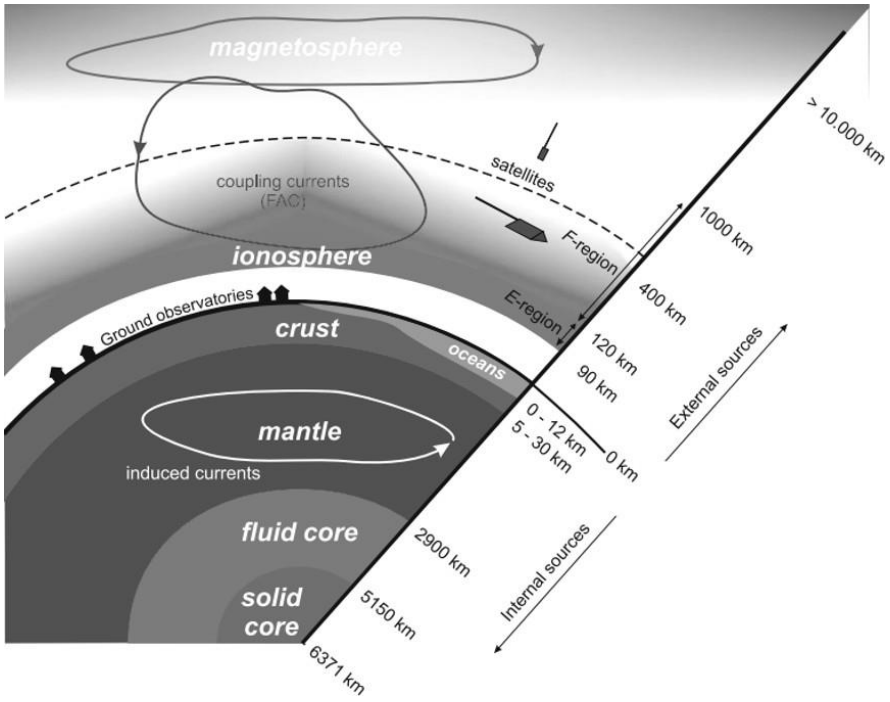

Figure 56. Sources contributing near-Earth magnetic field. (W. Freeden, M. Z. Nashed, and T. Sonar 2010).

Internal contributions to the magnetic field include the core magnetic field, accounting for around 95-99% of the total measured field, which is induced by electric currents generated by the movement of molten iron and nickel around the outer core (Gubbins 2010). Complex spherical harmonic models of this component are updated every five years to account for secular variations (Jacobs 1985) (Alken et al. 2021). Lastly, the anomaly field, generated by the concentration of magnetized rocks in the Earth's crust, provides high spatial-frequency information suitable for map-based navigation, especially at lower altitudes, and accounts for 1-5% of the total measured field.

External contributions to the total magnetic field, often denoted as external variations or disturbances, occur in the ionosphere and magnetosphere. The solar radiation creates an electrically conducting plasma in the ionosphere that induces a magnetic field, resulting in regular daily variations observed in magnetograms of magnetic quiet days (W. Freeden, M. Z. Nashed, and T. Sonar 2010). Simultaneously, variations occur due to magnetic storms from the magnetosphere, driven by solar winds composed of charged particles that interact with the Earth's magnetic field (Alexeev et al., n.d.) (Potemra 1984).

For air navigation, various studies have demonstrated the potential of magnetic fields for geo-localization development ("Absolute Postioning Using the Earth's Magnetic Anomaly Field - ProQuest" n.d.) (Goldenberg 2006). A key observation is that the magnetic anomaly field offers more accurate localization due to its high-frequency content. This provides several advantages over other navigation approaches, as the anomaly field is independent of weather conditions and time of day.

After understanding the main components of the total magnetic field, it is crucial to provide a detailed mathematical description to isolate the anomaly field component. When a magnetic field measurement is taken, it is necessary to compensate for all other components of the total magnetic field to isolate the crustal field's influence. To achieve this, a general measurement equation can be defined that includes all the possible sources previously mentioned, which contribute to the observations:

$$H_{Total}(\theta,\phi,r,t) = B_{crust}(\theta,\phi,r) + B_{core}(\theta,\phi,r,t) + B_{ext}(\theta,\phi,r,t) + V + \delta B_{crust} + \delta B_{core} + \omega + b \qquad (40)$$

Equation 40 describes any given magnetometer measurement $H_{T\ otal}$, at a given coordinate θ,ϕ,r, at the time t, as a composition of the anomaly component $B_{crust}(\theta, \phi, r)$ and its error δB_{crust}, plus the Core field component $B_{core}(\theta, \phi, r, t)$ and its error δB_{core}, plus the possible external variations $B_{ext}(\theta, \phi, r, t)$, plus the influence of the vehicle structure V if exists, and the sensor noise ω and bias b. Finally, a mathematical description of each of the components is defined independently since the total magnetic field can be seen as a superposition of the individual influences presented in Eq. 40 (Cuenca and Moncayo 2021b).

5.6.1 Mathematical Model

The core field, $B_{core}(\theta, \phi, r, t)$, is well studied and currently described by the International Geomagnetic Reference Field (IGRF) model (Blakely 1996) (Sabaka et al. 2015) (Sabaka, Olsen, and Langel 2002). This model comprises a series of mathematical representations of the internal geomagnetic field and its annual rate of change, known as secular variations, using a spherical harmonic analysis. This method aims to describe the core field mathematically from measurements over a spherical shape. The IGRF model presents the base equations of the spherical analysis and provides the coefficients based on ground and satellite data collected over several years. The magnetic field is defined in terms of a magnetic scalar potential V, where $B = -\nabla V$. The potential V is approximated by a finite series as follows:

$$V(r,\theta,\phi) = a\sum_{n=1}^{k}\left(\frac{a}{r}\right)^{n+1}\sum_{m=0}^{n}\left(g_n^m cosm\phi + h_n^m sinm\phi\right) P_n^m(cos\theta) \qquad (41)$$

In Equation 41, a is the Earth's radius, r is the radius coordinate of the point of interest with given longitude ϕ, and co-latitude θ. The coefficients g_n^m and h_n^m are called Gaussian coefficients, and $P_n^m(\theta)$ is the Schmidt quasi-normalized Legendre functions of degree n and order m (Davis 2004) . The latest IGRF-13 model provides the low order Gauss coefficients g_n^m and h_n^m for the core main filed, as these initial terms represent largely the core's influence (Blakely 1996) . As shown in Figure 57, the power contributions of the first 10 to 15 orders are due to the core field (Alken et al. 2021) (Thébault et al. 2015) (Davis 2004). It is important to note that the magnetic field strength is calculated from the partial derivatives of Eq. 41, which is equivalent to the following derivation (Davis 2004) :

$$B_r = -\frac{\partial V}{\partial r} = \sum_{n=1}^{k}\left(\frac{a}{r}\right)^{n+2}(n+1)\sum_{m=0}^{n}\left(g_n^m cosm\phi + h_n^m sinm\phi\right) P_n^m(cos\theta) \qquad (42)$$

$$B_\theta = -\frac{\partial V}{r\,\partial\theta} = -\sum_{n=1}^{k}\left(\frac{a}{r}\right)^{n+2}\sum_{m=0}^{n}(g_n^m cosm\phi + h_n^m sinm\phi)\frac{\partial P_n^m(cos\theta)}{\partial\theta} \tag{43}$$

$$B_\phi = -\frac{\partial V}{rsin\theta\,\partial\phi} = \frac{-1}{sin\theta}\sum_{n=1}^{k}\left(\frac{a}{r}\right)^{n+2}\sum_{m=0}^{n} m\,(-g_n^m sinm\phi + h_n^m cosm\phi)P_n^m(cos\theta) \tag{44}$$

The terms B_r,B_θ and B_ϕ correspond to the field intensity in local tangential coordinates. The Legendre polynomials related to each harmonic are a set of orthogonal polynomials that satisfy the zero mean and its solution becomes the Rodriges's formula for a given an independent variable *v* (Butcher 2019), (Davis 2004):

$$P_n(v) = \frac{1}{2^n n!}\left(\frac{d}{dv}\right)^n (v^2-1)^n \tag{45}$$

The associated Legendre polynomial related to the Legendre polynomials in Eq. 45 is defined as:

$$P_{n,m}(v) = (1-v^2)^{\frac{1}{2m}}\frac{d^m}{dv^m}\left(P_n(v)\right) \tag{46}$$

As denoted by different authors (Sabaka, Olsen, and Langel 2002), (Davis 2004), it is required to use the quasi-normalized associated Legendre polynomials, which means that Eq. 46 must be normalized. In magnetic modeling, the Schmidt quasi (semi) normalized form P_n^m is used and can be described as follows:

$$P_n^m(v) = \left(\frac{2(n-m)!}{(n+m)!}\right)^{\frac{1}{2}} P_{n,m}(v) \tag{47}$$

Recursive formulas for the quasi-normalized associated Legendre polynomials are provided in (Butcher 2019) and as previously mentioned, the Gauss coefficients for different epochs are available in the IGRF model.

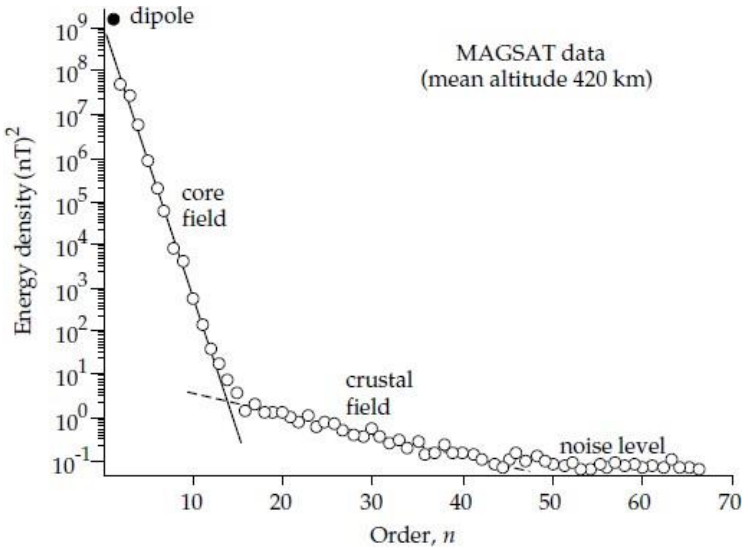

Figure 57. The energy density spectrum is derived from measurements of the geomagnetic field. (Lowrie and Fichtner 2020).

It is crucial to note that a solution for the crustal magnetic field can also be obtained using spherical harmonics with high-order coefficients, as illustrated in Figure 57. Models like EMAG2 (Maus et al. 2007) use Gauss coefficients from order 16 to 740, calculated based on ground, satellite, maritime, and airborne observations, as high spatial frequency components can be measured at lower distances. These coefficients are available from public databases such as the National Oceanic and Atmospheric Administration (NOAA) (Langlais n.d.). However, these models are still incapable of providing the high spatial frequency of wavelengths required for accurate navigation. Consequently, local or regional magnetic surveys become more useful for constructing maps for geomagnetic navigation purposes.

5.6.2 Regional Databases

One alternative approach to model the magnetic field, particularly for local regions with refined resolution, is by measuring the local intensity, subtracting the IGRF model, and accounting for diurnal variations. The database can then be constructed manually by extensively measuring the area of interest and post-processing to isolate the crustal influence, as shown in Figure 58, for example. Some research studies, such as (Canciani and Raquet 2016) (Pei et al. 2017), performed manual mapping and compared the model with previous mappings to ensure map stability.

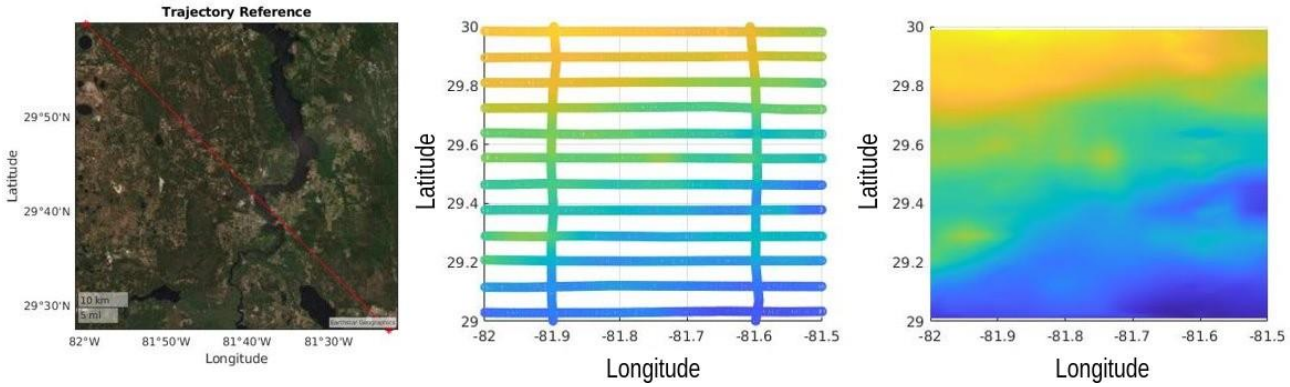

Figure 58. Anomaly magnetic mapping by extensive aerial measurements.

The United States Geological Survey conducts geomagnetic surveys to map and monitor the Earth's magnetic field, which is essential for various applications such as navigation, mineral exploration, and geophysical research. These surveys are carried out using airborne, marine, and ground-based platforms, providing high- resolution and accurate magnetic data of the Earth's crust (Langlais n.d.). The acquired data are processed and made available to the public through the USGS Geomagnetic Data Portal, which includes magnetic anomaly maps and databases.

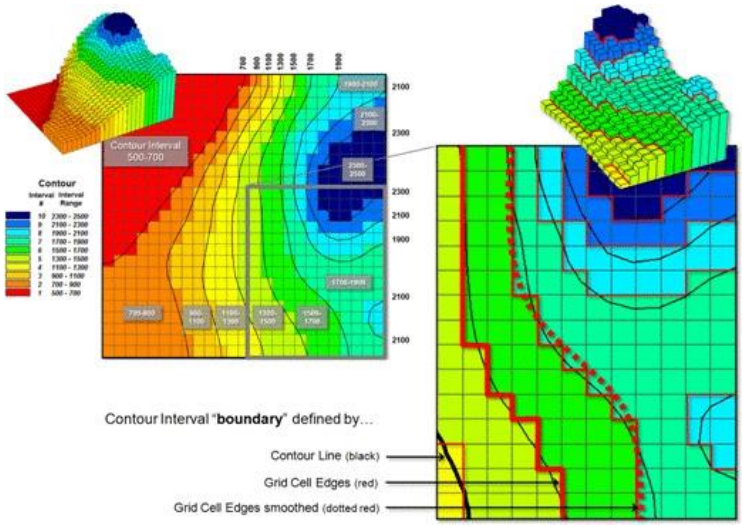

Figure 59. Grid representation of Magnetic databases and Contour lines (Berry 2007).

Commonly, over these magnetic surveys, data is collected at specific grid points, and interpolation techniques are employed to fill the gaps between these points as presented in Figure 58, creating a comprehensive representation of the geomagnetic field in the surveyed area. Each grid square is assigned an average magnetic value derived from its corner points, resulting in a discrete representation of the geomagnetic survey, as depicted in the Figure 59. Here, contour lines on the

geomagnetic survey maps follow a steep shape determined by the smoothness of the grid resolution (Berry 2007).

5.6.3 Matching Process

The matching process is the mechanism by which geomagnetic measurements taken by the vehicle are correlated with the geomagnetic database to infer the vehicle's position. In this project, the proposed matching mechanism is the Iterative Closest Contour Point (ICCP) (Cuenca and Moncayo 2021a). This method assumes that a GNSS signal is available, even if degraded, and that additional velocity measurements are provided, such as those from Optical Flow Visual Odometry. It is important to note that this implementation is not recommended for dead-reckoning scenarios, as the ICCP process heavily relies on the INS solution. In such cases, more robust and suitable approaches like Particle Filtering (Cuenca and Moncayo 2023) or Gradient Matching Process (Canciani and Raquet 2016) are recommended.

The ICCP algorithm is a widely used method in geomagnetic contour matching (Xiao et al. 2020) (Duan et al. 2019). It approximates the history of magnetic measurements to a possible path that closely correlates with the magnetic strength. In addition to requiring a geomagnetic database, this method assumes that the vehicle's real position is sufficiently close to the corresponding magnetic contour of the measurement. If this assumption does not hold, the algorithm's accuracy may be significantly reduced. Furthermore, a Nearest Euclidean Distance Point (NEDP) algorithm is employed to find the closest point on the measurement contour from the geomagnetic correction.

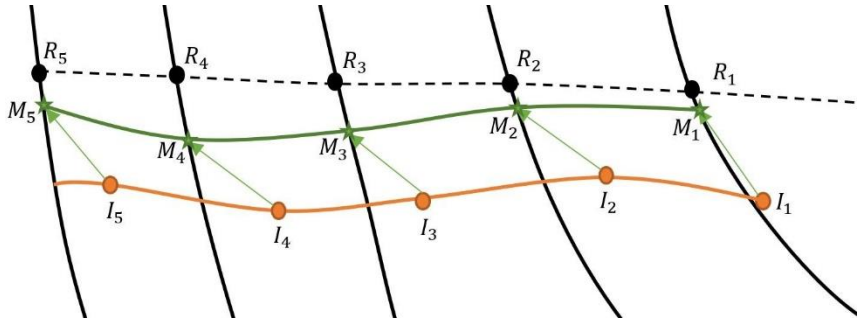

Figure 60. Illustration of the Geomagnetic Matching through Contour Point.

As illustrated in Figure 60, the algorithm takes estimated points I_1, ..., I_5 from an INS and uses ICCP algorithm to determine the geomagnetic path closest to the magnetic measurements. Afterwards, the NEDP algorithm finds at every iteration, the position that best matches the measurement contour line, resulting in the M_1, ..., M_5 geomagnetic position estimates. This approximation will determine the position that shares the same contour line, from the geomagnetic map, as the real path R_1, ..., R_5.

Traditional matching methods have two main characteristics, searching strategy and correlation length. The searching strategy is carried inside an uncertainty area U, normally defined by the INS's uncertainty, which represents its standard deviation within a Gaussian distribution. This brings up a limitation to the matching algorithm as the bigger the data set to be compared, the less computationally efficient the matching will be. As defined in Eq. (48), a good rule of thumb is to define an area of

maximum $+/-3\sigma$ around the INS point since a 3σ represents the boundaries where 99.73% of the probabilities will rely in a Gaussian distribution.

$$U = \left[(x, y), \left|x - \hat{S}_x\right| \leq 3\sigma \;\&\; \left|y - \hat{S}_y\right| \leq 3\sigma\right] \tag{48}$$

Although the uncertainty area is defined by a circle with radius 3σ, a square shape is selected due to computational adaptability. Additionally, it is possible to define the boundaries for the X and Y positions if the independent covariances are available respectively.

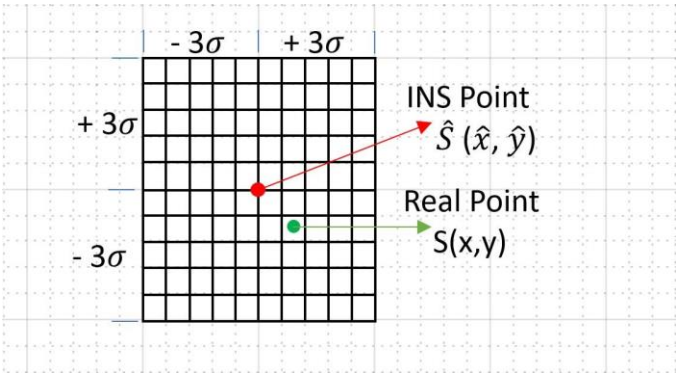

Figure 61. Uncertainty Area Boundaries.

When the vehicle starts navigating, magnetometer sensors measures the magnetic field's magnitude, $H_m = [h_{m,1}, h_{m,2}, ..., h_{m,N}]$ at each time step (k; 1,2,...,N). Additionally, each value of H_m is associated with a position in space estimated by the INS that will be denoted as $\hat{S}$. Given this statement, there will be N position points that defines the entire trajectory $\hat{S} = [\hat{S}_1, \hat{S}_2, ... \hat{S}_N]$. Following Eq. (48), the uncertainty area can be described as in Figure 61. It must be emphasized that the uncertainty area can be variable if independent covariances for the positions are available.

Each point within the uncertainty area, denoted as $U(i, j)$, has a magnetic value defined by the map. The objective is to compare the measurement taken at sample time k with all the magnetic values assigned to each point in the area. A straightforward initial approach is to select the magnetic value of the uncertainty area closest to the taken measurement at each iteration, as shown in Eq. (49). However, all measurement systems inherently suffer from noise and external factors that may cause disturbances, introducing additional noise into the correlation. As a result, it is necessary to develop a more robust expression like Eq. (50), which considers prior measurements instead of relying solely on Eq. (49).

$$min\big(CP(i,j)\big) = \left|H_{U(i,j),k} - H_{m,k}\right|, (i,j) \in U \tag{49}$$

There are four important correlation rules used in correlative analysis: Product Correlation (PROD), Normalized Product Correlation (NPROD), Mean Absolute Deviation (MAD), and mean variance algorithm (Ying Liu et al. 2008) (Wei et al. 2011). PROD and NPROD focus on the similarity between two sets, while MAD emphasizes the degree of difference between the sets. Although all options are widely used, the MAD algorithm has been chosen for this study based on references (Ying Liu et al. 2008) (Chang 2017), and it follows the mathematical expression as follows:

$$min\big(MAD(i,j)\big) = \frac{1}{N}\sum_{k=1}^{N}\left|H_{U(i,j),k} - H_{m,k}\right|, (i,j) \in U \quad (50)$$

Equation (50) is evaluated for the entire trajectory, referring to all the sampled times of the mission. However, it is important to note that the longer the set of points being evaluated, the higher the potential false certainty of the algorithm, which may converge to an incorrect unique solution. Conversely, using a short set of points may cause the algorithm to constantly switch between guesses due to noise interference affecting overall convergence. Within this algorithm, it is assumed that there are *i* by *j* parallel paths to be compared with the measured sequence H_m. The MAD algorithm identifies the path in the uncertainty area that deviates the least from the measured sequence.

Finally, it is used the nearest Euclidean distance to assign the highest probability to the closest point on the map with the same magnetic value measured by the sensor. Figure 62 illustrates an example of the algorithm's approximation. In the implementation, the location of each point matching the contour curve is compared to the location of the estimated position, and the closest one becomes the most probable estimation. This process is carried out to enhance the reliability of the geomagnetic estimation.

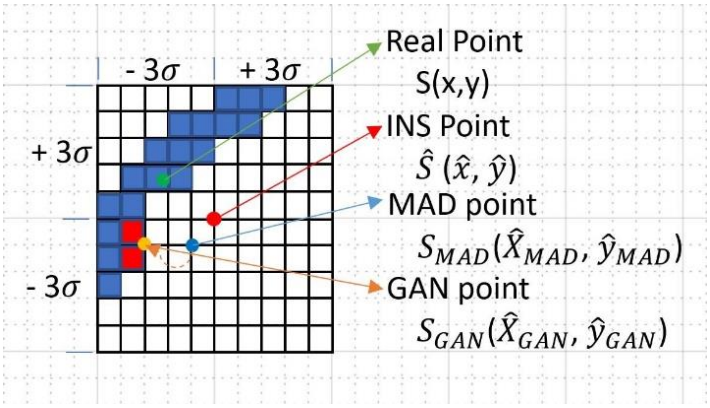

Figure 62. Representation of the Nearest Distant point.

The NEDP can be calculated by evaluating the 2D distance of all the points in the uncertainty area against the geomagnetic matching position. This can be represented as shown in Eq. 51, where $\hat{X}_{GMA}$ and $\hat{Y}_{GMA}$ is the resulting location from the MAD algorithm at the given iteration, and $X_{H_{m,k}}$ and $Y_{H_{x,k}}$ are all the locations that satisfy the measurement contour curve inside the uncertainty are

$$\hat{\boldsymbol{X}}_{\boldsymbol{NP}} = \boldsymbol{min}\sqrt{(\hat{\boldsymbol{X}}_{\boldsymbol{GMA}} - \boldsymbol{X}_{\boldsymbol{H_{m,k}}}(\boldsymbol{i},\boldsymbol{j}))^2 + (\hat{\boldsymbol{Y}}_{\boldsymbol{GMA}} - \boldsymbol{Y}_{\boldsymbol{H_{m,k}}}(\boldsymbol{i},\boldsymbol{j}))^2} \quad (\mathbf{51})$$

5.7 Test and Evaluation of the Developed Systems

The test and evaluation phase of the developed systems encompasses both the Optical Flow visual odometry system as well as an initial approach of the geomagnetic navigation system using the ICCP algorithm and the NEDP algorithm. This section focuses on test cases used to assess the accuracy,

reliability, and robustness of these integrated systems. The general architecture of the framework remains as presented in Figure 46, with the guidance and navigation depicted in Figure 53, and the controller illustrated in Figure 52.

Testing the combined system involves simulating and conducting real-world experiments where the vehicle's magnetic measurements are matched with the geomagnetic database for position estimation, while simultaneously utilizing the Optical Flow system for velocity measurements. Evaluation metrics should consider the accuracy of the position and velocity estimations, the ability to handle noise and external factors, the overall computational efficiency, and the performance of the integrated systems.

5.7.1 Performance Over Degraded Accessibility

A test case scenario is proposed by commanding the reference trajectory depicted in Figure 49, over the designed environment under a set of initial conditions for the satellite model and vehicle. The evaluation of visible satellites is performed at every time step of a mission simulation within the world map by using the Ephemeris model and the proposed signal shadowing algorithm. With this approach, it is possible to calculate the visible satellites across the entire map at a given Epoch, as shown in Figure 63. The satellite availability is represented as a heat map, illustrating the number of directly visible satellites.

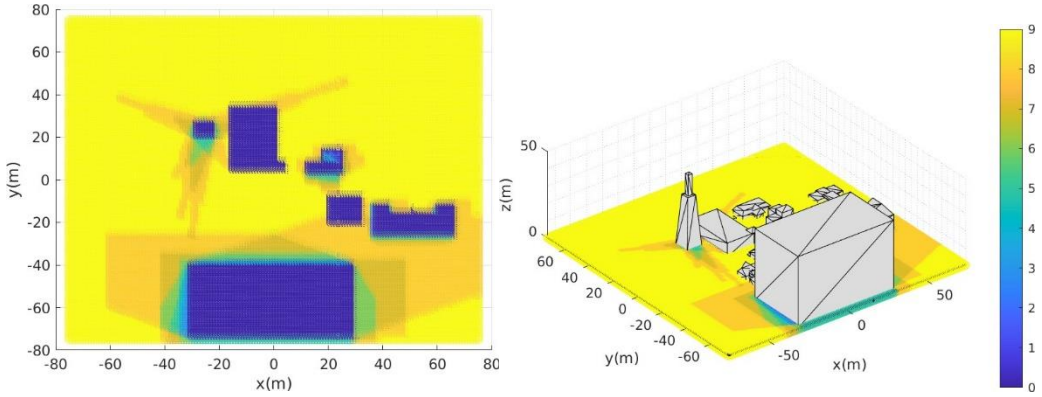

Figure 63 .Heat map of Available Satellites within a Defined Epoch @ Z=8m.

Additionally, the position uncertainty covariance given by the model is calculated by means of the Position Dilution Of Precision (PDOP), which is highly dependent on satellite geometry. Commonly, but not necessarily, there is a correlation between the increase in uncertainty and the reduction in the number of visible satellites. This relationship can be observed in Figure 64 for the presented case (A. Cuenca and H. Moncayo 2023).

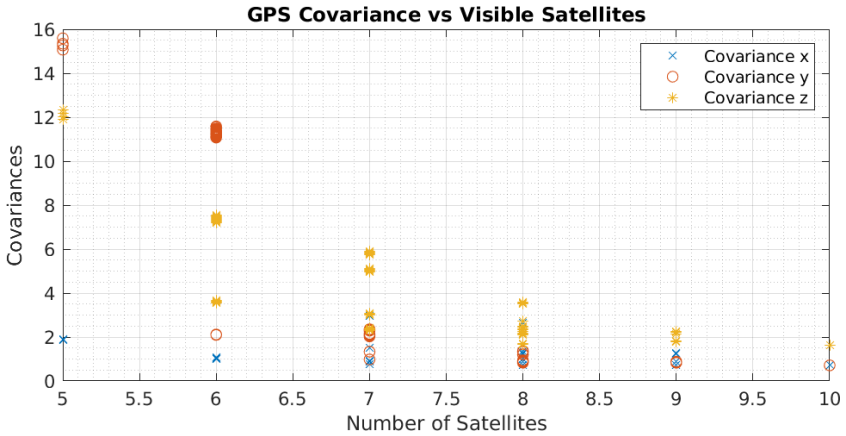

Figure 64. Relation between Positioning uncertainty and visible Satellites

Areas with a higher number of visible satellites tend to have lower PDOP values, indicating better access to a geometrical distribution of satellites and, consequently, a more accurate position estimation. Conversely, areas with fewer visible satellites typically exhibit higher PDOP values, reflecting the degraded satellite geometry and resulting in a less accurate position estimation.

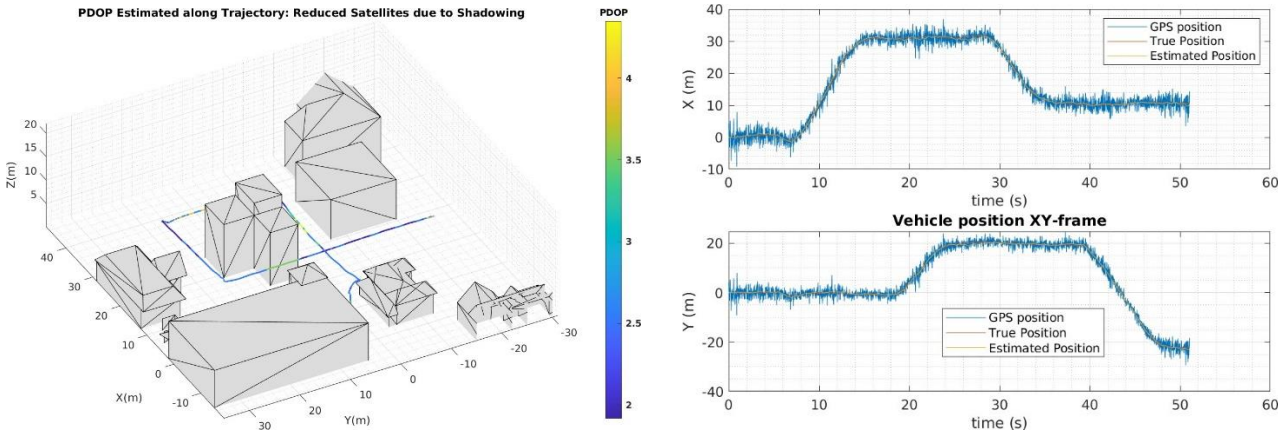

Figure 65. Vehicle Position estimation without enhancing strategies Vehicle Trajectory and PDOP, Vehicle Positioning over plane XY.

Finally, the position estimation was obtained through the fusion of sensor data and GPS signal integration under the Kalman filter framework. Figure 65 illustrates the executed trajectory, the PDOP obtained by the visible sequences of satellites over the trajectory, and the resulting position estimation, which could oscillate around eight meters. This level of accuracy is generally considered to be relatively low for UAV operations.

Despite the relatively low accuracy in certain parts of the trajectory, the integration of sensor data and GPS signals through the Kalman filter can still provide valuable information for navigation and control purposes. However, it is crucial to recognize the limitations of the system's performance in

these conditions and consider additional strategies or sensor modalities to enhance the overall accuracy and reliability of the navigation system for UAV operations.

5.8 Optical Flow Integration

The simulation environment offers a flexible platform for integrating various sensors to the vehicle model, enabling a comprehensive evaluation of their performance under different conditions. In this case, a monocular camera with a resolution of 752x480 pixels and a focal length of 230 was incorporated into the simulation, along with an ultrasound sensor for altitude measurement as shown in Figure 66. These sensors provide the required data for the Optical Flow visual odometry system.

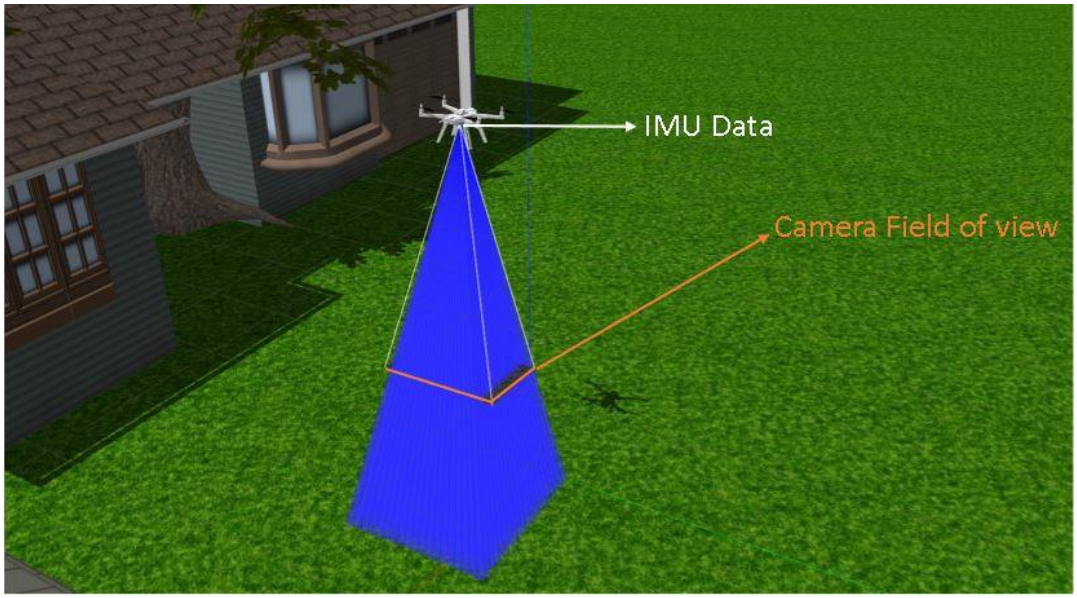

Figure 66. Simulated Camera Field for Optical Flow Assessment.

The simulation environment allowed to capture from the monocular camera, images at a frame rate of 30 frames per second, as well as Inertial Measurements provided at a rate of 100 Hz. To effectively process the data from the monocular camera, the Shi-Tomasi feature detection algorithm was employed to identify salient visual features in each image frame. The Lucas-Kanade Optical Flow algorithm was then used to track the movement of these features between consecutive frames as illustrated in the sequence depicted in

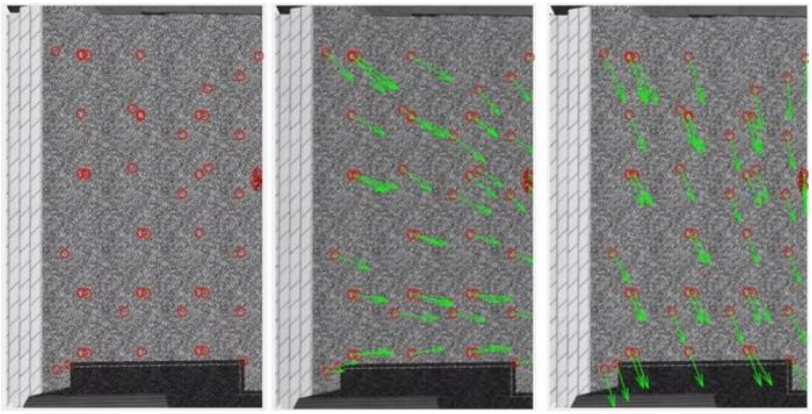

Figure 67, yielding estimates of their 2D displacement in the image plane. By combining this information with the pinhole camera model, the 3D motion of the vehicle could be estimated in the world frame.

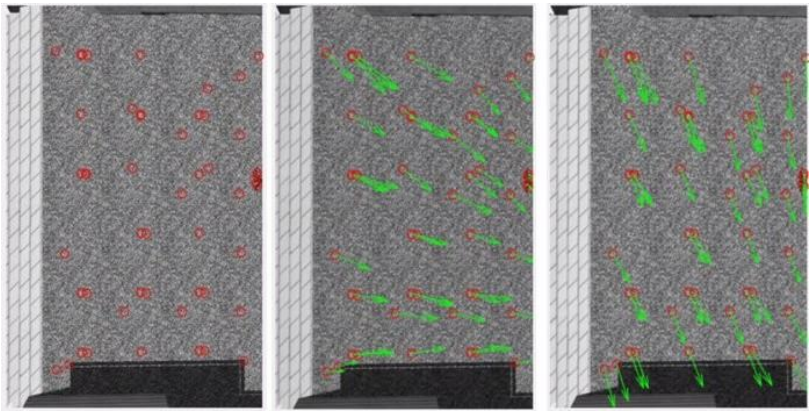

Figure 67. Consecutive Camera Frame Sequence and its Optical Flow Visualization.

Figure 68 presents the results of the vehicle velocity estimation derived from only the Optical Flow visual odometry system. The graph illustrates that the velocity estimation is quite accurate when features are available. It is noteworthy that there is some low-level noise present in the estimated velocity, which can be attributed to the vibrations of the vehicle while in motion. These vibrations can cause slight oscillations of the image pixels captured by the camera, subsequently affecting the Optical Flow calculations.

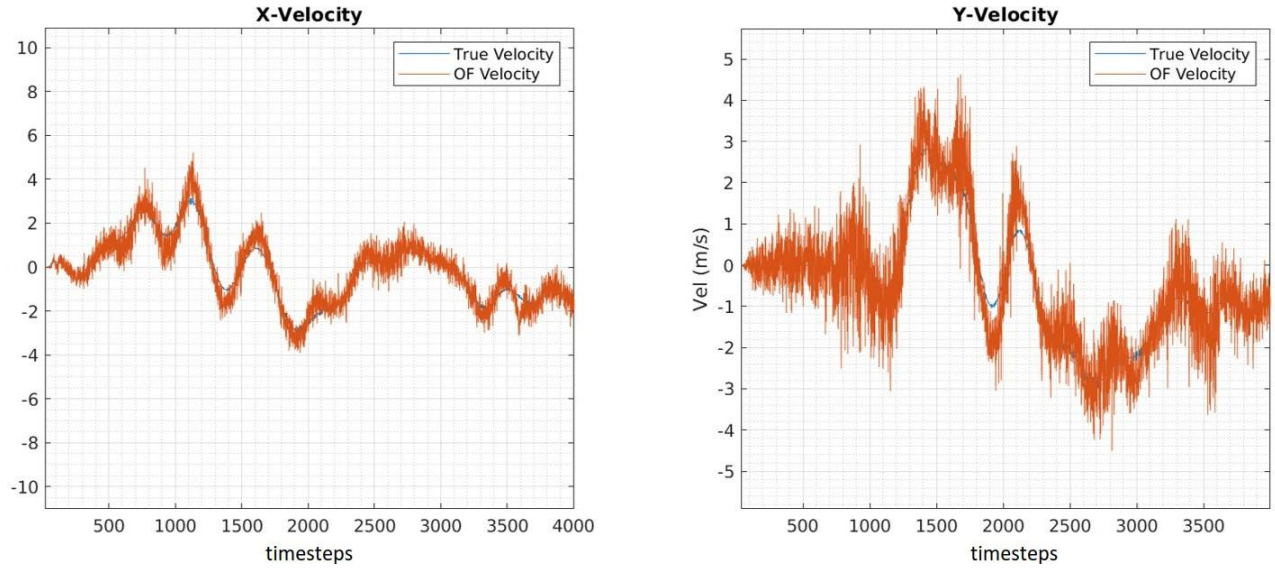

Figure 68. Velocity Measurements by only Optical Flow Odometry.

The Optical Flow velocity measurements were subsequently incorporated into the Kalman Filter estimator, without including any geomagnetic algorithms at this stage. Figure 71 demonstrates the filtered velocity estimation, even when integrating degraded GPS signals due to shadowing effects. The integration of Optical Flow measurements with the Kalman Filter effectively compensates for the reduced accuracy of GPS signals, which can be compromised under certain environmental conditions or in the presence of obstacles.

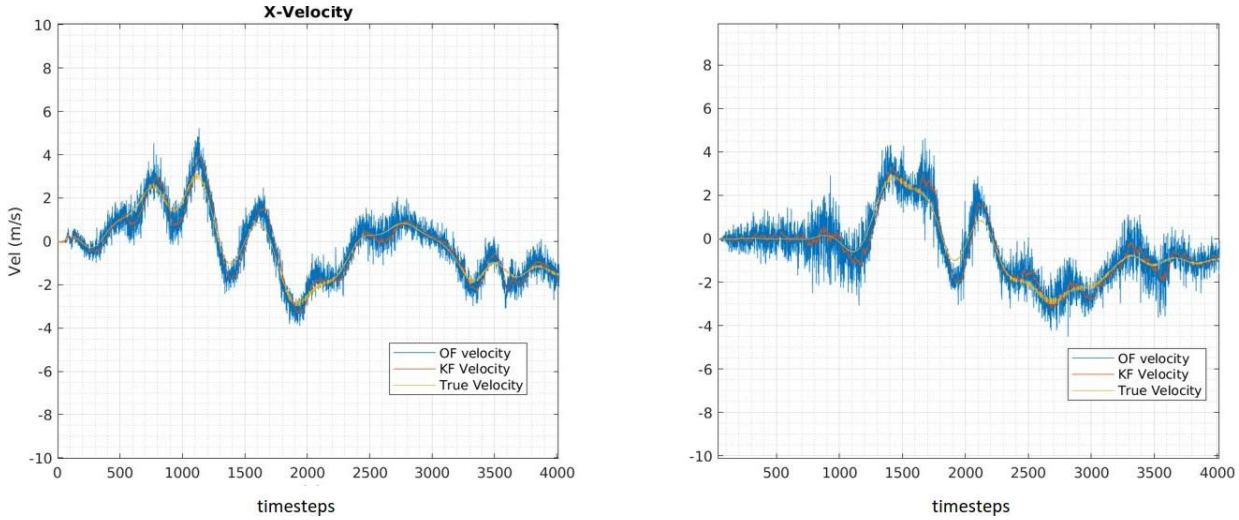

Figure 69. Velocity Estimation integrating OF Velocity Measurements.

Furthermore, the position estimation from the Kalman filter is also computed using velocity estimations from the Optical Flow odometry as measurement source, in conjunction with GPS positional measurements. This results in a significant improvement in the position estimation. This

improvement can be attributed to the increased measurement update rate obtained from the Optical Flow odometry compared to the GPS update rate. Additionally, the Optical Flow measurements are independent of satellite distribution, which represents an additional source of information to correct the noise from GPS measurements in areas where GPS signals might be degraded.

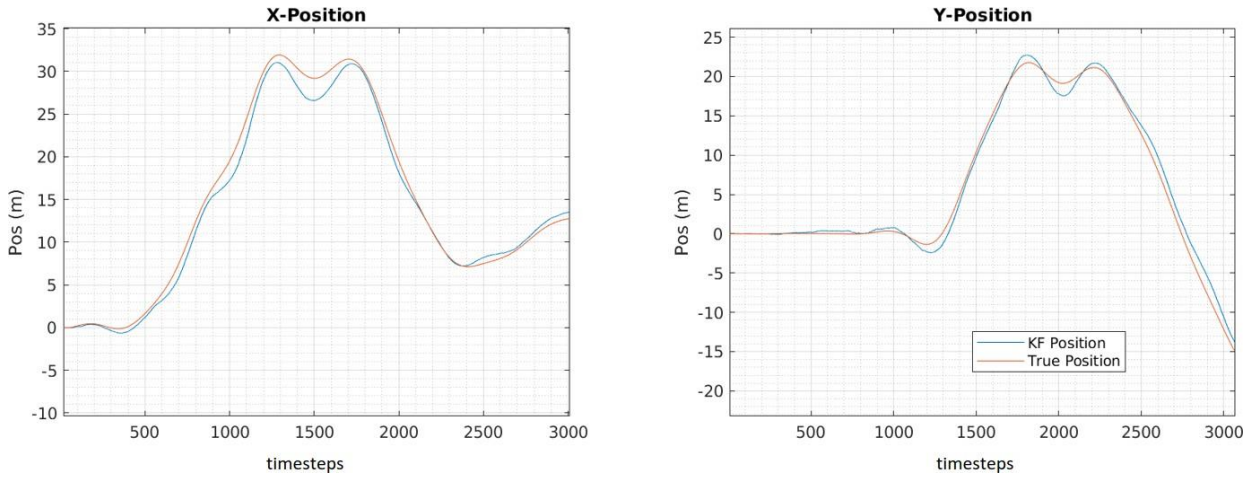

Figure 70. Position Estimation integrating OF Velocity Measurements.

By incorporating the Optical Flow odometry, the navigation system is more robust against GPS signal degradation and can provide more accurate position estimates in a wider range of environments. This demonstrates the effectiveness of using a multi-sensor approach to enhance the overall accuracy and reliability of the navigation system for UAV operations, especially in challenging environments where the performance of standalone GPS systems may be compromised.

5.8.1 Physical Implementation Remarks

A dataset from a real flight test was provided to the team for further testing of the Optical Flow algorithm in a real-world implementation. The dataset included Inertial measurements, camera images, and GPS information contained in a ROS bag file. The Optical Flow algorithm was applied to this dataset, following the same sequence of steps as in the simulation environment. Figure 71 presents the Optical Flow steps applied over frames of the provided flight test data.

The successful application of the Optical Flow algorithm to real flight test data demonstrates the robustness and adaptability of the proposed approach. By combining the Optical Flow odometry with the sensor data, it was possible to estimate the vehicle velocity using both the INS/GNSS loosely coupled integration as illustrated in the Figure 72 and separately, the visual odometry through Optical Flow as depicted in Figure 73.

The INS/GNSS integration combined the IMU data with the GPS information to generate an initial velocity estimation, while the visual odometry through Optical Flow was applied to the video to obtain an independent velocity measurement. These results were then compared to assess the performance of the Optical Flow algorithm in real-world environments.

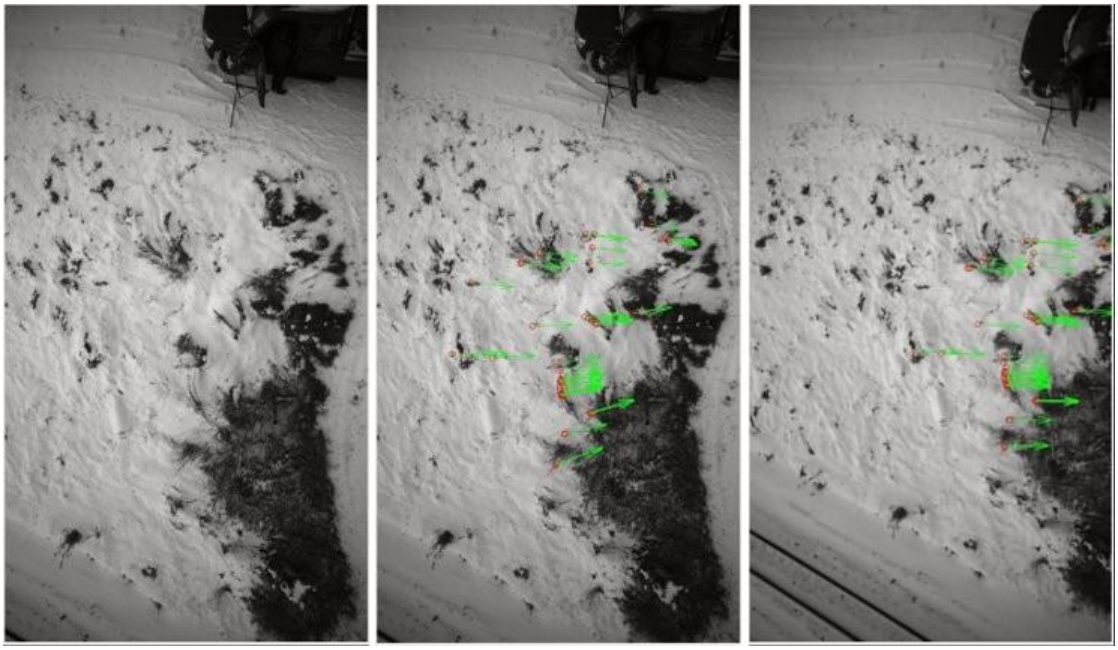

Figure 71. Consecutive Real Camera Frame Sequence and its Optical Flow Visualization.

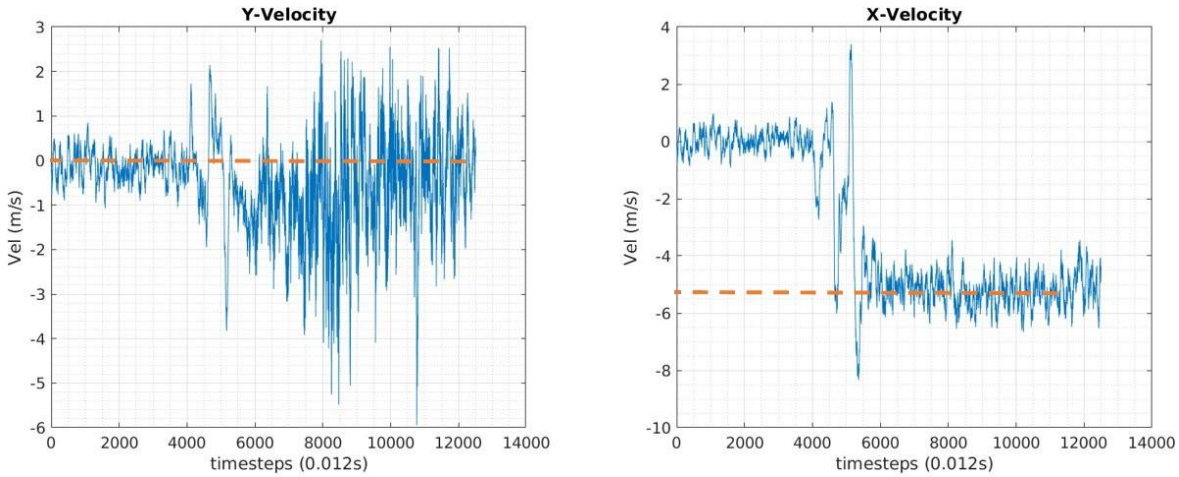

Figure 72 .Vehicle Kalman Filter Velocity Estimation INS/GNSS Loosely Coupled integration.

The velocity estimations highlight the effectiveness of the Optical Flow algorithm in providing accurate velocity estimates, even when used independently from the other sensor data. It also emphasizes the importance of using a multi-sensor approach for enhancing the overall accuracy and reliability of the navigation system. It is worth to mention that the result presented over this report of the optical flow velocity measurements correspond only for a small fraction of time after take of while the Kalman filter estimation without OF was calculated over the whole dataset, hence, the timestep differences.

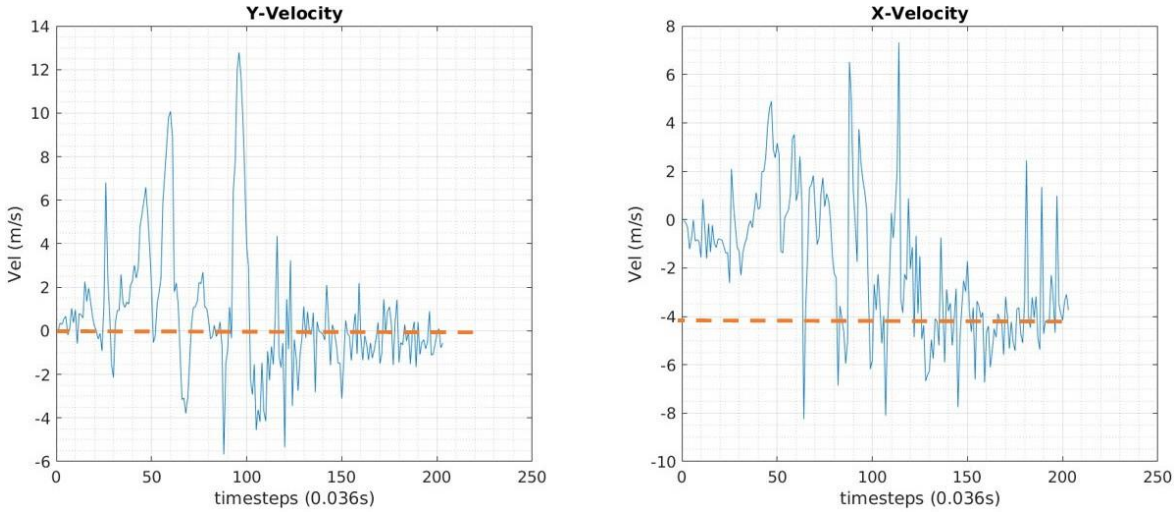

Figure 73. Velocity Measurements by only Optical Flow Odometry in real Data.

Maintaining constant altitude measurements and stable camera orientation is crucial for optimal performance of optical flow algorithms. However, it is worth noting that using high-resolution cameras may introduce challenges due to the increased computational demands associated with processing more pixels for feature detection. Consequently, low-resolution cameras are better suited for these types of implementations, as they offer a balance between accuracy and computational efficiency.

5.9 Geomagnetic Positioning Integration

The research team has conducted extensive research on geomagnetic localization approaches, primarily focusing on airborne navigation (Cuenca and Moncayo 2021b) (Cuenca and Moncayo 2021a) (Cuenca and Moncayo 2023), which represents a distinct navigation environment. A key consideration in urban environments is the magnetic distortion caused by buildings in the area, which affects the local anomaly field due to man-made disruptions. Consequently, it is contemplated that magnetic mapping of urban areas may be necessary to capture the structural distortions of the field. However, it is important to note that there is no guarantee that these distortions will remain constant over time and cannot work as perfect as indoor navigation approaches. Therefore, some analyses are presented over this project under severe assumptions as it is the existence of a refined magnetic map, and no magnetic disturbances due to motors over the simulation. It will be further discussed why these assumptions might not hold in urban environments.

A test case is defined for the navigation algorithm assessment using two proposed trajectories shown in blue over the illustration in Figure 74 with the corresponding anomaly geomagnetic map as the geomagnetic database. These cases simulate the drone flight over a small map with a known magnetic map under perfect conditions, with no external disturbances.

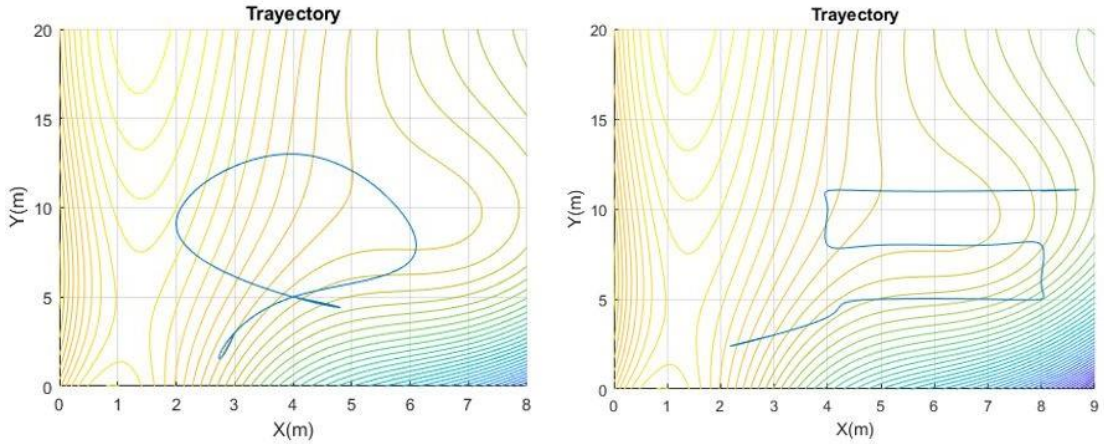

Figure 74. Trajectories proposed as study cases. a) O pattern, b) S pattern.

Alongside the Extended Kalman Filter, the geomagnetic matching algorithm, and the Nearest Contour Point method are integrated as supplementary modules. The results derived from the Geomagnetic Aided Navigation (GAN) algorithm, the INS, and EKF scenarios are presented concurrently to illustrate the performance of the algorithms graphically. The algorithm, once initialized, needs to build trust in its matching history. The matching method largely depends on a reliable position measurement and aims to correct the drift in the INS.

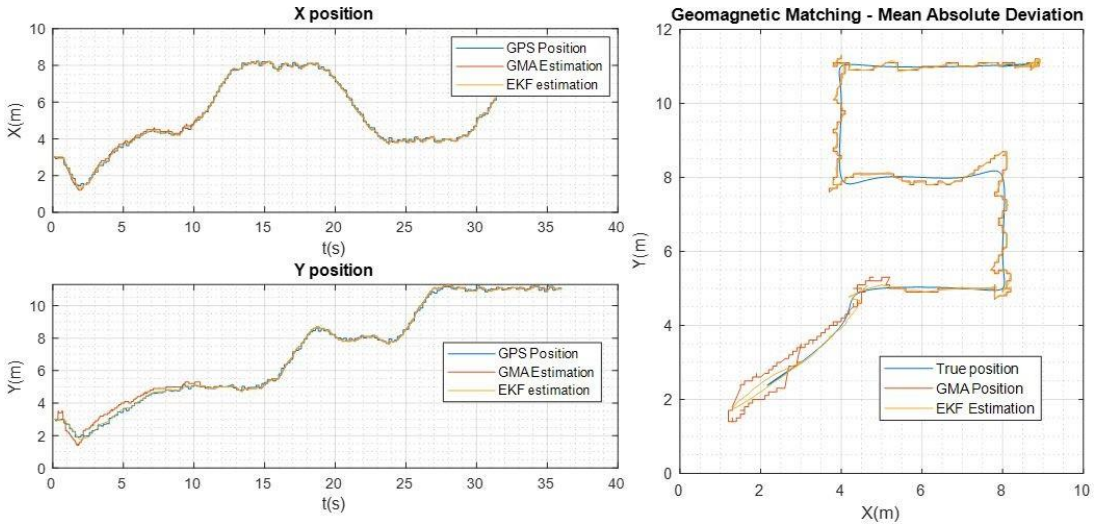

Figure 75. Trajectory S - Geomagnetic Matching Position estimation.

The results from both the S and O trajectories proposed, as demonstrated in Figure 75 and Figure 76, reveal that the MAD algorithm converges to the INS estimation point, which is at the center of the uncertainty area. This can be observed at 11s in Figure 75 and at 13s in Figure 76, where a jump in position estimation occurs.

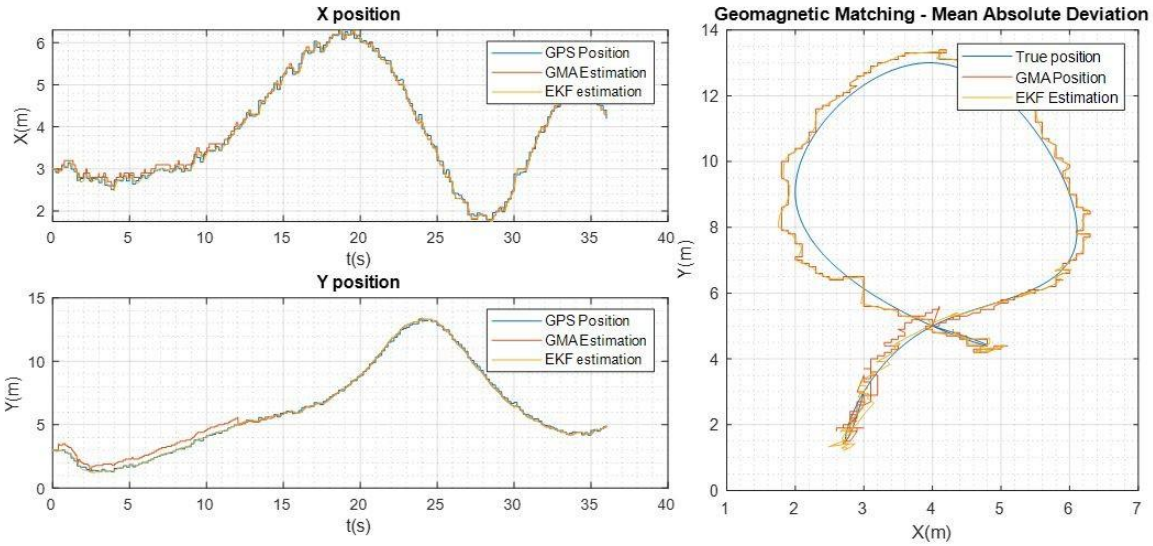

Figure 76. Trajectory O - Geomagnetic Matching Position estimation.

These findings suggest that the MAD algorithm places considerable trust in the INS estimation, which is primarily guided by the GPS measurements. Therefore, one of the analysis' obtained is that there exists a limitation of the algorithm on the GPS accuracy, although, it allows certain levels of uncertainty that is worth further study.

The NEDP block investigates the uncertainty area and approximates the point selected from the MAD algorithm in the Geomagnetic matching, to the closest position point of the contour lines that matches the measurement at that instant. This can be observed in Figure 77 where the blue box is the uncertainty area while the points marked by a blue X corresponds to positions with the same magnetic magnitude as the measurements inside the area.

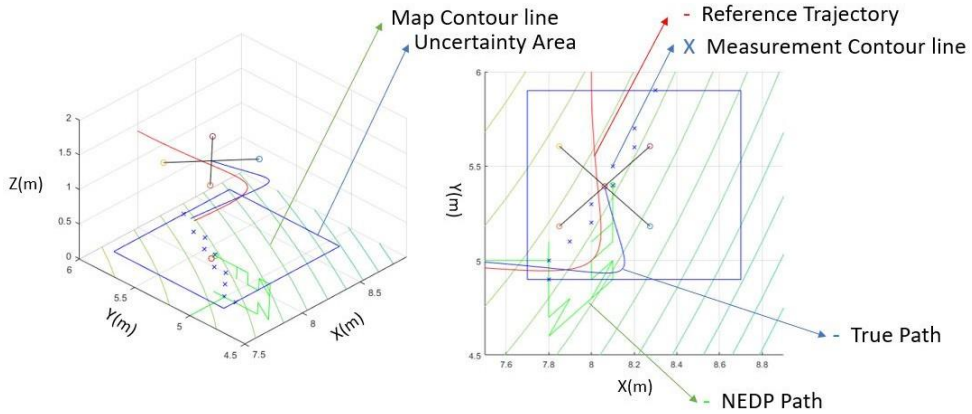

Figure 77. Closest Contour Point representation.

The simulation environment provides visual information of all the elements that structures the GAN architecture as presented in Figure 79 and Figure 78. When calculating the positions with the closest magnetic value as the measurement, a tolerance in the comparison can be defined. Depending on the

field's features, a high tolerance can be wise to use when the surface has a distinctive slope, while a low tolerance helps to prevent drifting when the surface is even.

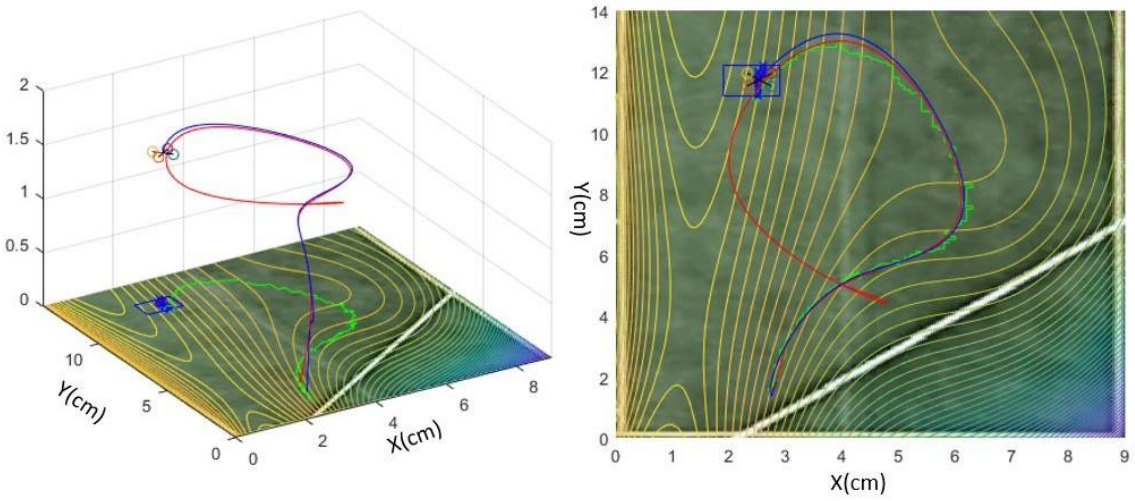

Figure 78. Trajectory O - 3D Visualization of GAN Path estimation.

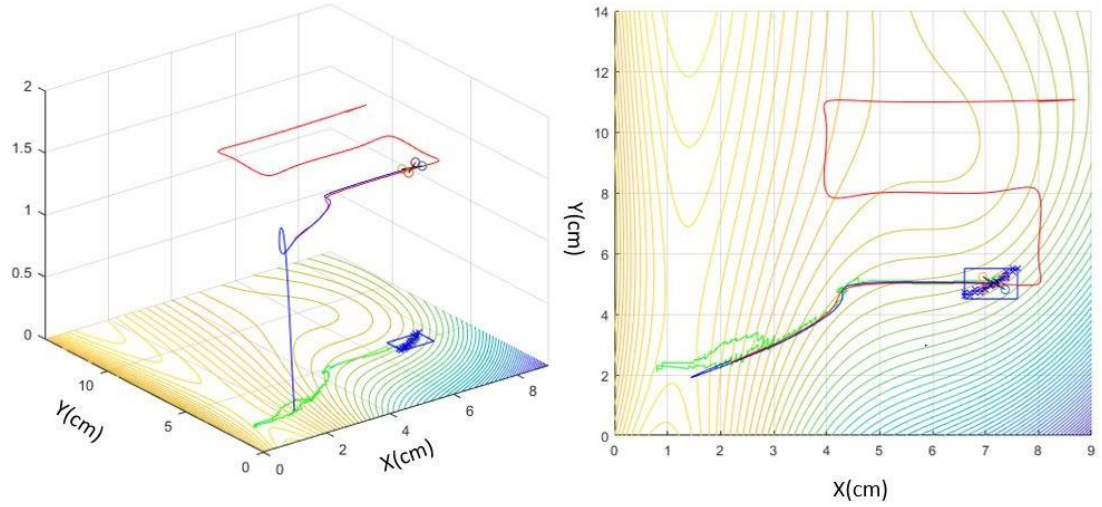

Figure 79. Trajectory S - 3D Visualization of GAN Path estimation.

A non-continuous pattern in the GAN estimation is observed since it depends on the resolution of the map grid. However, the information from the GAN algorithm is handled by the EKF estimation by smoothing the estimation. Again, the algorithm performs an enhancement of the position estimation with the geomagnetic referencing while still using GPS as main position measurement.

5.9.1 Physical Implementation Remarks

A series of flight tests, as illustrated in Figure 80, were conducted to gather sensor data from the field and evaluate the impact of the vehicle and its dynamics on the measurements. GPS data was also

recorded during all flights as a position reference value. The recorded data is stored on the PX4 SD card and requires post-processing in Matlab to be used as reference data for the GAN architecture implemented. These tests help to better understand the performance of the system under real-world conditions and to refine the algorithms accordingly.

Figure 80. Collection data Flight performed at ERAU's Softball Field.

During the post-processing of data gathered from various flights, several factors were identified that had a significant impact on the GAN algorithm. The most critical of these factors was the magnetic distortion of the field caused by the motors spinning. The motors, consisting of magnets with high currents flowing through them, generating magnetic fields that are still detected by the sensors. This introduces huge noises, which affects the magnetic measurements.

The magnetic distortion phenomenon is evident in Figure 81 when the motors are activated and the flight commences. The generated noise magnitude is significantly greater than the expected value derived from the map, emphasizing the considerable influence of this distortion on the system's performance.

Finally, the team is concurrently studying the MagNav.jl suite, a toolset developed by the MIT in collaboration with the Air Force. The suite offers a comprehensive set of tools tailored for airborne Magnetic Anomaly Navigation, encompassing features such as flight path and INS data import or simulation, mapping, aeromagnetic compensation, and navigation. The dataset provided within this suite was collected during a geosurvey in Canada at various altitudes, and it includes readings from five scalar magnetometers with different noise levels. Additionally, data from vector magnetometers are included, allowing for extensive testing of various geomagnetic algorithms.

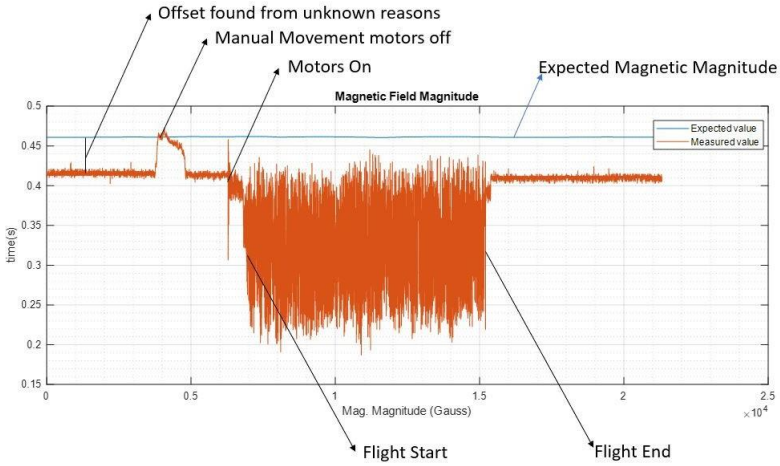

Figure 81. Flight test Magnetic Data.

5.9.2 Discussion and Recommendations

The subsequent section will delve into an analysis stemming from the research conducted by the team, drawing on the results obtained from the implementation of algorithms and simulations described in this report. This analysis will offer insights into the performance and efficacy of the methods and concluded remarks that have been developed and applied, helping to further understanding the complexities of Geomagnetic Aided Navigation, optical flow, and moreover, the operation of UAVs within Urban environments.

5.9.3 Simulation Environment

Gazebo is regarded as a highly potent tool for simulation, largely owing to its versatility and physics engine. Gazebo provides a robust and flexible platform that allows the simulation of complex environments and systems. It incorporates realistic physics for accurately modeling various phenomena such as lighting, gravity, and collision, among others. This realism, combined with its capacity to model a broad range of sensors and actuators, makes Gazebo an invaluable tool for testing, validating, and refining complex systems before deploying them in real-world scenarios.

On a specific consideration, it is important to note that the PDOP value derived from the GPS model in the simulation environment is not solely determined by the number of visible satellites; the geometric distribution of these satellites also plays a significant role in the overall positioning accuracy. As such, having a larger number of visible satellites does not always guarantee a lower PDOP value. Understanding the relationship between satellite visibility, satellite geometry, and the resulting position uncertainty is essential for effectively evaluating the performance of the navigation system under various conditions.

5.9.4 Optical Flow

As final remarks, optical flow techniques are indeed highly valuable for enhancing navigation systems, particularly in urban environments. Urban settings offer a wealth of features that can be detected and tracked by optical flow algorithms, making them well-suited for such scenarios. Additionally, one of

the key advantages of optical flow is the ability to provide velocity measurements at higher update rates than GPS. This can lead to significant improvements in estimation accuracy, especially in environments where GPS signals may be degraded or obstructed by buildings and other structures.

However, it should be noted that implementing optical flow algorithms often requires a dedicated companion computer to handle the vision processing tasks, separate from the main flight controller. While this may result in additional costs, the growing availability of low-cost solutions and extensive development in this area has made optical flow a more accessible and attractive option for enhancing navigation systems in urban environments.

5.9.5 Geomagnetic Positioning

Building geomagnetic maps for navigation in localized areas demands substantial effort and high-quality sensors to enhance the position estimation of any GAN method reliant on geomagnetic databases. A crucial aspect to consider is the noise inherent in the magnetic measurements, which translates into model uncertainty. Consequently, when maps are generated, they inherently carry this uncertainty, which could potentially introduce increased error in practical implementations.

As previously mentioned, the study involved several assumptions which, based on the team's experience with airborne navigation, can be challenging to maintain in urban environments. Key among these assumptions is the consistency and obtainability of magnetic signatures in outdoor areas close to man-made structures. In such environments, magnetic data can be significantly distorted, thereby affecting the quality and reliability of geomagnetic navigation. Additionally, it is assumed negligible magnetic field distortions due to the operation of the aircraft or vehicle itself. However, in practical scenarios, various onboard systems and operations can introduce significant magnetic noise, further complicating the task of accurate geomagnetic navigation.

Simultaneously, under the considerations established, the GAN algorithm is prone to drift in the absence of a reliable initial guess from the INS or EKF, and it requires accurate estimates of other states such as velocities or the position. These states will guide the course of observability because an incorrect hint can lead to the wrong path, even though it satisfies the magnetic matching conditions. The estimation can be misled by multiple points matching the magnetic measurement as illustrated in Figure 82. A precise velocity estimate will direct the correct path to follow as would be the case of the Optical Flow, whereas an inaccurate velocity estimate will result in severe drifting within the area.

This approach is not initially deemed suitable for urban environments until specific conditions are met. Key among these is the necessity for a meticulous magnetic calibration of the sensor, as well as the isolation of external magnetic sources from sensing objects, such as the motors in UAVs. This remains a significant concern for this type of development in long-range, high-altitude applications, and this concern can be extrapolated to smaller scenarios. Thus, while promising, the successful implementation of this approach in urban environments is contingent on meeting these stringent requirements.

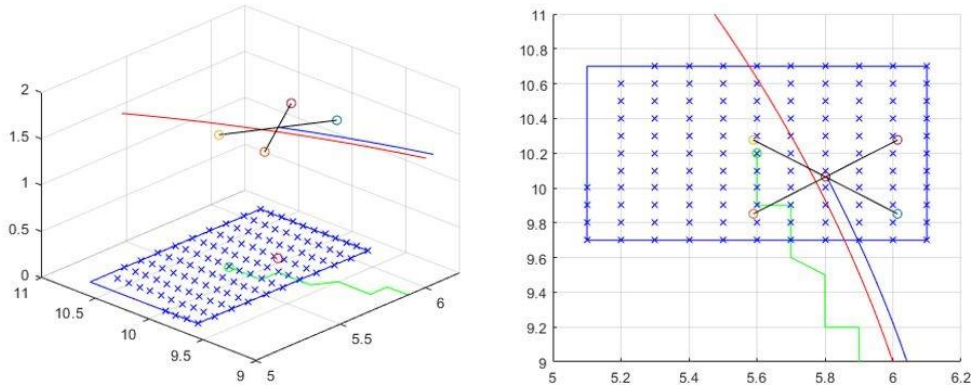

Figure 82. Flat Magnetic Area detected by the uncertainty area.

5.10 Conclusions

In this study, an initial approach rooted in position estimation from the nearest geomagnetic contour point and use of local features with optical tools are analyzed. T he importance of accurate velocity estimation is crucial, which can guide the GAN algorithm to a more specific exploration, particularly when navigating in magnetically flat regions devoid of detectable features.

Nevertheless, the geomagnetic matching algorithm serves as a corrective measure against the drift inherent in inertial navigation systems, although it doesn't provide position estimation itself. This highlights the need for an alternative position estimator, one that relies on sensor data beyond that of IMU components, as it is the Kalman filter included in the architecture.

Additionally, the Optical Flow techniques for enhancing navigation systems are highly valuable, especially in urban environments. These environments provide a wide set of features to be detected, and the high-rate velocity measurements from optical flow can significantly improve estimation accuracy.

Several challenges remain, including the impact of magnetic distortions in urban environments and the computational demands of high-resolution cameras in optical flow methods. Future work would focus on addressing these challenges and further refining the proposed algorithms for improved performance while simultaneously constantly improving the simulation environment proposed.

In conclusion, this report presents a comprehensive exploration and development of advanced methods aimed at enhancing autonomous navigation systems. The algorithms proposed and tested within this work have demonstrated significant promise in improving the accuracy and robustness of such systems, as evidenced by the results presented. Despite the successes achieved, it is recognized that there remains a considerable scope for further refinement and development. The complexities of real-world environments, particularly in urban settings, pose ongoing challenges that require innovative solutions. Nevertheless, the insights and knowledge gained from this work provide a solid foundation for future efforts in this field, and we remain confident in the potential of these methodologies to significantly advance autonomous navigation capabilities.

6 STANDARDS BODIES SUMMARY

As part of the ASSURE A44 Final Report, a list and synopsis of updates from several external organizations and working groups that were deemed important and pertinent to the FAA. Weight was placed on staying up to date with RTCA SC-228. Significant effort was done to review all SC-228 meeting minutes, phases of work, and all released and published documents for information applicable to this project. All other organizations, sub committees, and working groups have been investigated for applicability of previous, current, and upcoming work and deliverables. There have been very few updates since the initial RTCA and ASTM working group report delivered as part of the A44 literature review. RTCA document publications are generally behind schedule and the ASTM working groups are volunteer based and expected publications and updates are also behind schedule. Some of the areas reviewed are not directly associated with ADS-B and GPS, however their impact is related and therefore assessed on the potential impact on these systems.

6.1 RTCA SC-228 Detect and Avoid Standards

SC-228 of RTCA is meant to work closely with the UAS community to develop the Minimum operational Performance Standards (MOPS) for DAA equipment and the Performance Standards for the C2 Data Link. SC-228 deliverables include several performance standards documents which have been reviewed in their entirety for applicability to A44. All documents have a disclaimer mentioning applicability only to part 91 aircraft and operations and not part 107 small UAS. Only DO-365 and DO-381 specifically mentioned ADS-B and GPS.

DO-362A – Command and Control Data Link Minimum Operational Perf. Standards (MOPS)

The focus of this MOPS is the technical standards describing how CNPC Data Link Systems can compatibly share the spectrum that has been allocated for their use, yet remain waveform agnostic (i.e., unspecified). There are no interoperability requirements, as these are internal UAS interfaces. Rather, this MOPS provides required electromagnetic compatibility that permits simultaneous operation of federated designs in common spectrum.

DO-365A – MOPS for Detect and Avoid (DAA) Systems

The Detect and Avoid (DAA) system for Unmanned Aircraft Systems (UAS) flight was developed to assist the Pilot-in-Command (PIC) with his/her duties of operating an aircraft safely in the NAS.

All aircraft flying in the National Airspace System (NAS) must comply with the operating rules of Title 14 of the Code of Federal Regulations (14 CFR). Specifically, Part 91, §§.3, .111, .113(b), .115, .123 and .181(b), which address see and avoid, collision avoidance, and right-of-way rules. These operating regulations assumed that a pilot would be onboard the aircraft, so he/she would be able to exercise his/her authority to fully comply with these rules.

This document contains Phase 1 Minimum Operational Performance Standards (MOPS) for DAA systems used in aircraft transitioning to and from Class A or special use airspace (higher than 500’ Above Ground Level (AGL)), traversing Class D, E, and G airspace in the NAS. It does not apply to small UAS operating in low-level environments (below 500’) or

other segmented areas. Likewise, it does not apply to operations in the Visual Flight Rules (VFR) traffic pattern of an airport. DO-365 talks through ideal and safe performance standards that OEM's should meet for the safest and most efficient operations and walks through several con-ops that could apply to GPS/ADS-B DAA

DO-366A – MOPS for Air to Air Radar for Traffic Surveillance

This document contains the first update to the Minimum Operational Performance Standards (MOPS) for the air-to-air radar for traffic surveillance.

The intended application is supporting Detect and Avoid (DAA) operations including collision avoidance to detect intruders below 10,000' Mean Sea Level (MSL). These standards specify the radar system characteristics that should be useful for designers, manufacturers, installers and users of the equipment.

DO-377 – Minimum Aviation Safety Performance Standards (MASPS) for C2 link systems supporting operations of unmanned aircraft systems in US Airspace

This document contains the Minimum Aviation System Performance Standards (MASPS) for a C2 Link System connecting a Control Station (CS) and an Unmanned Aircraft (UA).

It covers UA operations requiring a C2 Link System that allows the UA to operate within line of sight (LOS) and beyond the line-of-sight (BLOS) of a Control Station. This MASPS contains the standards which specify system characteristics, i.e., it is design independent, that should be useful to UAS operators, Original Equipment Manufacturers 701 (OEM), and equipment manufacturers1 plus the FAA, as UAS operate within the U.S. airspace.

DO-381 – MOPS for Ground Based Surveillance System (GBSS) for Traffic Surveillance

This document contains MOPS for Ground Based Surveillance Systems (GBSS) used for air traffic surveillance in support of DAA operations for unmanned aircraft. The primary applications will be used in terminal, transit, or extended operational areas in the National Airspace System (NAS) as defined in RTCA Document 365A (DO 365A), Minimum Operational Performance Standards for Detect and Avoid Systems.

These standards specify the GBSS characteristics that should be useful for designers, manufacturers, installers and users of the equipment. Note that in this context, surveillance "systems" includes one or more networked non-cooperative sensors (e.g., radar and lidar), Electro-Optical/Infrared (EO/IR), etc.) needed to meet these MOPS.

DO-381 addresses several performance standards including but not limited to false track, latency, range, weather and environmental impacts and effect. DO-381 broadly applies to A44 but does not specifically match project scope or specific research tasks.

DO-397 – Guidance Material: Navigation Gaps for Unmanned Aircraft Systems (UAS)

This document is laying the initial groundwork to identify gaps in the navigation systems and standards that if filled may better support UAS operations. While all possible future UAS

operations is a very broad topic, to limit scope and provide near term focus, this document intentionally is focused on identifying navigation gaps associated with near term IFR and VFR-like planned path UAS operations for higher risk category fixed wing aircraft operating in and out of traditional airports.

DO-397 broadly applies to A44 but does not specifically match project scope or specific research tasks.

DO-398 – Operational Services and Environment Definition (OSED) for Unmanned Aircraft Systems Detect and Avoid Systems (DAA)

This document provides the Operational Services and Environment Description (OSED) for the SC-228 Unmanned Aircraft System (UAS) Detect and Avoid (DAA) Minimum Operational Performance Standards (MOPS). The purpose of this OSED is to provide a basis for assessing and establishing operational, safety, performance, and interoperability requirements for DAA systems, and outlines the use of DAA systems throughout the National Air Transportation System.

Although this document does describe the use of ADS-B as a DAA system, its focus is on but is quite broad and is focused on establishing requirements for systems and not about the systems themselves. It relates broadly to A44 scope and research tasks.

DO-400 – Guidance Material: Standardized Lost C2 Link Procedures for Uncrewed Aircraft Systems

This document provides guidance to stakeholders that could be affected by UAS operations that may encounter a Lost C2 Link (LC2L) while operating in the United States National Airspace System. Although worldwide UAS standards discussions identify a LC2L event as a rare event, standardized operating procedures to follow when/if this type of event occurs have yet to be established. This document is focused on UAS operations flying under an Instrument Flight Rules (IFR) flight plan and taxi operations on the airport movement areas. It has a near-term emphasis (within 4 years) and aligns with the International Civil Aviation Organization (ICAO) standards produced on LC2L procedures and the consequential amendments to ICAO Annexes and Procedures for Air Navigation Services documents.

6.2 RTCA SC-147 Traffic Alert and Collision Avoidance System

SC-147, since it was established in 1980, has produced and maintained minimum operational performance standards (MOPS) for Collision Avoidance Systems (CAS) and surveillance techniques required to meet desired levels of performance and safety. Since 2013, SC-147 has worked with EUROCAE WG75 to develop a new generation of collision avoidance systems called ACAS X. Recently, SC-147 has also worked closely with SC-228 on standards to ensure interoperability between all existing and future CAS and Detect and Avoid (DAA) systems (DO-382) and variants of ACAS X for Unmanned Aircraft Systems (UAS) and Vertical Take-off and Landing (VTOL) aircraft that are compliant and integrated with DAA standards published in versions of DO-365.

In December, 2020, SC-147 published the ACAS Xu MOPS (DO-386) which is a DAA/CA system for fully equipped (Transponder and ADS-B Out) aircraft flying in controlled airspace and receiving ATC services. DO-386 defines the minimum operational performance standards (Vol I) and Algorithm Design Descriptions (Vol II) for the Airborne Collision Avoidance System Xu (ACAS Xu) equipment, designed for platforms with a wide range of surveillance technologies and performance characteristics such as Unmanned Aircraft Systems (UAS).

In December of 2022, SC-147 published DO-396, Minimum Operational Performance Standards for Airborne Collision Avoidance System sXu (ACAS sXu). This document sets forth minimum operational performance standards for the Airborne Collision Avoidance System sXu (ACAS sXu) equipment, designed for platforms with a wide range of surveillance technologies and performance characteristics typical of smaller Unmanned Aircraft Systems (sUAS). Incorporated within these standards are system characteristics that should be of value to users, designers, manufacturers, and installers. These characteristics accommodate the requirements of various users.

Both DO-386 and DO-396 have direct applicability to A44 as GPS ADS-B data are used for collision avoidance.

6.3 RTCA SC-186 Automatic Dependent Surveillance Broadcast (ADS-B)

The purpose of SC-186 is to codify requirements based upon the airborne and ground user needs for an Automatic Dependent Surveillance-Broadcast (ADS-B) system. MOPS published by SC-186 are intended to be used by the FAA and other civil aviation authorities (CAA's) as an acceptable means of certifying ADS-B equipment for civil aircraft. Deliverables are intended to result in revised Technical Standard Orders for manufacturers of ADS-B equipment.

In 2009, SC-186 published DO-282B – MOPS for Universal Access Transceiver (UAT) Automatic Dependent Surveillance – Broadcast (ADS-B).

In 2022, SC-186 published DO-282C as an update to 282B. This document is similarly titled DO-282C "Minimum Operational Performance Standards for Universal Access Transceiver (UAT) Automatic Dependent Surveillance - Broadcast (ADS-B)" The document contains Minimum Operational Performance Standards for airborne equipment to support Automatic Dependent Surveillance - Broadcast utilizing the Universal Access Transceiver (UAT). UAT is a multi-purpose aeronautical data link intended to support not only ADS-B, but also Flight Information Service - Broadcast (FIS-B), and Traffic Information Service - Broadcast (TIS-B).

6.4 ASTM F38 working group updates

ASTM F38 WK16285 New Spec for Design and Performance of UAS Class 1320 – This working group is no longer posted on the ASTM website and no information can be found elsewhere. It is likely dissolved.

ASTM F38 WK27055 New Practice for UAS Remote ID – There is no mention of working group WK27055 on the ASTM website however, the document *Standard Specification for Remote ID and* Tracking has been published and was last updated July 2022. The document scope is as follows:

> This specification covers the performance requirements for remote identification (Remote ID) of unmanned aircraft systems (UAS). Remote ID allows governmental and civil identification of UAS for safety, security, and compliance purposes. The objective is to increase UAS remote pilot accountability by removing anonymity while preserving operational privacy for remote pilots, businesses, and their customers. Remote ID is an enabler of enhanced operations such as beyond visual line of sight (BVLOS) operations as well as operations over people.
>
> This specification defines message formats, transmission methods, and minimum performance standards for two forms of Remote ID: broadcast and network. Broadcast Remote ID is based on the transmission of radio signals directly from a UAS to receivers in the UAS's vicinity. Network Remote ID is based on communication by means of the internet from a network Remote ID service provider (Net-RID SP) that interfaces directly or indirectly with the UAS, or with other sources in the case of intent-based network participants.
>
> This specification addresses the communications and test requirements of broadcast or network Remote ID, or both, in UAS and Net-RID SP systems.
>
> This specification is applicable to UAS that operate at very low level (VLL) airspace over diverse environments including but not limited to rural, urban, networked, network degraded, and network denied environments, regardless of airspace class.
>
> This specification neither purports to address UAS operating with approval to use ADS-B or secondary surveillance radar transponders, nor does it purport to solve ID needs of UAS for all operations.
>
> In particular, this specification does not purport to address identification needs for UAS that are not participating in Remote ID or operators that purposefully circumvent Remote ID.
>
> The values stated in SI units are to be regarded as standard. The values given in parentheses after SI units are provided for information only and are not considered standard.

ASTM F38 WK53964 Design, Construct, and Test of VTOL - This working group is no longer posted on the ASTM website and no information can be found elsewhere. It is likely dissolved.

ASTM F38 WK62670 New Standard Large UAS Design and Construction - This working group is no longer posted on the ASTM website and no information can be found elsewhere. It is likely dissolved.

ASTM F38 WK62668 Detect and Avoid Performance Requirements – There is no mention of working group 62668 by ASTM however, the *Standard Specification for Detect and Avoid System Performance Requirements* document is available and last updated February of 2023. This working group document has broad applicability to A44 and its research tasks. The scope of the document is as follows:

> This specification applies to uncrewed aircraft (UA) with a maximum dimension (for example, wingspan, disc diameter) ≤25 ft, operating at airspeeds below 100 kts, and of any configuration

or category. It is meant to be applied in a “lower risk” [low- and medium-risk airspace as described by Joint Authorities for Rulemaking on Unmanned Systems (JARUS)] airspace environment with assumed infrequent encounters with crewed aircraft; this is typically in classes G and E airspace [below about 1200 ft above ground level (AGL)], Class B, C, D (below approximately 400 ft to 500 ft AGL) below obstacle clearance surface (FAA Order 8260.3, as amended) or within low altitude authorization and notification capability (LAANC) designated areas below the altitude specified in the facility map.

> Traffic encountered is expected to be mixed cooperative and non-cooperative traffic, instrument flight rules (IFR) and visual flight rules (VFR), and to mostly include low-altitude aircraft—including rotorcraft, small general aviation, crop dusters, ultralights, and light sport aircraft, but not transport category aircraft.
>
> This includes, but is not limited to, airspace where nearly all aircraft are required2 to be cooperative (for example, within the Mode C veil in the United States).

Ultimate determination of applicability will be governed by the appropriate civil aviation authority (CAA).

This specification assumes no air traffic control (ATC) separation services are provided to the UA.

While some architectures may have limitations due to external conditions, this specification applies to daytime and nighttime, as well as visual meteorological conditions (VMC) and instrument meteorological conditions (IMC). The system integrator shall document system limitation (that is, due to operating environments and/or minimum altitudes at which the air picture is no longer valid).

This specification is applicable to the avoidance of crewed aircraft by uncrewed aircraft systems (UAS), not UA-to-UA or terrain/obstacle/airspace avoidance (both to be addressed in future efforts). Likewise, birds or natural hazard (for example, weather, clouds) avoidance requirements are not addressed.

This specification does not define a specific detect and avoid (DAA) architecture and is architecture agnostic. It will, however, define specific safety performance thresholds for a DAA system to meet in order to ensure safe operation.

This specification addresses the definitions and methods for demonstrating compliance to this specification, and the many considerations (for example, detection range, required timeline to meet well clear, and near mid-air collision (NMAC) safety targets) affecting DAA system integration.

The specification highlights how different aspects of the system are designed and interrelated, and how they affect the greater UAS system-of-systems to enable a developer to make informed decisions within the context of their specific UAS application(s).

> It is expected this specification will be used by diverse contributors or actors including, but not limited to DAA system designers and integrators, sensor suppliers, UA developers, control station designers, UAS service suppliers, and flight control designers.
>
> Except for DAA system integrators for whom all the "shalls" in this specification apply, not all aspects of this specification are relevant to all actors/contributors. In some instances, the actor most likely to satisfy a requirement has been identified in brackets after the requirement; this is for informative purposes only and does not indicate that only that actor may fulfill that requirement. Where not specified, the system integrator/applicant is assumed to be the primary actor; in all cases, the system integrator/applicant is responsible for all requirements and may choose to delegate requirements as is suitable to the system design. Nonetheless, familiarity with the entire specification will inform all actors/contributors of how their contributions affect the overall DAA capability and is strongly recommended.
>
> The values stated in either SI units or inch-pound units are to be regarded separately as standard. The values stated in each system are not necessarily exact equivalents; therefore, to ensure conformance with the standard, each system shall be used independently of the other, and values from the two systems shall not be combined.
>
> This standard does not purport to address all of the safety concerns, if any, associated with its use. It is the responsibility of the user of this standard to establish appropriate safety, health, and environmental practices and determine the applicability of regulatory limitations prior to use.
>
> This international standard was developed in accordance with internationally recognized principles on standardization established in the Decision on Principles for the Development of International Standards, Guides and Recommendations issued by the World Trade Organization Technical Barriers to Trade (TBT) Committee.

ASTM F38 WK62669 Detect and Avoid Test Methods – This working group is very active and will soon be releasing a document defining test methods for DAA systems and sensors applicable to smaller UAS BVLOS operations for the protection of manned aircraft in lower altitude airspace. The publish date is not yet known but is expected within the next 6 months.

ASTM F38 WK28019 New Practice for selecting sUAS Launch and Recovery - This working group is no longer posted on the ASTM website and no information can be found elsewhere. It is likely dissolved.

ASTM F38 WK59317 Vertiport Design – There is no mention of working group 59317 by ASTM however, the *Standard Specification for Vertiport Design* has been published and was last updated August of 2022. The scope of the document is as follows:

> This specification defines the requirements for the planning, design, and establishment of vertiports intended to service vertical takeoff and landing (VTOL) aircraft. These aircraft include, but are not limited to, standard category aircraft, optionally piloted aircraft, and unmanned aircraft. Aircraft not covered by this specification include VTOL aircraft less than 55 lb [25 kg]. In developing these standards, identified types of eVTOL aircraft, for example, Multi-Rotor, Lift

& Cruise, Vectored Thrust, Tilt Wing, Tilt Rotor, etc., were considered. Ultimately it is up to the authorities having jurisdiction (AHJ) as to how and to what extent these standards are applied. Vertiports may provide commercial or private services in support of the operation of eVTOL aircraft including, but not limited to, some or all of occupant and cargo transport, air medical, flight instruction, aerial work, aircraft rental, fueling, charging of energy storage devices, battery exchange, hangaring, and maintenance services.

This specification is intended to support the design of civil vertiports and vertistops, however, it may also be used as a best practice document for other facilities.

Vertiport is a generic reference to the area of land, water, or structure used, or intended to be used, for the landing and takeoff of VTOL aircraft, together with associated buildings and facilities. At this time, aircraft with floats conducting water landings and takeoffs are not included in this specification.

Vertistop - The same as Vertiport, except that no fueling, defueling, scheduled maintenance, scheduled repairs, or storage of aircraft is permitted. Unscheduled maintenance and repairs to return an aircraft in an AOG (Aircraft on Ground) status to a serviceable status are permissible.

This document may present information in either SI units, English Engineering units, or both. The values stated in each system are not necessarily exact equivalents; therefore, to ensure conformance with the standard, each system shall be used independently of the other, and values from the two systems shall not be combined.

This standard does not purport to address all of the safety concerns, if any, associated with its use. It is the responsibility of the user of this standard to establish appropriate safety, health, and environmental practices and determine the applicability of regulatory limitations prior to use.

This international standard was developed in accordance with internationally recognized principles on standardization established in the Decision on Principles for the Development of International Standards, Guides and Recommendations issued by the World Trade Organization Technical Barriers to Trade (TBT) Committee.

ASTM F38 WK63418 Service Provided under UAS Traffic Management (UTM) - This working group is no longer posted on the ASTM website and no information can be found elsewhere. It is likely dissolved.

ASTM F38 WK62344 BVLOS Package Delivery sUAS Operations - This working group is no longer posted on the ASTM website and no information can be found elsewhere. It is likely dissolved.

ASTM F38 WK11425 New Practice for Private UAS Pilot Practical Test Standards for UAS - This working group is no longer posted on the ASTM website and no information can be found elsewhere. It is likely dissolved.

ASTM F38 WK62730 UAS Operator Audit Programs – There is no mention of working group 62730 on the ASTM website, however a document was published in 2019 titled *Standard practice for Independent Audit Program for Unmanned Aircraft Operators*. The document has seen no updates since its publishing and is likely not beneficial to A44.

ASTM F38 WK62733 Training and Development of Training Manuals for UAS Operator – This working group published *Standard specification for Training and the Development of Training Manuals for the UAS Operator* in February 2023. The scope of the document is as follows:

> This specification defines the requirements for training and the development of training manuals for the unmanned aircraft systems (UAS) operator.
>
> The specification addresses the requirements or best practices, or both, for documentation and organization of a professional operator (that is, for compensation and hire) for the purposes of internal training programs and for programs offered to the general public.
>
> This specification supports professional entities that will receive operator certification by a CAA, and provide standards of practice for self- or third-party audit of operators of UAS.
>
> The standard case study used to develop this specification focused on operators of light UAS (below 1320 lb/600 kg as defined by EASA), but the specification may be applied to larger aircraft for using other methods of classification (that is, risk based classes and pilot privileges classes).
>
> Training manuals that do not include all the minimum requirements of this specification may not be referred to as meeting this specification.
>
> The values stated in inch-pound units are to be regarded as standard. The values given in parentheses are mathematical conversions to SI units that are provided for information only and are not considered standard.
>
> This standard does not purport to address all of the safety concerns, if any, associated with its use. It is the responsibility of the user of this standard to establish appropriate safety, health, and environmental practices and determine the applicability of regulatory limitations prior to use.
>
> This international standard was developed in accordance with internationally recognized principles on standardization established in the Decision on Principles for the Development of International Standards, Guides and Recommendations issued by the World Trade Organization Technical Barriers to Trade (TBT) Committee.

ASTM F38 WK63407 Required Product Information to be provided with an sUAS - No data can be found on this working group from the ASTM website, but this is due to a website error. This will be updated as soon as possible.

ASTM F38 WK69690 Surveillance UTM Supplemental Data Service Provider (SDSP) - No data can be found on this working group from the ASTM website, but this is due to a website error. This will be updated as soon as possible.

7 SUMMARY

The A44 team has completed the testing, analysis, and demonstration of mitigations report and has made final recommendations which fulfills Task 5 for the A44 ASSURE project. The integrity of ADS-B and GPS navigation systems were tested to detect threats to the integrity and/or reliability of the data. These risks include dropped, erroneous, spoofed, and jammed data from GPS and/or ADS-B systems. Several mitigation schemes were flight and simulation tested based on their potential effectiveness in jamming and spoofing conditions. The mitigation schemes tested are cellular signal navigation, the Eichelberger's Collective Detection (ECD) method, optical flow, and geomagnetic navigation.

In Chapter 2 UAS anomalies were studied using ADS-B data sets to identify ADS-B anomalies that would result in enhanced risk in flight operations. Efforts were also made to identify the scenarios that are most common and provide plausible reasons for the events. The data analyzed was collected by using flight test operations at UAF as well as from a unique case study of public use ADS-B data from the Dallas Fort Worth airport. In both cases there are events that lead to enhanced risk in flight operation if only ADS-B is used. To reduce these risks, additional metrics were recommended for ADS-B reception quality and the distance and altitudes of the ADS-B receiver and transmitting aircraft. The DFW case clearly illustrated the possibility of extended loss of ADS-B signals and the subsequent need for mitigation strategies. Initial studies regarding introducing path planning were presented to illustrate the effectiveness and ability of the technique.

In Chapter 3 the effectiveness of cellular navigation techniques was studied. Flight tests were developed to record and utilize nearby LTE/4G cellular signals to inform a GNSS-independent positioning solution from a UAS-based receiver. The findings show precise cellular signal positioning approaches have strong potential for mitigating risk in UAS operations and should be considered a supporting navigation aide. The primary considerations for this conclusion include (1) the published potential for meter to submeter accuracy in time-of-arrival approaches, (2) practicality and plausibility of cellular receiver utilization in current and future UAS hardware, (3) the signal coverage of typical UAS operation flight space currently available from existing cellular infrastructure, and (4) future potential for cellular positioning in challenging urban environments in lieu of 'smart cities', possible dense 5G communication networks.

Chapter 4 focused on the ECD method in a simulation environment to produce preliminary data to assess its effectiveness. The research efforts have uncovered some of the viability and unique capabilities of ECD to detect spoofed signals, mitigate the false and true signals, and recover the true signals. A preliminary GPS simulation model has been created as an initial step in establishing ECD validity. The research and simulation activities were fully completed due to the scope of work required, but the team has not lost faith or interest in the ECD counter-spoofing technology. The viability and power of ECD to do three things that other countermeasure technologies cannot do in

entirety: (1) Detect spoofed communication/navigation signals; (2) Use ECD to mitigate the false and true signals; and (3) Recover the true signals in all the risk conditions. To produce a fully functional GPS simulation model there needs further modifications to explicitly prove the ECD validity.

In Chapter 5 the evaluation of the capabilities, advantages, and limitations of optical flow and geomagnetic navigation techniques were made using both flight and simulated data. These algorithms have demonstrated significant potential in improving the accuracy and robustness of navigation systems. In the geomagnetic navigation study, an initial approach rooted in position estimation from the nearest geomagnetic contour point and use of local features with optical tools were analyzed. It was shown that the geomagnetic matching algorithm serves as a corrective measure against the drift inherent in inertial navigation systems, although it doesn't provide position estimation itself. The optical flow techniques for enhancing navigation systems were shown to be highly valuable, especially in urban environments. These environments provide a wide set of features to be detected, and the high-rate velocity measurements from optical flow can significantly improve estimation accuracy. The algorithms proposed and tested within this chapter have demonstrated significant promise in improving the accuracy and robustness of such systems.

The A44 team Task 5 Final Report provides in-depth studies of several navigational mitigation techniques and events that help better inform the FAA and standards bodies detailed information to create appropriate regulations and operational guidelines. Task 1-4 Reports are provided in the appendices to provide additional details of the studies done in support of the final report findings.

8. REFERENCES

A. Cuenca, and H. Moncayo. 2023. “Performance Analysis of UAV Control Architectures Over Urban Environments with Degraded GNSS Accessibility.” In . IEEE/ION PLANS. https://www.ion.org/plans/abstracts.cfm?paperID=12020.

Abdallah, Ali A., and Zaher M. Kassas. 2021. “UAV Navigation With 5G Carrier Phase Measurements.” In , 3294–3306. https://doi.org/10.33012/2021.18101.

“Absolute Postioning Using the Earth’s Magnetic Anomaly Field - ProQuest.” n.d. Accessed May 22, 2023. https://www.proquest.com/docview/1845857381?pq-origsite=gscholar&fromopenview=true.

Alexeev, I I, S Yu Bobrovnikov, V V Kalegaev, Yu G Lyutov, M I Panasyuk, and J M Quinn. n.d. “Space System - Space Environment (Natural and Artificial) Model of Earth’s Magnetospheric Magnetic Field.”

Ali, Busyairah Syd, Washington Ochieng, Arnab Majumdar, Wolfgang Schuster, and Thiam Kian Chiew. 2014. “ADS-B System Failure Modes and Models.” *The Journal of Navigation* 67 (6): 995–1017.

Ali, Busyairah Syd, Washington Yotto Ochieng, and Rozaimah Zainudin. 2017. “An Analysis and Model for Automatic Dependent Surveillance Broadcast (ADS-B) Continuity.” *GPS Solutions* 21 (4): 1841–54. https://doi.org/10.1007/s10291-017-0657-y.

Alken, P., E. Thébault, C. D. Beggan, H. Amit, J. Aubert, J. Baerenzung, T. N. Bondar, et al. 2021. “International Geomagnetic Reference Field: The Thirteenth Generation.” *Earth, Planets and Space* 73 (1): 49. https://doi.org/10.1186/s40623-020-01288-x.

Andert, Franz, Nikolaus Ammann, Jan Puschel, and Jorg Dittrich. 2014. “On the Safe Navigation Problem for Unmanned Aircraft: Visual Odometry and Alignment Optimizations for UAV Positioning.” *2014 International Conference on Unmanned Aircraft Systems, ICUAS 2014 - Conference Proceedings*, 734–43. https://doi.org/10.1109/ICUAS.2014.6842318.

Arteaga, Ricardo A., Kraettli Epperson, Mohammed Dandachy, Arun Aruljothi, Hong Truong, and Mihir Vedantam. 2018. “MADS-B Detect and Avoid Flight Tests on Phantom 4 Unmanned Aircraft System.” In *2018 AIAA Information Systems-AIAA Infotech@ Aerospace*, 2014.

Beauchemin, S. S., and J. L. Barron. 1995. “The Computation of Optical Flow.” *ACM Computing Surveys* 27 (3): 433–66. https://doi.org/10.1145/212094.212141.

Berry, Joseph K. 2007. “Map Analysis: Understanding Spatial Patterns and Relationships.”

Bi, Yingcai, Menglu Lan, Jiaxin Li, Shupeng Lai, and Ben M. Chen. 2019. “A Lightweight Autonomous MAV for Indoor Search and Rescue.” *Asian Journal of Control* 21 (4): 1732–44. https://doi.org/10.1002/asjc.2162.

Blakely, Richard J. 1996. *Potential Theory in Gravity and Magnetic Applications*. Cambridge University Press.

Butcher, Eric A. 2019. “Analytical Mechanics of Space Systems: Fourth Edition [Bookshelf].” *IEEE Control Systems* 39 (5): 110–11. https://doi.org/10.1109/MCS.2019.2925258.

Cai, Guowei, Jorge Dias, and Lakmal Seneviratne. 2014. “A Survey of Small-Scale Unmanned Aerial Vehicles: Recent Advances and Future Development Trends.” *Unmanned Systems* 2 (2): 175–99. https://doi.org/10.1142/S2301385014300017.

Canciani, Aaron, and John Raquet. 2016. “Absolute Positioning Using the Earth’s Magnetic Anomaly Field.” *NAVIGATION* 63 (2): 111–26. https://doi.org/10.1002/navi.138.

Chang, Liu. 2017. “Progress, Contribution and Challenges of Earth-Magnetism Navigation.” *Automation, Control and Intelligent Systems* 5 (1): 8. https://doi.org/10.11648/j.acis.20170501.12.

Chao, Haiyang, Yu Gu, and Marcello Napolitano. 2013. “A Survey of Optical Flow Techniques for UAV Navigation Applications.” In *2013 International Conference on Unmanned Aircraft Systems (ICUAS)*, 710–16. Atlanta, GA, USA: IEEE. https://doi.org/10.1109/ICUAS.2013.6564752.

———. 2014. “A Survey of Optical Flow Techniques for Robotics Navigation Applications.” *Journal of Intelligent & Robotic Systems* 73 (1): 361–72. https://doi.org/10.1007/s10846-013-9923-6.

Corporation, The Analytic Sciences. 1974. *Applied Optimal Estimation*. MIT Press.

Couturier, Andy, and Moulay Akhloufi. 2020. “Conditional Probabilistic Relative Visual Localization for Unmanned Aerial Vehicles.” *Canadian Conference on Electrical and Computer Engineering* 2020-Augus. https://doi.org/10.1109/CCECE47787.2020.9255691.

Cuenca, Andrei, and Hever Moncayo. 2021a. “A Geomagnetic-Based Integrated Architecture for Dead-Reckoning Navigation.” In *AIAA Scitech 2021 Forum*. AIAA SciTech Forum. American Institute of Aeronautics and Astronautics. https://doi.org/10.2514/6.2021-1227.

———. 2021b. “Machine Learning Application to Estimation of Magnetospheric Contributions for Geomagnetic-Based Navigation.” In *AIAA SCITECH 2022 Forum*. AIAA SciTech Forum. American Institute of Aeronautics and Astronautics. https://doi.org/10.2514/6.2022-1714.

———. 2023. “Geomagnetic Aided Navigation Using Rao Blackwellized Particle Filter.” In . https://doi.org/10.2514/6.2023-1452.

Cui, Jin Q., Shupeng Lai, Xiangxu Dong, and Ben M. Chen. 2016. “Autonomous Navigation of UAV in Foliage Environment.” *Journal of Intelligent & Robotic Systems* 84 (1): 259–76.

Davis, Jeremy. 2004. “Mathematical Modeling of Earth’s Magnetic Field,” May.

Duan, Xiusheng, Jing Xiao, Xiaohui Qi, and Yifei Liu. 2019. “An INS/Geomagnetic Integrated Navigation Algorithm Based on Matching Strategy and Hierarchical Filtering.” *Electronics* 8 (4): 460. https://doi.org/10.3390/electronics8040460.

El-Rewini, Zeinab, Karthikeyan Sadatsharan, Niroop Sugunaraj, Daisy Flora Selvaraj, Siby Jose Plathottam, and Prakash Ranganathan. 2020. “Cybersecurity Attacks in Vehicular Sensors.” *IEEE Sensors Journal* 20 (22): 13752–67. https://doi.org/10.1109/JSEN.2020.3004275.

G. Bradski. 2000. “Dr. Dobb’s Journal of Software Tools.” November 2000. https://ftp.math.utah.edu/pub/tex/bib/toc/dr-dobbs-2000.html#25(11):November:2000.

Gageik, Nils, Michael Strohmeier, and Sergio Montenegro. 2013. “An Autonomous UAV with an Optical Flow Sensor for Positioning and Navigation.” *International Journal of Advanced Robotic Systems* 10 (10): 341. https://doi.org/10.5772/56813.

Garcia, Jorge Reyes. n.d. “Minimum Aviation System Performance Standards For Automatic Dependent Surveillance Broadcast (ADS-B.” Accessed July 6, 2023. https://www.academia.edu/8996706/Minimum_Aviation_System_Performance_Standards_For_Automatic_Dependent_Surveillance_Broadcast_ADS_B.

Garg, Sahil, Gagangeet Singh Aujla, Neeraj Kumar, and Shalini Batra. 2019. “Tree-Based Attack–Defense Model for Risk Assessment in Multi-UAV Networks.” *IEEE Consumer Electronics Magazine* 8 (6): 35–41.

Gebre-Egziabher, Demoz, and Brian Taylor. 2012. “Impact and Mitigation of GPS-Unavailability on Small UAV Navigation, Guidance and Control, Univ. of MN UAV Laboratory.” *Dep’t of Aerospace Eng. & Mech*.

Goforth, Hunter, and Simon Lucey. 2019. “GPS-Denied UAV Localization Using Pre-Existing Satellite Imagery.” In *2019 International Conference on Robotics and Automation (ICRA)*, 2974–80. IEEE.

Goldenberg, Felix. 2006. “Geomagnetic Navigation beyond the Magnetic Compass.” In , 684–94. http://www.ion.org/publications/abstract.cfm?jp=p&articleID=6702.

GPS.GOV. 2021. “Space Segment.” Systems. 2021. https://www.gps.gov/systems/gps/space/.

Gubbins, David. 2010. “Terrestrial Magnetism: Historical Perspectives and Future Prospects: ‘Baggage We Carry with Us.’” *Space Science Reviews* 155 (1–4): 9–27. https://doi.org/10.1007/s11214-010-9675-6.

Gudla, Charan, Md Shohel Rana, and Andrew H Sung. 2018. “Defense Techniques against Cyber Attacks on Unmanned Aerial Vehicles.” *Proceedings of the International Conference on Embedded Systems, Cyber-Physical Systems, and Applications (ESCS)*, 110–16.

Gupta, Lav, Raj Jain, and Gabor Vaszkun. 2016. “Survey of Important Issues in UAV Communication Networks.” *IEEE Communications Surveys and Tutorials* 18 (2): 1123–52.

Gustavsson, Kenneth. 2015. *UAV Pose Estimation Using Sensor Fusion of Inertial, Sonar and Satellite Signals*. https://urn.kb.se/resolve?urn=urn:nbn:se:uu:diva-256872.

Harris, C., and M. Stephens. 1988. “A Combined Corner and Edge Detector.” In *Procedings of the Alvey Vision Conference 1988*, 23.1-23.6. Manchester: Alvey Vision Club. https://doi.org/10.5244/C.2.23.

Hartmann, Kim, and Christoph Steup. 2013. “The Vulnerability of UAVs to Cyber Attacks - An Approach to the Risk Assessment.” *International Conference on Cyber Conflict, CYCON*.

Hentati, Aicha Idriss, and Lamia Chaari Fourati. 2020. “Comprehensive Survey of UAVs Communication Networks.” *Computer Standards and Interfaces* 72 (June): 103451. https://doi.org/10.1016/j.csi.2020.103451.

Higuchi, Kenichi, and Anass Benjebbour. 2015. “Non-Orthogonal Multiple Access (NOMA) with Successive Interference Cancellation for Future Radio Access.” *IEICE Transactions on Communications* E98B (3): 403–14. https://doi.org/10.1587/transcom.E98.B.403.

Horri, Nadjim, and Phil Palmer. 2013. “Relative Navigation.” *Distributed Space Missions for Earth System Monitoring*, no. August: 331–44. https://doi.org/10.1007/978-1-4614-4541-8_9.

Isaacs, Jason T., Ceridwen Magee, Anantharaman Subbaraman, François Quitin, Kingsley Fregene, Andrew R. Teel, Upamanyu Madhow, and João P. Hespanha. 2014. “GPS-Optimal Micro Air Vehicle Navigation in Degraded Environments.” *Proceedings of the American Control Conference*, 1864–71. https://doi.org/10.1109/ACC.2014.6859336.

Jacobs, J. A. 1985. “The Earth’s Magnetic Field: Its History, Origin and Planetary Perspective. By R. T. MERRILL and M. W. McELHINNY. Academic, 1983. 401 Pp. £39.50 Hb, £17.50 Pb.” *Journal of Fluid Mechanics* 156 (July): 532–33. https://doi.org/10.1017/S0022112085212233.

Khalife, Joe J., Souradeep Bhattacharya, and Zak M. Kassas. 2018. “Centimeter-Accurate UAV Navigation With Cellular Signals.” In , 2321–31. https://doi.org/10.33012/2018.16105.

Khalife, Joe, Kimia Shamaei, and Zaher M. Kassas. 2016. “A Software-Defined Receiver Architecture for Cellular CDMA-Based Navigation.” In *2016 IEEE/ION Position, Location and Navigation Symposium (PLANS)*, 816–26. https://doi.org/10.1109/PLANS.2016.7479777.

Kintner, P. M., B. M. Ledvina, and E. R. De Paula. 2007. “GPS and Ionospheric Scintillations.” *Space Weather* 5 (9): 1–23. https://doi.org/10.1029/2006SW000260.

Kissai, Ali, and Milton Smith. 2019. “UAV Dead Reckoning with and without Using INS/GPS Integrated System in GPS Denied Polar Regions.” *International Journal of Aeronautics and Aerospace Engineering* 1 (2): 58–67. https://doi.org/10.18689/ijae-1000109.

Lagkas, Thomas, Vasileios Argyriou, Stamatia Bibi, and Panagiotis Sarigiannidis. 2018. “UAV IoT Framework Views and Challenges: Towards Protecting Drones as ‘Things.’” *Sensors* 18 (11): 4015.

Langlais, K. n.d. “The New Digital Magnetic Anomaly Database and Map of North America.” Accessed May 22, 2023. https://pubs.usgs.gov/of/2002/ofr-02-414/.

Leela Krishna, C. G., and Robin Murphy. 2018. “A Review on Cybersecurity Vulnerabilities for Unmanned Aerial Vehicles.” *Auvsi Xponential 2018*, 0–5.

Li, Li, Kangye Qu, and Kuo-Yi Lin. 2020. “A Survey on Attack Resilient of UAV Motion Planning.” In *2020 IEEE 16th International Conference on Control & Automation (ICCA)*, 558–63. IEEE.

Liu, Ying, Meiping Wu, Xiaoping Hu, and Hongwei Xie. 2008. “Geomagnetism Aided Inertial Navigation System.” In *2008 2nd International Symposium on Systems and Control in Aerospace and Astronautics*, 1–5. https://doi.org/10.1109/ISSCAA.2008.4776291.

Liu, Yuanwei, Zhijin Qin, Yunlong Cai, Yue Gao, Geoffrey Ye Li, and Arumugam Nallanathan. 2019. “UAV Communications Based on Non-Orthogonal Multiple Access.” *IEEE Wireless Communications* 26 (1): 52–57. https://doi.org/10.1109/MWC.2018.1800196.

Lowrie, William, and Andreas Fichtner. 2020. *Fundamentals of Geophysics*. Cambridge University Press.

Ly, Bora, and Romny Ly. 2021. “Cybersecurity in Unmanned Aerial Vehicles (UAVs).” *Journal of Cyber Security Technology* 5 (2): 120–37. https://doi.org/10.1080/23742917.2020.1846307.

M. J. Kochenderfer, J. P. Chryssanthacopoulos, L. P. Kaelbling, and T. Lozano-P´erez. n.d. “Model-Based Optimization of Airborne Collision Avoidance Logic | MIT Lincoln Laboratory.” Accessed May 21, 2023. https://www.ll.mit.edu/r-d/publications/model-based-optimization-airborne-collision-avoidance-logic.

Matolak, David W. 2015. “Unmanned Aerial Vehicles: Communications Challenges and Future Aerial Networking.” *2015 International Conference on Computing, Networking and Communications, ICNC 2015*, 567–72. https://doi.org/10.1109/ICCNC.2015.7069407.

Maus, S., T. Sazonova, K. Hemant, J. D. Fairhead, and Dhananjay Ravat. 2007. “National Geophysical Data Center Candidate for the World Digital Magnetic Anomaly Map.” *Geochemistry, Geophysics, Geosystems* 8 (6). https://doi.org/10.1029/2007GC001643.

Mellinger, Daniel, Nathan Michael, and Vijay Kumar. 2014. “Trajectory Generation and Control for Precise Aggressive Maneuvers with Quadrotors.” In *Experimental Robotics*, edited by

Oussama Khatib, Vijay Kumar, and Gaurav Sukhatme, 79:361–73. Springer Tracts in Advanced Robotics. Berlin, Heidelberg: Springer Berlin Heidelberg. https://doi.org/10.1007/978-3-642-28572-1_25.

Morales, Joshua J., and Zaher M. Kassas. 2021. "Tightly Coupled Inertial Navigation System With Signals of Opportunity Aiding." *IEEE Transactions on Aerospace and Electronic Systems* 57 (3): 1930–48.

Nahangi, Mohammad, Adam Heins, Brenda McCabe, and Angela Schoellig. 2018. "Automated Localization of UAVs in GPS-Denied Indoor Construction Environments Using Fiducial Markers." *ISARC 2018 - 35th International Symposium on Automation and Robotics in Construction and International AEC/FM Hackathon: The Future of Building Things*, no. Isarc. https://doi.org/10.22260/isarc2018/0012.

National Institute of Standards and Technology (NIST). 2004. "Standards for Security Categorization of Federal Information and Information Systems." *Federal Information Processing Standards Publication (FIPS PUB 199)*, no. February: 473–84. https://doi.org/10.1016/b978-159749116-7/50032-9.

Parrot. 2021. "Parrot ANAFI Ai | The 4G Robotic UAV." Parrot. 2021. https://www.parrot.com/us/drones/anafi-ai.

Pei, Yanliang, Baohua Liu, Qingfeng Hua, Chenguang Liu, and Yuqiang Ji. 2017. "An Aeromagnetic Survey System Based on an Unmanned Autonomous Helicopter: Development, Experiment, and Analysis." *International Journal of Remote Sensing* 38 (8–10): 3068–83. https://doi.org/10.1080/01431161.2016.1274448.

Peral-Rosado, Jose A. del, Jose A. Lopez-Salcedo, Gonzalo Seco-Granados, Francesca Zanier, Paolo Crosta, Rigas Ioannides, and Massimo Crisci. 2013. "Software-Defined Radio LTE Positioning Receiver Towards Future Hybrid Localization Systems." In *31st AIAA International Communications Satellite Systems Conference*. International Communications Satellite Systems Conferences (ICSSC). American Institute of Aeronautics and Astronautics. https://doi.org/10.2514/6.2013-5610.

Potemra, Thomas A. 1984. *Magnetospheric Currents*. *Magnetospheric Currents. Potemra*. Vol. 28. https://doi.org/10.1029/GM028.

Program, Air Force, and Air Force Program. 2012. "Global Positioning System (GPS) Selective Availability Anti-Spoofing Module (SAASM)." *Gps Saasm*, 227–28.

Qualcomm. 2022. "Qualcomm Unleashes a New Era of Autonomous Drone Capabilities with World's First 5G and AI-Enabled Drone Platform." 2022. https://www.qualcomm.com/news/releases/2021/08/qualcomm-unleashes-new-era-autonomous-drone-capabilities-worlds-first-5g.

R. Hartley, and A. Zisserman. 2003. "Multiple View Geometry in Computer Vision." *Cambridge University Press*.

Riahi Manesh, Mohsen, and Naima Kaabouch. 2017. "Analysis of Vulnerabilities, Attacks, Countermeasures and Overall Risk of the Automatic Dependent Surveillance-Broadcast (ADS-B) System." *International Journal of Critical Infrastructure Protection* 19 (December): 16–31. https://doi.org/10.1016/j.ijcip.2017.10.002.

"Robust Waypoints Navigation Using Fuzzy Type 2 Controller | IEEE Conference Publication | IEEE Xplore." n.d. Accessed May 21, 2023. https://ieeexplore.ieee.org/document/9015101.

Sabaka, Terence J., Nils Olsen, and Robert A. Langel. 2002. “A Comprehensive Model of the Quiet-Time, near-Earth Magnetic Field: Phase 3.” *Geophysical Journal International* 151 (1): 32–68. https://doi.org/10.1046/j.1365-246X.2002.01774.x.

Sabaka, Terence J., Nils Olsen, Robert H. Tyler, and Alexey Kuvshinov. 2015. “CM5, a Pre-Swarm Comprehensive Geomagnetic Field Model Derived from over 12 Yr of CHAMP, Ørsted, SAC-C and Observatory Data.” *Geophysical Journal International* 200 (3): 1596–1626. https://doi.org/10.1093/gji/ggu493.

Sahawneh, Laith R., Matthew O. Duffield, Randal W. Beard, and Timothy W. McLain. 2015. “Detect and Avoid for Small Unmanned Aircraft Systems Using ADS-B.” *Air Traffic Control Quarterly* 23 (2–3): 203–40. https://doi.org/10.2514/atcq.23.2-3.203.

Scaramuzza, D., and R. Siegwart. 2008. “Appearance-Guided Monocular Omnidirectional Visual Odometry for Outdoor Ground Vehicles.” *IEEE Transactions on Robotics* 24 (5): 1015–26. https://doi.org/10.1109/TRO.2008.2004490.

Schumacher, Adrian. n.d. “Integration of a GPS Aided Strapdown Inertial Navigation System for Land Vehicles.”

Sedjelmaci, Hichem, Sidi Mohammed Senouci, and Nirwan Ansari. 2017. “A Hierarchical Detection and Response System to Enhance Security against Lethal Cyber-Attacks in UAV Networks.” *IEEE Transactions on Systems, Man, and Cybernetics: Systems* 48 (9): 1594–1606.

Semke, William, Nicholas Allen, Asma Tabassum, Matthew McCrink, Mohammad Moallemi, Kyle Snyder, Evan Arnold, Dawson Stott, and Michael G. Wing. 2017. “Analysis of Radar and ADS-B Influences on Aircraft Detect and Avoid (DAA) Systems.” *Aerospace* 4 (3): 49. https://doi.org/10.3390/aerospace4030049.

Shamaei, Kimia, and Zaher M. Kassas. 2019. “Sub-Meter Accurate UAV Navigation and Cycle Slip Detection with LTE Carrier Phase Measurements.” In , 2469–79. https://doi.org/10.33012/2019.17051.

Shan, Mo, Fei Wang, Feng Lin, Zhi Gao, Ya Z. Tang, and Ben M. Chen. 2015. “Google Map Aided Visual Navigation for UAVs in GPS-Denied Environment.” *2015 IEEE International Conference on Robotics and Biomimetics, IEEE-ROBIO 2015*, 114–19. https://doi.org/10.1109/ROBIO.2015.7418753.

Shashok, Nikolas. 2017. “Analysis of Vulnerabilities in Modern Unmanned Aircraft Systems To The Community : Modern Drone Uses and Risks.”

Shi, Jianbo and Tomasi. 1994. “Good Features to Track.” In *1994 Proceedings of IEEE Conference on Computer Vision and Pattern Recognition*, 593–600. https://doi.org/10.1109/CVPR.1994.323794.

Silvagni, Mario, Andrea Tonoli, Enrico Zenerino, and Marcello Chiaberge. 2017. “Multipurpose UAV for Search and Rescue Operations in Mountain Avalanche Events.” *Geomatics, Natural Hazards and Risk* 8 (1): 18–33.

Sobers, D. Michael, Girish Chowdhary, and Eric N. Johnson. 2009. “Indoor Navigation for Unmanned Aerial Vehicles.” *AIAA Guidance, Navigation, and Control Conference and Exhibit*, no. August. https://doi.org/10.2514/6.2009-5658.

Song, Xiaojing, Lakmal D. Seneviratne, and Kaspar Althoefer. 2011. “A Kalman Filter-Integrated Optical Flow Method for Velocity Sensing of Mobile Robots.” *IEEE/ASME Transactions on Mechatronics* 16 (3): 551–63. https://doi.org/10.1109/TMECH.2010.2046421.

sUAS news. 2021. “New York’s 50-Mile Drone Corridor Integrates 5G Test Network.” SUAS News - The Business of Drones. September 29, 2021. https://www.suasnews.com/2021/09/new-yorks-50-mile-drone-corridor-integrates-5g-test-network/.

Sung, Yunsick, Sejun Jang, Young Sik Jeong, and Jong Hyuk (James J.). Park. 2020. “Malware Classification Algorithm Using Advanced Word2vec-Based Bi-LSTM for Ground Control Stations.” *Computer Communications* 153 (December 2019): 342–48. https://doi.org/10.1016/j.comcom.2020.02.005.

Syd Ali, Busyairah, Wolfgang Schuster, Washington Ochieng, and Arnab Majumdar. 2016. “Analysis of Anomalies in ADS-B and Its GPS Data.” *GPS Solutions* 20 (3): 429–38. https://doi.org/10.1007/s10291-015-0453-5.

Tabassum, Asma. 2017. *Performance Analysis of Automatic Dependent Surveillance-Broadcast (ADS-B) and Breakdown of Anomalies*. The University of North Dakota.

Tabassum, Asma, and William Semke. 2018. “UAT ADS-B Data Anomalies and the Effect of Flight Parameters on Dropout Occurrences.” *Data* 3 (2): 19.

“The 1090MHz Riddle.” n.d. Accessed May 18, 2023. https://mode-s.org/decode/content/ads-b/1-basics.html.

“The OpenSky Network - Free ADS-B and Mode S Data for Research.” n.d. Accessed July 6, 2023. https://opensky-network.org/.

Thébault, Erwan, Christopher C. Finlay, Ciarán D. Beggan, Patrick Alken, Julien Aubert, Olivier Barrois, Francois Bertrand, et al. 2015. “International Geomagnetic Reference Field: The 12th Generation.” *Earth, Planets and Space* 67 (1): 79. https://doi.org/10.1186/s40623-015-0228-9.

Titterton, David, and John L. Weston. 2004. *Strapdown Inertial Navigation Technology*. IET.

Vasconcelos, Gabriel, Gabriel Carrijo, Rodrigo Miani, Jefferson Souza, and Vitor Guizilini. 2016. “The Impact of DoS Attacks on the AR.Drone 2.0.” *Proceedings - 13th Latin American Robotics Symposium and 4th Brazilian Symposium on Robotics, LARS/SBR 2016*, 127–32. https://doi.org/10.1109/LARS-SBR.2016.28.

Vidal, Chaz, and Kim Kwang Raymond Choo. 2018. *Situational Crime Prevention and the Mitigation of Cloud Computing Threats*. *Lecture Notes of the Institute for Computer Sciences, Social-Informatics and Telecommunications Engineering, LNICST*. Vol. 239. https://doi.org/10.1007/978-3-319-78816-6_16.

W. Freeden, M. Z. Nashed, and T. Sonar. 2010. *Handbook of Geomathematics*. Springer Science & Business Media.

Wang, Fei, Kangli Wang, Shupeng Lai, Swee King Phang, Ben M. Chen, and Tong H. Lee. 2014. “An Efficient UAV Navigation Solution for Confined but Partially Known Indoor Environments.” *IEEE International Conference on Control and Automation, ICCA*, 1351–56. https://doi.org/10.1109/ICCA.2014.6871120.

Wang, Haichao, Jinlong Wang, Jin Chen, Yuping Gong, and Guoru Ding. 2018. “Network-Connected UAV Communications: Potentials and Challenges.” *China Communications* 15 (12): 111–21.

Wei, Liu, Wu Zhitian, Meiping Wu, and Xiaoping Hu. 2011. “Geomagnetic Matching Technology Based on Iterative Contour Matching Algorithm.” In *IEEE 2011 10th International*

Conference on Electronic Measurement & Instruments, 4:342–45. https://doi.org/10.1109/ICEMI.2011.6038011.

Wheeler, David O., Daniel P. Koch, James S. Jackson, Gary J. Ellingson, Paul W. Nyholm, Timothy W. McLain, and Randal W. Beard. 2020. "Relative Navigation of Autonomous GPS-Degraded Micro Air Vehicles." *Autonomous Robots*, 1–20.

Wu, Zhijun, Tong Shang, and Anxin Guo. 2020. "Security Issues in Automatic Dependent Surveillance - Broadcast (ADS-B): A Survey." *IEEE Access* 8: 122147–67. https://doi.org/10.1109/ACCESS.2020.3007182.

Xiao, Jing, Xiusheng Duan, Xiaohui Qi, and Yifei Liu. 2020. "An Improved ICCP Matching Algorithm for Use in an Interference Environment during Geomagnetic Navigation." *The Journal of Navigation* 73 (1): 56–74. https://doi.org/10.1017/S0373463319000535.

Yağdereli, Eray, Cemal Gemci, and A. Ziya Aktaş. 2015. "A Study on Cyber-Security of Autonomous and Unmanned Vehicles." *Journal of Defense Modeling and Simulation* 12 (4): 369–81. https://doi.org/10.1177/1548512915575803.

Zeng, Yong, Rui Zhang, and Teng Joon Lim. 2016. "Wireless Communications with Unmanned Aerial Vehicles: Opportunities and Challenges." *IEEE Communications Magazine* 54 (5): 36–42. https://doi.org/10.1109/MCOM.2016.7470933.

Zhao, Shiyu, Feng Lin, Kemao Peng, Xiangxu Dong, Ben M. Chen, and Tong H. Lee. 2016. "Vision-Aided Estimation of Attitude, Velocity, and Inertial Measurement Bias for UAV Stabilization." *Journal of Intelligent and Robotic Systems: Theory and Applications* 81 (3–4): 531–49. https://doi.org/10.1007/s10846-015-0206-2.

9. APPENDICES

Appendix 1. A11L.UAS.86 - A44 Mitigating GPS and ADS-B Risks for UAS Task 1: Literature Review

Appendix 2. A11L.UAS.86 - A44 Mitigating GPS and ADS-B Risks for UAS Task 2: Identification of Potential Mitigations

Appendix 3. A11L.UAS.86 - A44 Mitigating GPS and ADS-B Risks for UAS Task 3: Planning the Testing and Demonstration of Mitigations

Appendix 4. A11L.UAS.86 - A44 Mitigating GPS and ADS-B Risks for UAS Task 4: Test Plan and Report